REFERENCE ONLY

UNIVERSITY OF LONDON THESIS

Degree PhD Year 2005 Name of Author GOFF C-P

X-Ray Studies of Flaring Magnetic Structures

Christopher Philip Goff

Mullard Space Science Laboratory
Department of Space and Climate Physics
University College London

A thesis submitted to the University of London
for the degree of Doctor of Philosophy

ProQuest LLC
789 East Eisenhower Parkway
P.O. Box 1346
Ann Arbor, MI 48106-1346

To

someone

for something

Abstract

This thesis studies non–thermal emission from flaring magnetic structures by looking at HXR emission from flare footpoints; at a faint X–ray source above a flare loop; and finally at radio emission generated by eruptions. By complementing high quality data from recent missions with data from older instrumentation, studies were performed to compare with accepted models.

The relation between Hard X–ray footpoint emission and magnetic field strength in a sample of 32 flares was studied in order to investigate the effects of the magnetic field on the transport of accelerated electrons. It was found that one third of compact flares studied had stronger footpoints in stronger magnetic regions whereas the reverse is anticipated from magnetic trapping arguments.

On 16th April 2002, a limb flare was studied in many wavelengths. This provided an opportunity to study an erupting filament from the low corona and into interplanetary space. *RHESSI* identified a moving X–ray source associated with a rising filament, confirming the plasmoid definition of Tsuneta (1997). The velocity profile of the filament was determined along with its exponential acceleration. This suggested that an instability was responsible for eruption, possibly the kink instability. Doppler shifts were observed on either side of the filament as it crossed the slit field of view, suggesting helical flows and thus a flux rope.

A succession of quadrupolar flares, followed by an LDE were then studied. An associated CME was seen and appeared linked to the quadrupolar flares which should remain confined. The flaring region triggered loop expansion, which interacted with a neighbouring large–scale streamer. This led to a fast CME front, which weakened the restraining field above the active region filaments allowing a partial filament eruption. Although at first glance the observations appeared contradictory; it was demonstrated that the quadrupolar flares remained confined while triggering a large–scale eruption.

Contents

List of Figures

List of Tables

Chapter 1

Introduction

It is very rare that as a science student one gets to make observations and deductions on an object that is of such vital importance to mankind that it was once regarded as a deity. To the ancient Egyptians, for example, the Sun god, Ra, was born each morning and carried across the heavens in a boat to die in the west in the evening; during the night he was carried beneath the world to his rebirth in the east.

To the ancient Greeks Apollo would ride across the heavens in a fiery chariot. Yet even then, some 2,500 years ago, there were those who speculated about the physical nature of this shining Orb. Attempts were made to gauge its size and distance. Even sunspots were observed as early as 350 B.C. by Theophrastus of Athens, a pupil of Aristotle, giving the indication that the Sun was not perfect and blemish free. Long–term observations of sunspots allowed Samuel Heinrich Schwabe (1826–1843) to revealed the existence of a sunspot cycle. Further Carrington (1863) was able to determine the nature of surface rotation through similar observations. In fact, the Chinese have observations of sunspots dating back over 2000 years. However with the invention of the telescope more detailed observations of sunspots could be made, with seminal work carried out by Galileo Galilei in the 17th century.

From a modern astronomer's point of view the Sun is of utmost interest as it is the only star that can be spatially resolved at high resolution. Until comparatively recently the Sun could be studied only by means of visible light emitted from the surface and by

spectral line observations from the chromosphere. With the advent of radio astronomy around the time of the Second World War, new facets of solar structure and activity were unveiled. Although modern techniques have permitted other wavelengths to be detected from Earth–based observatories and high–altitude balloons, it was the development of space technology that suddenly opened up the observational toolkit for the solar physicist. This allowed the Sun to be viewed in a totally new way using parts of the electromagnetic spectrum normally attenuated by the Earth's atmosphere. Most significantly, observations could be made of plasma emitting at extreme–ultraviolet and X–ray wavelengths. Additionally uninterrupted observations can be made without the limitations imposed by monitoring only during daylight hours.

These observations have revealed a variety of solar phenomena across all observable spatial and temporal scales. Our understanding of the physical processes taking place in the Sun has advanced substantially since the first telescope observations. However, many questions on the phenomena that are observed remain unanswered.

1.1 Overview

The Sun is regarded as a giant ball of plasma, considered on short time scales as being approximately in hydrostatic equilibrium. However, there is structure within the Sun. The solar interior consists of the core, radiation zone and convection zone. Between the radiative and convection zone is a thin layer called the tachocline, the most likely location of the solar dynamo which is responsible for the cyclic generation and reversal of solar magnetic fields. The atmosphere consists of the photosphere, chromosphere, transition region and corona. The atmospheric layers are defined by their temperatures and are best illustrated by Figure 1.1. The approximation that the Sun is in hydrostatic equilibrium most obviously breaks down when considering the solar wind. This is the constant outflow of plasma, from the Sun into interplanetary space, which occurs as a consequence of the continual expansion of the hot corona into the near vacuum of space. This chapter presents an overview of the solar atmosphere and magnetic fields along with

the theory governing the behaviour of the system.

1.2 The Solar Atmosphere

The following section will describe the basic properties of each region of the solar atmosphere from the photosphere through to the corona.

1.2.1 The Photosphere

The photosphere is the lowest, densest level of the solar atmosphere. The opacity of the atmosphere of the Sun increases as you approach from interplanetary space. The point at which the atmosphere appears to become completely opaque to radiation is known as the photosphere, and is regarded as the surface of the Sun. It is an extremely thin layer (a few hundred kilometres thick) where the solar photons created in the core become able to pass through the solar atmosphere suffering only weak absorption. This layer is the source of sunlight, and is appropriately named from the Greek word *photos* meaning 'light'.

The photosphere has an effective blackbody temperature of 5800 K and the emission peaks at visible wavelengths. Here it is sufficiently cool that protons and electrons can form hydrogen atoms. In a rare collision, a hydrogen atom in the photosphere can briefly attach a free electron to form a hydrogen ion, H^-, which can subsequently lose its electron through the absorption of a photon. The photosphere can be summarised as the region between 6600 K (base of photosphere) and the temperature minimum 4300 K, which is 500 km above the base.

The photosphere is in continual motion as a result of the convection cells from the convection zone below, which overshoot to produce granulation cells with a thickness of around 100–200 km. The centre of the cells appear bright in comparison to the boundary due to the hot plasma rising from below (0.4 km s^{-1}), which moves across (~0.25 km s^{-1}) to the cell boundary where it sinks as cooler plasma. The diameter of these granulation cells is typically between 700 and 150 km and they have a lifetime of around 8 minutes.

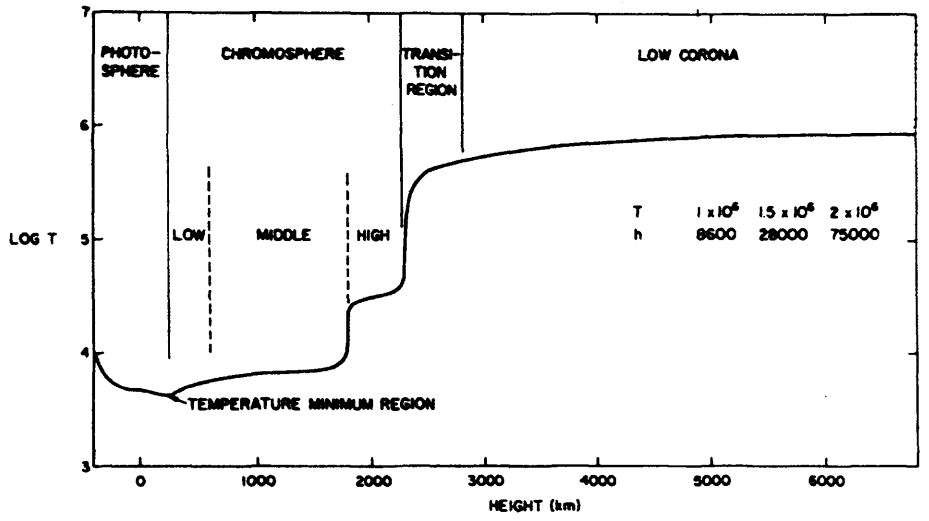

Figure 1.1: The temperature structure of the solar atmosphere (courtesy of Athay, 1976). The temperature is observed to decrease through the photosphere until a minimum of 4300 K is reached 500 km above the base of the photosphere. The temperature increases from this point into the corona where magnitudes of 2 MK are reached.

Larger scale velocity patterns known as meso–granulation and super–granulation also exist. Super–granule cells are typically between 20,000 and 54,000 km across with a lifetime of 1 to 2 days. Convective flows here are weaker than in the smaller scale granules and the material rises in the centre of the cells with a velocity of 0.1 km s^{-1}, moves horizontally at around 0.3–.4 km s^{-1} and sinks at the edge of the cell at 0.1–0.2 km s^{-1}.

The photosphere is not uniform in brightness. It often has dark patches on the surface referred to as sunspots. They appear dark as they are cooler than their bright surroundings. A simple sunspot has a dark centre, called the umbra, surrounded by a lighter penumbra. Sunspots are regions of intense magnetic field which are believed to rise from the solar interior to the surface as a result of magnetic buoyancy.

1.2.2 The Chromosphere

Moving up through the solar atmosphere, in both height and temperature, is the chromosphere, from *Chromos* the Greek word for colour. The chromosphere is very faint, and

the underlying photosphere so bright, that it was first observed during a total eclipse. It becomes visible for a short while before and after totality, as a narrow, rose–coloured band at the limb.

The chromospheric region of the solar atmosphere extends from approximately 500 km to 2300 km above the base of the photosphere. Disc observations of the chromosphere are made using the light of Hα (formed by the $n = 3$ to $n = 2$ Balmer transition at 6563 Å , in the red part of the spectrum giving the rose colour) and the Ca II H and K lines (3968 Å and 3934 Å). Non–visible wavelengths are also used to observe the hotter regions of the upper chromosphere, such as ultra–violet (UV; 1000 Å – 3500 Å) and extreme ultra–violet (EUV; 100 Å – 1000 Å) lines.

Super–granulation boundaries are observed in the Ca II K line and observations in Hα near the limb reveal plasma jets known as spicules (Beckers 1972) in the boundaries of the super–granules where small–scale magnetic fields are being concentrated by flows. Hα observations on the disc reveal horizontal features known as fibrils which follow the direction of magnetic field lines.

The temperature increases in the atmosphere from the base of the chromosphere and there is an especially sharp rise at the interface between the chromosphere and the corona, in a region known as the *transition region.* In the transition region the temperature rises from tens of thousands to over 1 million Kelvin. This is illustrated in Figure 1.1.

1.2.3 The Corona

The temperature rise continues into the solar atmosphere, to the region known as the solar corona, where temperatures of 2 million Kelvin and greater are reached. The mean corona is situated above the chromosphere, and plasma with different temperatures co–exist in this region.

The first indications that the solar corona was extremely hot and tenuous (10^8 cm^{-3}) came from the observations of emission lines from forbidden transitions (e.g. Fe X line

at 6374 Å, Edlén 1942). In a gas of moderate density, collisions would destroy the excitations before a spectral line can be emitted. However, in the hot tenuous plasma of the corona, these transitions can be dominant.

Observations of the corona cannot normally be made due to the overwhelming photospheric emission (the coronal intensity is approximately one–millionth of the photospheric intensity). However, white light observations can be made at times of eclipse, or with the use of a coronagraph which produces an artificial eclipse. Direct images can be taken in ultraviolet, extreme ultraviolet or X–rays as the plasma emits thermally at coronal temperatures. The reasons for the high temperature of the coronal plasma are still disputed and several mechanisms have been proposed; different mechanisms may be responsible for heating in different regions. In general, the heating mechanisms can be divided into 2 groups, the first involves heating due to the dissipation of magnetohydrodynamic waves generated at the base of the corona. The second group involves the dissipation of free magnetic energy created by the shuffling of the flux tube footpoints due to photospheric motions. Recent work has indicated that coronal heating models based on the stressing of the coronal fields by footpoint motions better fit the observational constraints than do those models based on wave dissipation e.g. Mandrini et al. (2000); Démoulin et al. (2003).

Soft X–ray images of the Sun were first taken using instruments flown on rockets, the typical angular resolution being 2 arc minutes. The first high resolution soft X–ray images of the corona were taken with the grazing incidence telescope on–board Skylab (Vaiana et al. 1977). It was later realised that the observed structure in the corona is dominated by the magnetic fields and can be roughly divided into two regions: those where the magnetic field is open and extends into the interplanetary medium, and regions where the field is closed with both ends of the flux tube intersecting the photosphere. In X–rays the closed field regions appear as coronal loops in a range of sizes and topologies, associated with both the quiet Sun and the concentrated magnetic fields above sunspots. In these regions the plasma is confined by the magnetic field and is thus relatively high density. The open field regions appear dark due to the low plasma density which results from the outflow

of plasma to form coronal holes and the fast solar wind. Open field lines are defined to be those that extend outward beyond the height at which the velocity of the solar wind becomes super–sonic.

1.2.4 Atomic Processes

There are five general atomic processes and they are summarised in this section.

Bound–free or Continuum An absorbed photon has enough energy to remove an electron from its bound state. The atom is therefore ionised.

Free– bound or Recombination The Recombination of a free electron and ion gives rise to photons of all energies above the ionisation energy and this emission forms the continuum.

Free–free When a free electron drops into another unbound state of lower energy contributing to the continuum.

Bound–bound These transitions involve the photon energy lifting a bound electron from one bound state to another. The photon must have precisely the right energy to do this and so the absorption is always monochromatic, occurring in a narrow band of wavelengths. Hence a line appears in the spectrum.

Thomson Scattering Photons are scattered by free electrons

1.3 The Dynamic Sun

The solar atmosphere is a very dynamic environment. Recent solar observations have revealed that the solar atmosphere is much more dynamic than had been previously thought; even the quiet Sun is never quiet. With advances in instrumentation and constant monitoring of the Sun our knowledge and understanding of active phenomena has increased.

It is widely understood that dynamic phenomena occur as a result of the release of free magnetic energy. Strong magnetic regions are seen to be coincident with sunspots and they have been interpreted as the intersection of flux tubes with the surface which were created at the base of the convection zone and buoyed up into the corona. As the flux tubes rise their shape resembles that of the letter Ω since they keep their connections to their toroidal roots, and they are thus referred to as Ω loops. When using magnetograms to observe magnetic field lines only the cross–section of the flux tube with the photosphere can be seen. The flux tubes rise and expand, and also rotate due to the Coriolis force. They rotate clockwise in the northern hemisphere and anti–clockwise in the southern (Joy's Law). Field lines are traced out by emitting plasma which can be observed in X–ray and Extreme Ultra–Violet wavelengths. They show themselves as complex systems of loops in the solar atmosphere.

The emergence of twisted magnetic bundles and the existence of shearing motions in the photosphere makes the coronal magnetic field very complex and as a result it stores magnetic energy. Solar flares act as a release for this energy, which is then injected into the solar atmosphere on a very short timescale. The energy release is widely believed to be achieved through magnetic reconnection, or re-arrangement of field line connectivities since it can explain many of the observational signatures associated with flares. As a direct result of this energy release other associated phenomena are observed in many wavebands, for example, ejections of plasma, post–flare loops, and non–thermal emission from energetic particles.

1.3.1 Solar Flares

1.3.1.1 Photospheric and Chromospheric Effects

Solar flares can release energies of up to about 10^{32} ergs in a few tens of minutes or less. Flares are the response of the solar atmosphere to a sudden, transient release of magnetic energy. Figure 1.2 shows schematic light curves of a flare measured in various wavelengths. They have been extensively studied since they were first observed in white

light by Carrington (1859).

With Hα observations, it is possible to see bright flashes associated with flares. In large–scale and long duration flares, two bright ribbons can be observed (e.g. Figure 1.3). These 'ribbons' are two long bright regions that form either side of a magnetic neutral line, thus in regions of opposite polarity. As the flare progresses the ribbons are seen to separate. The light curve of the Hα flux integrated over the flaring region shows gradual change. The brightenings are thought to be caused by the precipitation of non–thermal electrons from the corona into the chromosphere, which stimulates the excitation and ionisation of hydrogen atoms (Ricchiazzi & Canfield 1983; Canfield et al. 1984). Since this precipitation also produces hard X–ray (HXR) radiation via bremsstrahlung, there can be patches of correlation in Hα ribbons and HXR sources.

Some filamentary material, which is dark on the disk (filament) and bright on the limb (prominence), can also be seen in Hα. There are often relationships between flares and activities in filaments that lie along neutral lines in active regions that will be described later.

Flares often occur following the emergence of new flux, which carries new magnetic energy into the corona. Shearing motions in the photosphere also make the magnetic field more stressed, storing energy.

1.3.1.2 Coronal Effects

Phenomena that occur in the corona are more dynamic than those in the chromosphere. In the past it was very difficult to observe structure within the corona because the plasma is high temperature and low density. However, with space based instruments it became possible to observe in the X–ray and extreme ultraviolet (EUV) wavelengths.

With the launch of *Yohkoh* (Ogawara et al. 1991) X–ray observations were made routinely over ten years. *Yohkoh* was able to reveal the dynamic features of the magnetic corona. Observations in the soft X–ray (SXR) range suggested that magnetic energy is released in the corona through magnetic reconnection and then carried down to the chromosphere by energetic particles and thermal conduction along reconnected field lines.

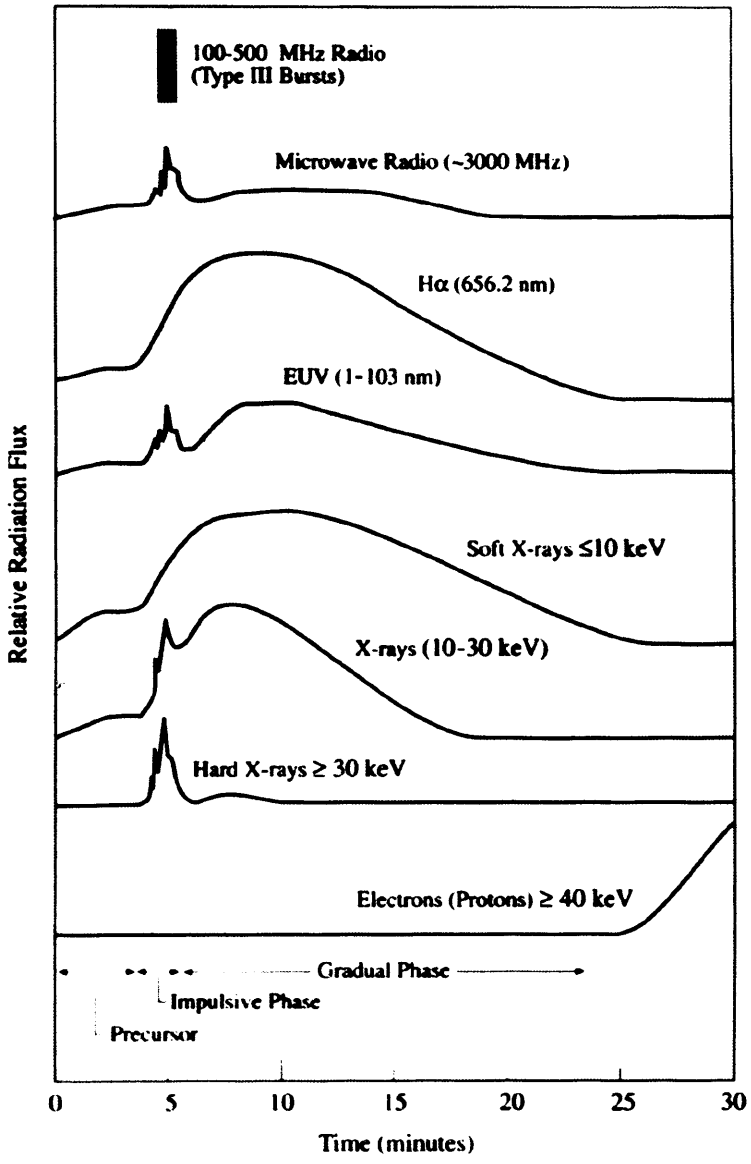

Figure 1.2: Time profiles of solar flares as observed at different wavelength bands. (based on Kane (1974))

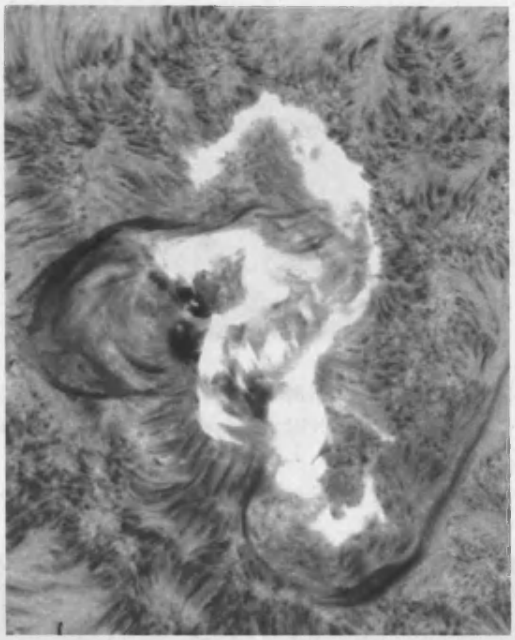

Figure 1.3: The great 'Seahorse Flare' of August 7th, 1972: This image in the blue wing of Hα shows the two–ribbon structure late in the event, with bright Hα loops connecting the ribbons.

The chromospheric plasma is pumped explosively up the loops due to a radiative instability and pressure enhancement in a process referred to as 'chromospheric evaporation'. The coronal density in the flare loops (which are in fact newly reconnected field lines) increases dramatically because of chromospheric evaporation, making the flare loops visible in SXR. Since the plasma in the corona is assumed to be frozen into the magnetic field, it is confined to travel along the magnetic field lines. This enables a visualisation of the magnetic field containing such emitting plasma.

The coronal plasma is heated, sometimes up to 40 MK, during and just after the flare energy release occurs, which then cools due to thermal conduction and radiation. It becomes observable in EUV (~1 MK) and finally in Hα (10^4K, Figure 1.3) as it cools. These loops are referred to as (post) flare loops and represent field lines of decreased stress.

The SXR flare often shows a cusp shape structure (Tsuneta et al. 1992; Forbes & Acton 1996) such as that presented in Figure 1.4. It is believed that above the peak of this

Figure 1.4: This cusp structure was observed with *Yohkoh* SXT on 18th March 1999. This image was taken from the Montana Science Nuggets of March 19, 1999, by H. Hudson.

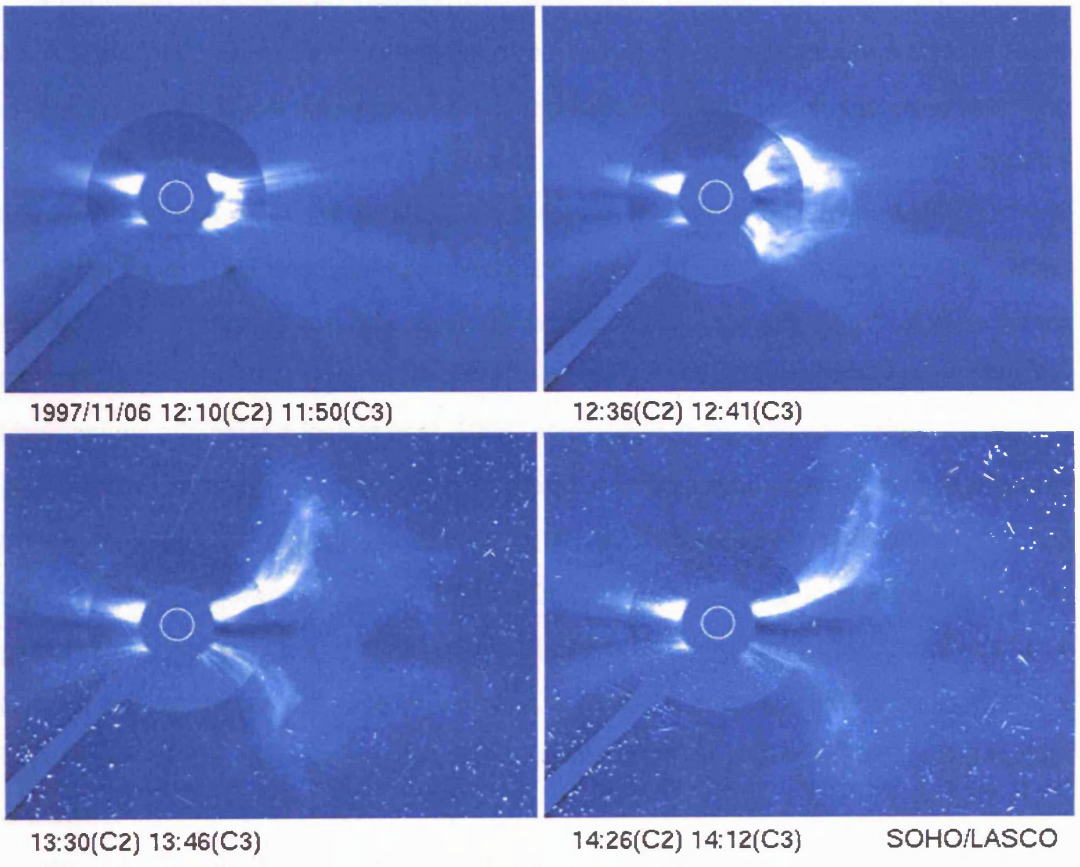

Figure 1.5: A CME observed by LASCO C2 and C3 from the 6th November 1997 provided by the *SoHO* gallery. The size of the Sun is indicated by a white circle.

cusp represents a region at which field lines reconnect. These cusped loops grow with time providing evidence for reconnection occurring at successively higher altitudes as the flare progresses.

1.3.2 Filament Ejections and Coronal Mass Ejections

Filaments lie along magnetic neutral lines. Quiescent filaments do not usually show any drastic changes during a solar rotation. However active region filaments can disappear or be ejected prior to solar flares, especially with large–scale, long–duration events (LDEs). These filament eruptions form part of events known as coronal mass ejections (CMEs).

Filaments comprise high–density, low–temperature plasma. They are supported by the coronal magnetic field along the magnetic neutral line. If these erupt a two–ribbon flare is often seen either side of the original filament position. SXR plasmoid ejections have been observed by Ohyama & Shibata (1998) and are thought to be the coronal counterpart of filament eruptions. They are accelerated during the impulsive phase of a flare.

Large flares are sometimes accompanied by coronal mass ejections (CMEs) (Harrison 2002). An example can be seen in the series presented in Figure 1.5. CMEs present themselves as a balloon type structure as they expand above the solar corona. The first observations of CMEs (Gosling et al. 1974) were made in the 1970s by space–borne coronagraphs; instruments which produce an artificial eclipse thus allowing coronal observations by blocking the bright photospheric emission. They exhibit a range of morphologies from the classical 3–part structure (Forbes 2000) (an expanding loop followed by a depleted region and inside a bright core containing filament material) to amorphous blobs. Like the corona itself CMEs are observed in white–light as the result of Thomson scattering of light off the coronal electrons, the intensity of which is proportional to the electron density.

From their early discovery a link of CMEs with solar flares was sought to understand the CME launch process (Dryer 1982) and it was assumed that a CME required a flare. The work of Burkepile & et al. (1994); Munro et al. (1979); Harrison (1995); Kay et al.

(2003) found that the probability of a CME occurring with a flare increases with the intensity of the X-ray flare. However, this is not always the case. Green et al. (2002) observed an X1.2 class flare from which there was no associated CME. Additionally flare duration and the probability of CME launch has been studied showing that CME launch prefers long duration events e.g. Sheeley et al. (1983); Harrison (1995).

It has been noticed that often the closest associated flare had a rise phase which followed the CME launch. Harrison (1996) used data from the Solar Maximum Mission (SMM) and observed a weak soft X–ray burst (the precursor), which preceded the flare by several tens of minutes, and during which the CME was released.

1.3.3 Energetic Particles

Energetic particles are closely associated with solar flares and they give rise to non–thermal emissions. The particles are accelerated following magnetic reconnection. Non–thermal emissions are often observed in HXRs, microwave and γ–ray wavelengths.

Neupert (1968) reported that the variation of the time integral of the microwave intensity often closely matches the variation of the SXR intensity in flares, a phenomenon termed the Neupert effect. Since the SXR emission is roughly representative of the thermal energy, the Neupert effect indicates that the microwave intensity is proportional to the energy release rate. This can be extended to HXR emission due to the similarity between the light curves of both microwave and HXR wavebands. This non–thermal emission is seen in Figure 1.2 and has a spiky nature. This is referred to as the 'impulsive phase' and appears in the initial phase of a solar flare, the time of particle acceleration.

Our understanding of hard X–ray emission has been revolutionised by observations using HXR spectrometers and imagers such as *SMM* HXIS, *SMM* HXRBS, *Yohkoh* HXT, and *RHESSI* (details of some of these instruments are given in Chapter 2). The most important radiation mechanism that produces a continuum of emission in the hard X–ray wavebands is collisional bremsstrahlung. This results from the emission of photons when electrons are elastically scattered in the electric Coulomb field of ambient ions. There are

three commonly discussed scenarios that can cause such emission:

Thermal bremsstrahlung; the fats colliding electrons are locally Maxwellian and have the same temperature as the ambient plasma.

Non–Thermal Thin–target bremsstrahlung; the electrons are continuously accelerated in a collisional plasma and the X–ray spectrum in nearly unchanged from the injection spectrum.

Non–Thermal Thick–target bremsstrahlung; the incident electrons have been accelerated to a high, non–thermal, energy (in a collisionless plasma) and are then stopped in a cool thermal plasma (Brown 1971), where primarily Coulomb collisions cause modifications to the injected spectrum.

The solar hard X–ray imagers enabled, for the first time, spatial studies of this emission. Sakao (1994) reviewed the features of HXR emitting sources during solar flares. The strongest sources are flare loop footpoints due to thick–target bremsstrahlung in or near the chromosphere as found by Hoyng et al. (1976) using HXIS. Sakao found that around 40% of the 28 flares he studied had double HXR sources observed, examples of which can be seen in Chapter 3. With the observations from *Yohkoh* it was possible to verify these sources as footpoints because they were spatially coincident with the ends of loops seen in soft X–rays.

Masuda et al. (1994) observed a loop–top HXR source with *Yohkoh*'s Hard X–ray Telescope. This source was much weaker than the footpoint sources, but does imply that the energy release occurs at a higher site, supporting reconnection models. This result is shown in Figure 1.6.

An excellent review of X–ray observations from *RHESSI* has been produced by Dennis et al. (2005) which shows how much these kinds of observations have progressed since *Yohkoh* . Perhaps the most surprising result was the apparent displacement in one event between the source of the neutron–capture gamma–ray line and the source of the bremsstrahlung X–rays (Hurford et al. 2003). This suggests that there are differences

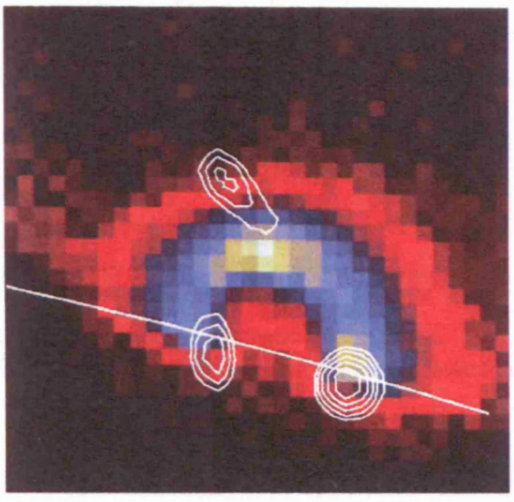

Figure 1.6: The loop top source observed on the 13th January 1992. The background image is an SXT image with HXT contours on top Masuda et al. (1994). The white line indicates the solar limb.

between the acceleration and/or transport of the energetic ions and electrons. When energetic ions collide with the solar atmosphere they excite nuclei that emit nuclear de-excitation lines along with electrons and positrons which result in the delayed neutron–capture line and the positron–annihilation line. Another remarkable result is the evidence for magnetic reconnection in a current sheet above the flare loops, based on the observation of an above–the–looptop source (Sui et al. 2004; Goff et al. 2005). This is further discussed in chapter 4.

1.3.4 Magnetic Reconnection

Magnetic reconnection is a topological restructuring of a magnetic field caused by a change in the connectivity of its field lines. It is this change that allows the release of stored magnetic energy. Magnetic reconnection was first proposed to be the flare energy release mechanism by Dungey (1953) and quantified by Sweet (1958b) and Parker (1957) and still further developed by Parker (1963), Petschek (1964) and others. Magnetic reconnection theory can be used to explain many characteristics of numerous solar phenomena, for example jets, flares and CMEs.

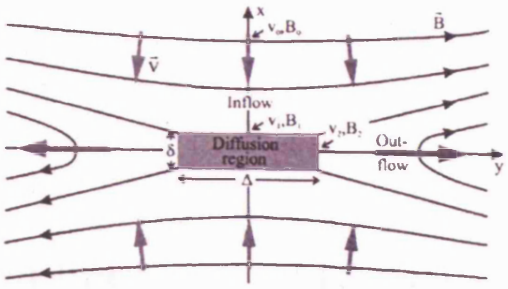

Figure 1.7: The basic 2D representation of magnetic reconnection. Two oppositely directed inflows bring together oppositely oriented lines which diffuse and reconnect creating oppositely directed outflows (Schindler & Hornig 2001).

Magnetic reconnection requires plasma to have resistivity. As regions of plasma containing oppositely oriented magnetic field approach one another a current sheet is formed. The current flows with almost no resistance, because the conductivity of coronal plasma is very high. However, if there is local resistance ideal MHD breaks down and the frozen–in conditions do not apply. The field lines can then reconnect (illustrated in Figure 1.7).

Over the years many people have used the magnetic reconnection principle in models to explain observations. It is generally accepted that there is no 'one size fits all' flare model, but there are several that are widely accepted. A selection of the most commonly referenced models are discussed below, namely the CSHKP 2D model, the emerging flux model, a quadrupolar flare model and the breakout model.

1.3.4.1 The CSHKP 2D Flare Model

This 2D flare model is one of the most widely accepted and is named after the five authors from whom it evolved (Carmichael 1964; Sturrock 1966; Hirayama 1974; Kopp & Pneuman 1976) (Figure 1.8). This was further extended by the works of Tsuneta (1996, 1997) (Figure 1.9) and Shibata et al. (1995) (Figure 1.10) based upon *Yohkoh* observations.

In this model the initial driver is the rising prominence or filament. The filament is suspended by magnetic field lines above a neutral line in an active region and as it rises, the filament acting to stretch the magnetic field lines. This results in a current sheet

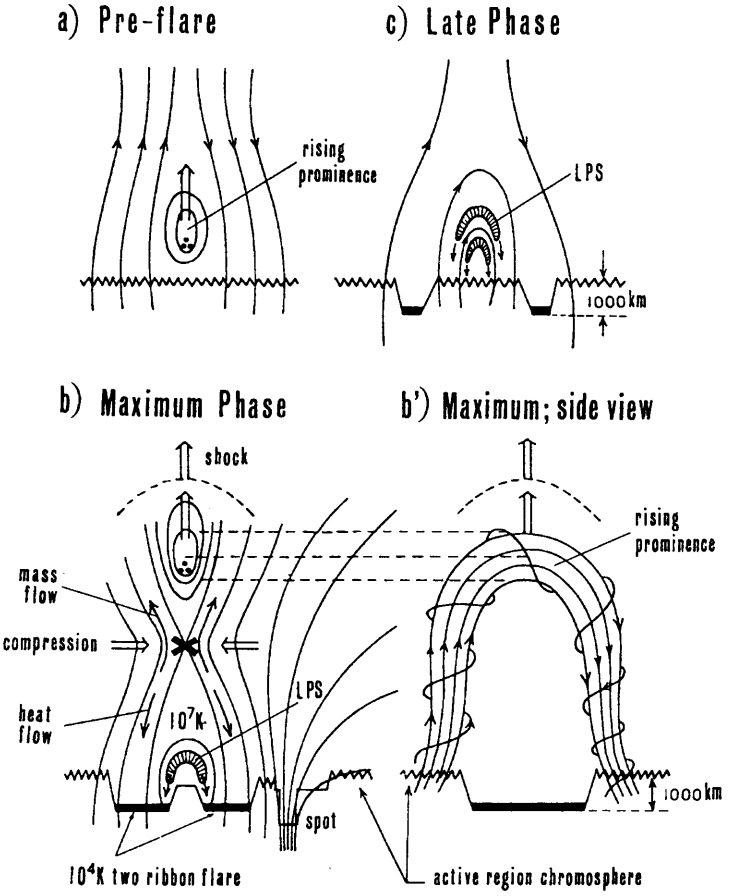

Figure 1.8: A time series of cartoons from the model of Hirayama (1974). (a) shows a rising filament/prominence which causes the X-point reconnection shown in (b) and from the side in (b'). The whole process ends with the late phase shown by consecutively reconnected flare loops in (c).

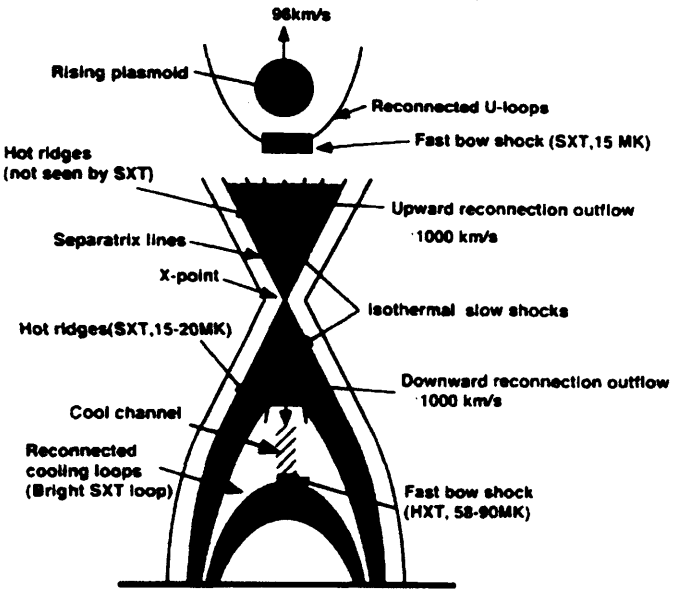

Figure 1.9: Expansion on the previous CSHKP model showing shocks and the upward moving plasmoid; Tsuneta (1997).

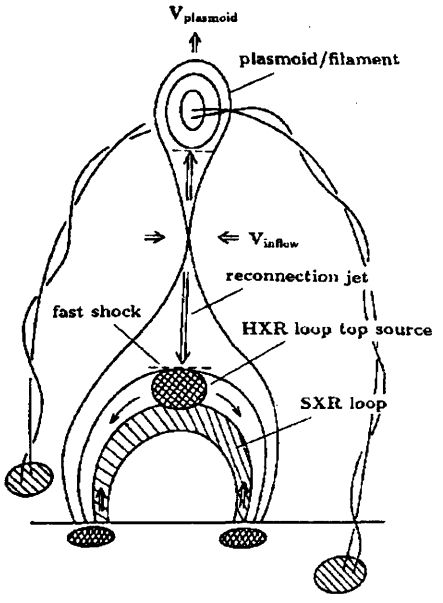

Figure 1.10: Again an expansion on the previous CSHKP model showing the upward moving plasmoid, which is in fact the erupting filaments; Shibata et al. (1995).

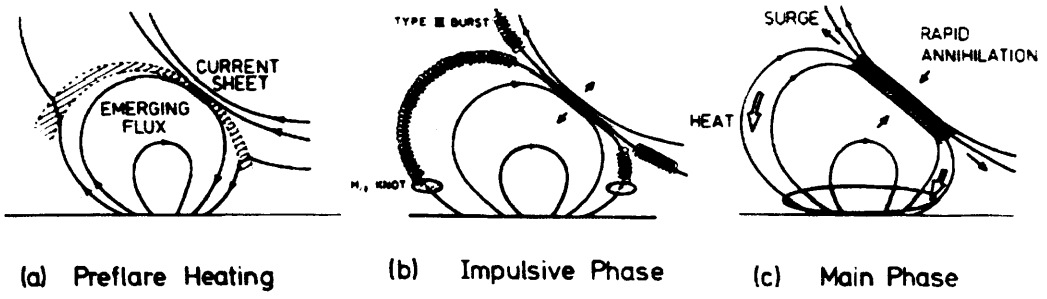

Figure 1.11: A three phase model for solar flares due to emerging magnetic flux (Heyvaerts et al. 1977)

forming between oppositely orientated field lines rooted on both sides of the inversion line. This configuration is then prone to reconnection such as that shown in cartoon (b) and (b') of Figure 1.8. Material flows above a cusped structure towards an X–point, a situation that was observed by Yokoyama et al. (2001).

Common to all authors is that the principal energy release occurs at the X–point reconnection site. This heats the local coronal plasma and accelerates particles. This process causes non–thermal particles to precipitate into the chromosphere where chromospheric plasma 'evaporates' and fills the newly reconnected field lines with dense heated plasma that emits in SXR.

This model fits many of the observational phenomena such as hard X–ray, soft X–ray and Hα features. However, the model does not specify the driver which initially causes the filament to become unstable.

1.3.4.2 The Emerging Flux Model

Another driving force in solar flares is emerging magnetic flux and this is central to the model of Heyvaerts et al. (1977) (Figure 1.11). This model assumes that magnetic flux emerges into a region where pre–existing far connecting (or 'open') field lines have a component that is anti–parallel with the new flux. It consists of three stages:

(a) is the pre–flare heating phase where new magnetic flux emerges.

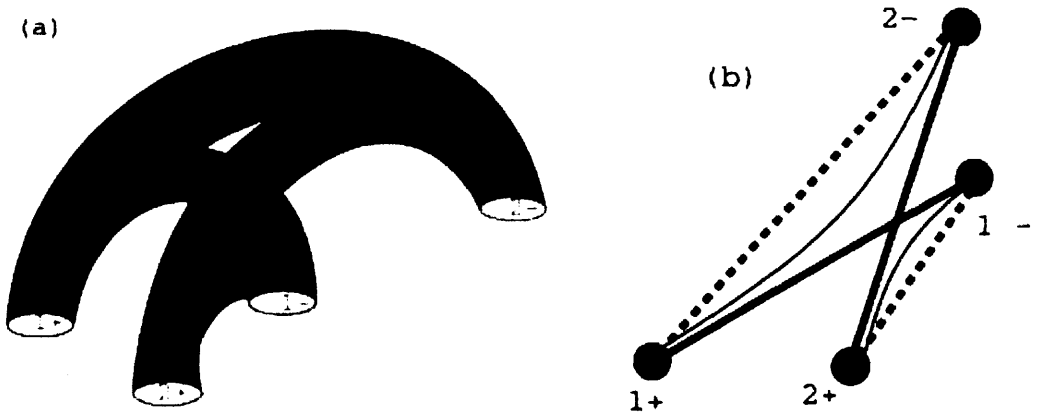

Figure 1.12: A quadrupolar flare model from the interaction of two current carrying loops Melrose (1997)

(b) The rise causes compression of the magnetic field which forms a current sheet between the new and old field. When the current sheet becomes unstable, reconnection (i.e. the impulsive phase) starts, accelerating particles and triggering chromospheric evaporation.

(c) Finally the main phase continues when the current sheet reaches a new steady state with reconnection. Heat conduction channels energy towards the footpoints of the emerging flux loop and material is accelerated (surge) along the far–connecting (open) pre–existing field lines.

1.3.4.3 Quadrupolar Flare Models

The previous models discussed can all be described as 'bipolar' or in the case of Heyvaerts emerging flux model 'tripolar'. This terminology describes the number of footpoints observed in the chromosphere and the photosphere. Each loop footpoint is rooted in a single magnetic polarity, and in a two loop case there would be four separate magnetic footpoints. There is a further case known as 'quadrupolar' flares. These are generally represented by the interaction between two magnetic loops. A theoretical 3D model was developed by Melrose (1997) and was based on the interaction between two interacting current-carrying loops.

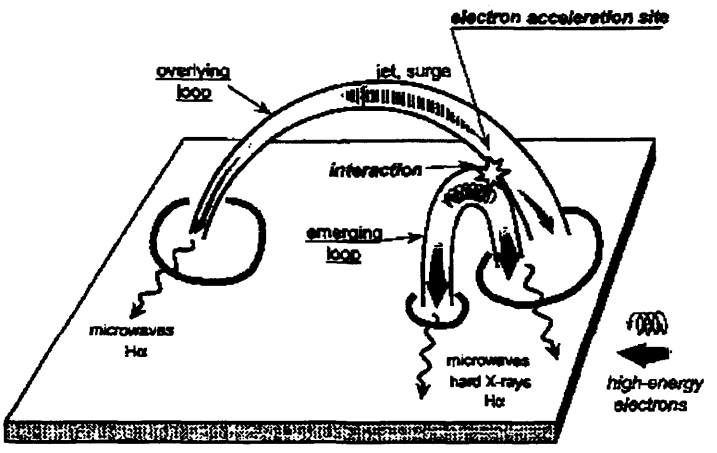

Figure 1.13: A two loop interaction with a common footpoint. This gives the impression that there are only three footpoints but there are actually 4 distinct magnetic footpoints (Hanaoka 1996) This configuration in many respects is like the emerging flux model by Heyvaerts et al. (1977)

The model allows two magnetic loops over a common neutral line to reconnect to form two independent post–flare loops. It is the newly reconnected loops which can be seen through observation. The model is best represented by the cartoon shown in Figure 1.12. Obviously no open field lines are included in the interactions and thus the model cannot explain either a rising filament or the expulsion of a CME. However, most importantly, in the 3D case the loops are not required to be anti–parallel, but simply have some angle between them to allow components of the field lines to be anti–parallel.

One observation of such an interaction was made by Hanaoka (1996), but only three footpoints were resolved. One of the loops was very small, probably because it was in the early stages of emergence, and thus two of the footpoints were probably unresolved. A cartoon illustrating the topology is shown in Figure 1.13.

1.3.4.4 The Breakout Model

The break-out model proposed by Antiochos et al. (1999) requires large–scale quadrupolar magnetic configurations i.e. three parallel magnetic neutral lines. A cartoon of this model can be seen in Figure 1:14. A large overlying magnetic field is illustrated in red,

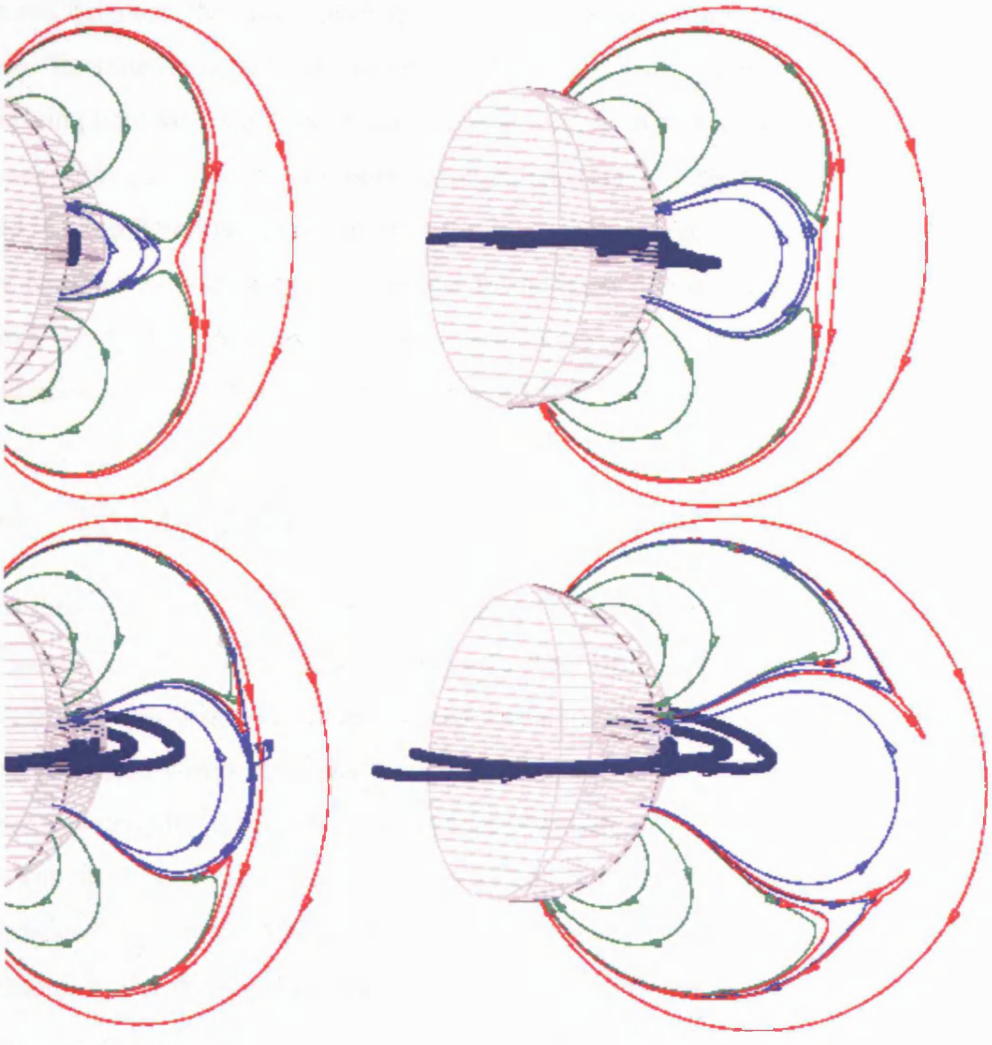

Figure 1.14: Presented here is a time series of cartoons. The central arcade is sheared and begins to expand. As it does so the oppositely orientated overlying fields at the apex begin to reconnect, forming two sets of side loops, removing overlying stabilising magnetic field. This process continues until the sheared core field bursts through. (Antiochos et al. 1999)

and beneath a small arcade is illustrated in blue. When the footpoints of the blue arcade are sheared the arcade begins to expand. As it expands it pushes against the overlying magnetic field. At the top of the arcade the magnetic field direction is anti–parallel to the red field and thus reconnection begins. The reconnection forms two lobes of field lines, illustrated in green, which are over individual neutral lines. As this progresses the overlying field becomes weaker and weaker, until such a time as the arcade, which may be supporting a filament, can burst through, creating a CME. In this case the overlying field is of sufficiently large scale that the footpoints would probably not be observed as any emission would be very weak due to the large distances electrons would have to travel. Under the erupting filament reconnection starts, forming closing–down relaxing field lines, which leads to a 2-ribbon flare or LDE described earlier.

1.4 Thesis Overview

This introduction has shown that solar explosive events are by nature very complex and to understand them fully multi–wavelength observations of a single event are essential. It is true to say that a valuable analysis can be performed in a single waveband, but it is fundamentally important that this information is then cross–referenced with studies in other wavelengths to correctly interpret the observation.

This thesis presents several multi–wavelength studies which probe individual characteristics of flares and CMEs. It will be shown that flares and CMEs are often intimately linked and it is therefore appropriate that they should be studied as complete phenomena. Chapter 3 recognises that there are flares where there is no CME association, thus confined events are examined.

Initially the instrumentation used to study these phenomena is discussed with a basic description of the principles of operation, in addition to how the data can be used. Chapter 2 will also detail common data reduction techniques required to make a full and accurate analysis.

Three chapters follow (3–5) that each presents a distinct and separate research product

which, although not directly linked, relate. To begin with a study of hard X–ray emission from a group of small confined flares is presented followed by a larger explosive event in the next chapter; and then in chapter 5 a much more complex explosive event is considered in many wavebands.

Chapter 3 presents a statistical study of flare hard X–ray footpoint emission and its relationship to magnetic field strength. It has been previously reported by Sakao (1994) that the location of the stronger magnetic footpoint has weaker HXR emission. This chapter presents findings that show a significant number of events contradict this. A much larger sample has been considered here in conjunction with magnetogram data taken not more than 45 minutes from the event time. This larger sample may give an indication of an asymmetric system where the electron injection point is not equidistant from each footpoint.

Chapter 4 describes the study of a single explosive flare event that occurred on the west limb and followed a series of homologous events. High quality observations were available in numerous energy bands that enabled the tracking of an erupting filament seen in *TRACE* 195 Å as it moved through the low corona. Only on very few occasions over the past couple of years have such observations been made (e.g. Gallagher et al. (2002); Foley et al. (2001); Pike & Mason (2002); Williams et al. (2005). A height time profile is presented out to many solar radii through the addition of LASCO C2 and C3 data. By using *RHESSI* it was possible to observe an X–ray source which followed the moving flux rope and is interpreted as the *RHESSI* equivalent of the plasmoid ejection observed by Tsuneta (1997). Coronal Diagnostic Spectrometer (CDS) data were also available for this event and allowed us to observe helical flows, through Doppler shift measurements, in the rising structure. This was then interpreted as a flux rope.

Chapter 5 presents the results of a study into a quadrupolar flare series, which is followed by an LDE. We have seen that, in the classical picture depicted in the model suggested by Melrose (1997), quadrupolar events are expected to remain confined. However, there are numerous indications that there are explosive elements associated with these

quadrupolar events ranging from type–II and type–III radio signatures, to direct observation of a CME in LASCO C2 and C3. It is proposed that this series of events gives rise to an expansion of overlying field which then reconnects with a neighbouring streamer. This gives rise to a large scale CME front while simultaneously allowing the flare series to remain confined. Once the overlying, and restraining, magnetic field from above the active region has been removed in the form of this front, a partial filament eruption can follow.

Finally, the findings of this work are discussed in chapter 6 and are presented with concluding remarks and recommendations for future work.

Chapter 2

Instrumentation

The Sun is very complex, comprising many different types of structures confining plasmas at different temperatures which emit at different wavelengths. By observing these structures with instruments designed to focus on specific wavebands further understanding can be gained of the mechanisms responsible for the differing phenomena. Instruments vary in both their capabilities and scientific objectives and this chapter will discuss the instrumentation used throughout this thesis as well as the data reduction methods used. This includes instrumentation from five different spacecraft, discussed in turn: *Yohkoh*, *RHESSI*, *GOES*, *SoHO* and *TRACE*.

2.1 The Yohkoh Spacecraft

The *Yohkoh* (Ogawara et al. 1991) spacecraft was launched on the 30 August 1991 on the M–3SII–6 launcher by the Institute of Space and Astronautical Sciences (ISAS), Japan. The mission operated successfully for some 10 years until the passage through a near–total solar eclipse zone caused the craft to lose attitude control due to a software defect. As a consequence *Yohkoh* was no longer able to point sunward and eventually lost all remaining battery charge on 14th December 2001.

Yohkoh was a collaborative project between many institutes from Japan, the United States and the United Kingdom. The instruments that were aboard the craft are shown

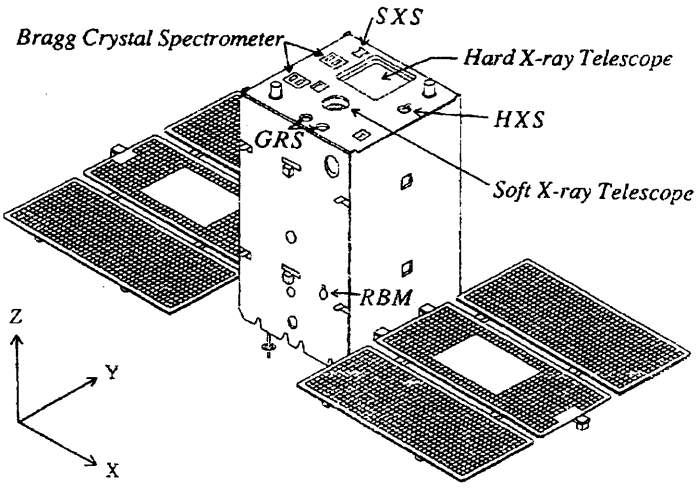

Figure 2.1: Schematic of the instruments on the *Yohkoh* spacecraft, taken from Ogawara et al. (1991).

in Figure 2.1 and comprise the Hard X–ray Telescope (HXT), the Soft X–ray Telescope (SXT), the Wide band Spectrometer (WBS) and the Bragg Crystal Spectrometer (BCS). The WBS itself consisted of four detectors; the Hard X–ray Spectrometer (HXS), the Soft X–ray Spectrometer (SXS), the Gamma Ray Spectrometer (GRS) and the Radiation Belt Monitor (RBM). With this suite of instruments *Yohkoh* was able to perform spectral diagnostics and image features of the X–ray corona.

Yohkoh was launched at solar maximum into a nearly circular Earth orbit with a perihelion distance of approximately 600 km, 31^o inclination and period of 97 minutes. As a result 40 minutes of each orbit was spent in spacecraft night. *Yohkoh* was predominantly below the Earth's radiation belts, but over Brazil and part of the South Atlantic there is a dip in the magnetic field known as the South Atlantic Anomaly. On passage through this anomaly, the high voltage power supplies of the instruments were turned off to protect them from damage caused by this intense radiation.

The following two sections discuss the SXT and HXT instruments in more detail.

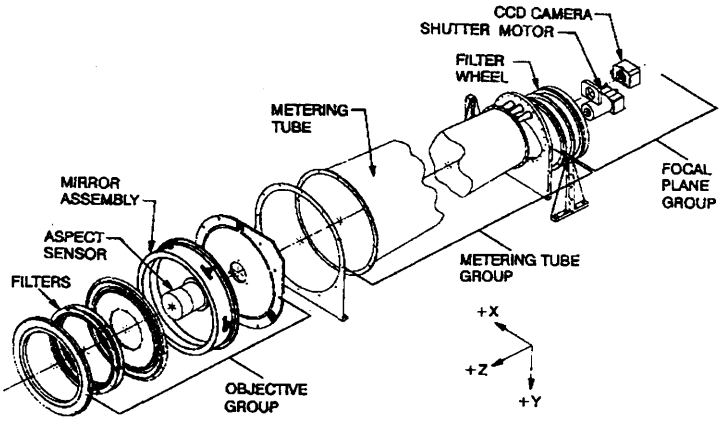

Figure 2.2: Schematic of the Soft X–ray Telescope aboard *Yohkoh* . Taken from Tsuneta et al. (1991). This view shows that SXT components include a detector, a shutter, dual filter wheels, grazing-incidence mirrors to focus the X–rays and a lens for visible light observations.

2.1.1 Soft X–Ray Telescope

The Soft X–ray Telescope (Tsuneta et al. 1991) was a grazing incidence telescope which observed soft X–rays in the energy band 0.25–4.00 *keV* corresponding to a wavelength range 3–60 Å. A grazing incidence telescope focuses X–rays by making use of the fact that they behave like longer wavelength rays if they strike surfaces at a shallow enough angle. The images produced illustrate magnetic structures in the solar corona by measuring the soft X–ray emission produced by the heated plasma trapped in the coronal fields. From these images it was possible to make deductions about the magnetic field topology and geometry, along with the evolution of flaring regions. SXT had a brightness range of $< 10^7$, a best time resolution of 2s, spatial resolution of $\geq 5''$, and was able to image the full solar disc. In addition SXT was able to determine the temperature of structures.

Figure 2.2 shows a schematic of the SXT. The visible light aspect camera failed in late 1992 and thus was not used in this work. The charge coupled device (CCD) had a pixel size of 18μm×18μm corresponding to 2.455$''$ × 2.455$''$ and providing a spatial resolution of 4.91$''$. However, to conserve telemetry the CCD pixels could be binned providing half resolution (2×2 pixels) and quarter resolution (4×4 pixels) images. This allowed SXT to

Front Wheel	Rear Wheel
Open	Open
30 Å at 4310 Å	Al 1265 Å
CCD flood lens	Al/Mg/Mn composite
Opal–glass filter	Be 119 μ m
140 Å at 458 Å	Al 11.6 μ m
8.05% mesh	Mg 2.52 μ m

Table 2.1: List of filters mounted on the dual filter wheel of SXT, taken from Tsuneta et al. (1991) The rear filter wheel holds the X–ray analysis filters, and the front wheel holds the filters to block visible and ultra–violet light.

make global studies, but in addition the more dynamic small scale could be observed in greater detail using smaller frame images. The full frame images (FFI) of the whole Sun were taken with a cadence of 5–10 minutes, and partial frame images (PFI) were taken with a cadence of a few seconds.

The CCD used by SXT functioned in a charge collection mode. As a result the read out charge represented the energy of the photon flux integrated over the exposure time, and therefore not number of photons. The charge had to be converted to a data number (DN), where 1 DN corresponded to the detection of a single photon of wavelength 34 Å.

The SXT had two entrance filters which could exclude visible and ultra–violet light, in addition to minimising stray light into the instrument. Near the focal plane, in front of the CCD detector, was a dual filter wheel. The filters mounted in this wheel are detailed in Table 2.1. They consisted of five metallic filters on the rear wheel designed to separate the different X–ray energies. These were broken down into three *thin* filters (Al 1265 Å, Al/Mg/Mn composite, and Mg 2.52 μm), and two *thick* filters (Al 11.6 μm and Be 119 μm). This gave SXT the capability of imaging plasma in a temperature range of $>1\times10^6$ to $<50\times10^6$ K.

In Figure 2.3(a) the response of SXT for the different filters assuming an emission measure (a measure of the amount of plasma available to produce the observed flux which

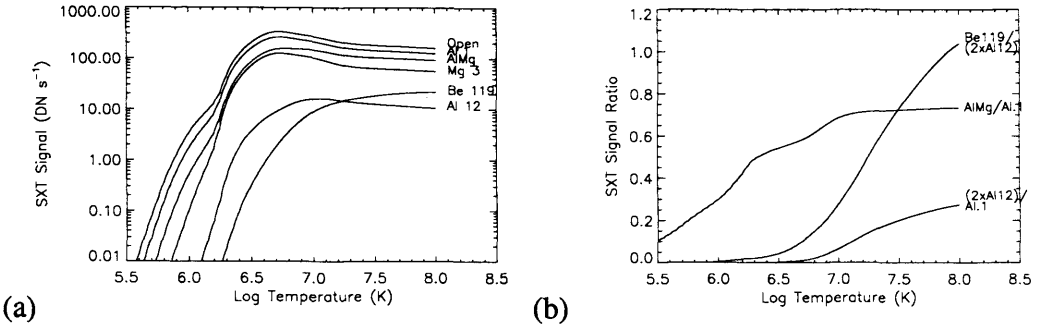

Figure 2.3: (a) The total SXT signal as a function of temperature for the open filter position of the front filter, and each of the X–ray analysis filters. The curves assume an emission measure of 10^{44} cm^{-3}. (b) The ratios of the SXT response functions. The effective observation time has been doubled for some filters where indicated.

is the product of the square of the electron number density and the volume of emission)of 10^{44} cm^{-3} is shown. Figure 2.3(b) shows the ratios of these functions for selected filter pairs as indicated in the plot. Using this information it is possible by using ratios of the filter pairs, to determine the temperature of the plasma, assuming that the plasma is isothermal, as detailed in Hara (1996).

The SXT data had to be calibrated before any analysis could be carried out. This included the subtraction of the CCD dark current, the flagging of saturated pixels, the removal of spacecraft jitter, the correction for spacecraft roll and the removal of spikes and cosmic rays from the images. This could be done through the use of IDL (Interactive Data Language) and the standard software which is part of the SolarSoft package using the sxtprep routine. Following these corrections the images could also be normalised for exposure time to provide continuity in the data set.

2.1.2 Hard X–Ray Telescope

The Hard X–ray Telescope (Kosugi et al. 1991) was a Fourier–synthesis imager capable of imaging in four energy bands simultaneously. These energy bands were separated into 14–24 *keV* (the LO channel), 24–35 *keV* (the M1 channel), 35–57 *keV* (the M2 channel) and 57–93 *keV* (the HI channel). HXT was designed to enable the study of the electron

acceleration mechanism, location and propagation in flaring loops, and the location of energy deposition. In flare mode the telescope could make observations every 0.5 seconds and had a spatial resolution of 5″.

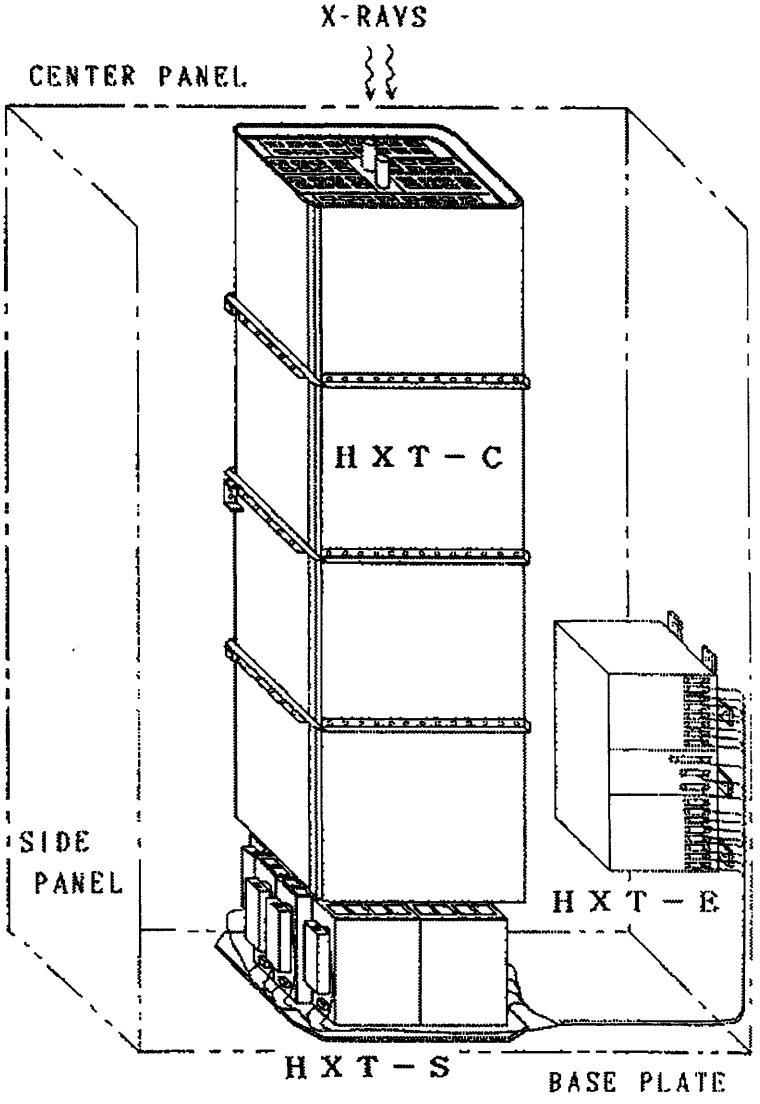

Figure 2.4: Schematic of the Hard X–ray Telescope aboard *Yohkoh* taken from Kosugi et al. (1991). There are three sections; the collimator (HXT–C), the detector assembly (HXT–S) and the electronics unit (HXT–E).

HXT essentially comprise three major sections as shown in Figure 2.4. These were the collimator (HXT–C) , the detector assembly (HXT–S) and the electronics (HXT–E).

The collimator was the X–ray optics part of the telescope with an X–ray grid plate at either end. These plates were comprised of 64 sub–collimator grids made from 0.5 mm thick tungsten.

HXT–S was positioned below HXT–C and consisted of 64 individual detector modules, one for each sub–collimator in HXT–C. These non–position sensitive detectors consisted of NaI(Tl) scintillation crystals and a photomultiplier tube. It was the purpose of each of these sub–collimators to measure a particular spatial Fourier component of the X–ray brightness distribution.

To obtain the solar flare HXR image it is necessary to reconstruct images from the HXT data. In principle a 2D inverse Fourier transform of the spatially modulated photon count data is performed. This is because the measured hard X–ray counts can be expressed as spatial Fourier components of the hard X–ray signal, as detailed in Sakao (1994). However, HXT has fewer detector pairs than are needed. This means that a direct inverse transform is not feasible without producing significant noise and spurious signals in the recovered image. However, there are methods that perform the inversion with incomplete sets of measurements and two of the most favoured are the Maximum Entropy Method (MEM Gull & Daniell 1978; Willingdale 1981) and the Pixon method (Pina & Puetter 1993; Metcalf et al. 1996). Throughout Chapter 3 images are reconstructed by using the maximum entropy method. This was largely due to the long time period required to make images by the Pixon method. With such large numbers of events it would have been difficult to use the Pixon method across the board. The maximum entropy approach seeks the 'most plausible' and smoothest solution that is consistent with the observations. To obtain good images, photon counts of a few hundred per sub–collimator are required, which means integration times of many seconds are needed to ensure good counting statistics. These images can be reconstructed using software from the SolarSoft archive. This software allowed the user to set the minimum number of counts in a chosen channel (in this case 200 in the M2 Channel) as threshold for the making reliable images. A series of images was then produced in all of the channels. The routine was improved by Sato et al. (1999) and it was also empirically determined that the reconstructed images

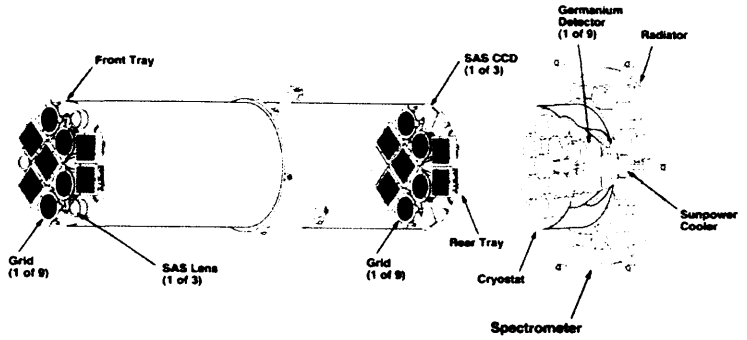

Figure 2.5: Schematic of *RHESSI* (Lin et al. 2002).

were accurate down to between 10 and 20% intensity levels.

HXT can also act as a wide band spectrometer. Data from all 64 detectors in one energy channel can be summed to provide an HXR flare spectrum. This spectrum can then be fitted with either a power law or thermal spectrum to determine the photon spectrum.

2.2 *RHESSI*

The *Reuven Ramaty High Energy Solar Spectroscopic Imager* (*RHESSI*, Lin et al. 2002) is a NASA small explorer (SMEX) mission that was launched in February of 2002. *RHESSI* is a spin stabilised spacecraft and is in Earth orbit inclined at 38 degrees to the equator.

RHESSI is a single instrument comprising an imaging system, spectrometer and instrument data processing unit containing the electronics. It was principally designed to study the acceleration of electrons, protons and heavier ions in solar flares. In addition, it can be used to study the propagation and evolution of energetic particles in flares, as well as to determine the relative abundances of accelerated and ambient ions in flares. These objectives can be achieved by the simultaneous production of high resolution images and spectroscopy of solar flares from 3 keV X–rays to 17 MeV gamma rays with high time resolution.

2.2.1 *RHESSI* Imaging

A very detailed description of the *RHESSI* imaging concept can be found in Hurford et al. (2002), which explains all aspects from instrument design through to image reconstruction algorithms. Included here is a brief summary of the imaging process.

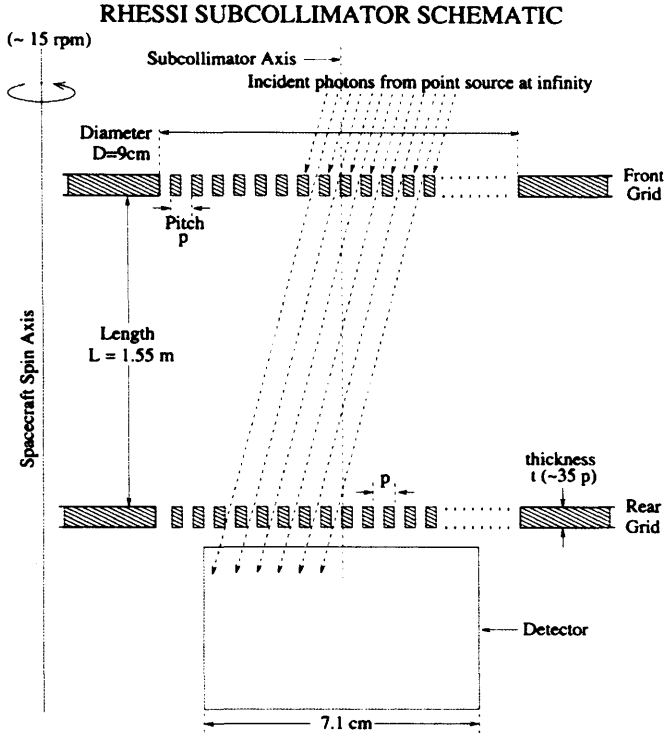

Figure 2.6: Schematic of *RHESSI* subcollimator showing representative incident photons (Hurford et al. 2002)

The only practical method of combining high angular resolution (~ 2″) with high sensitivity and large energy range, within the cost, mass and launch constraints of a small satellite was to use collimator–based Fourier–transform imaging. The schematic in Figure 2.5 shows a set of nine bi-grid subcollimators, each of which consists of a pair of widely separated grids. These are each in front of a corresponding non-imaging X–ray/gamma–ray detector. The grids are X–ray–opaque slats separated by transparent slits. Figure 2.6 is an illustration of the transition through the grid pair of the X–rays. It is

clearly seen that the transmission is dependent on the direction. If the incident direction changes with time, that transmission of the grid pair is modulated in time. The shadow of the slats in the top grid alternately falls on the slits or slats in the rear grid. As the direction of the source changes the transmission is time–modulated from zero to 50% and back again. One cycle of this transmission occurs for a source angle change of Pitch/Length. When the source is off axis, rotation of the spacecraft allows a relative shift in angle of the source. The detector and data system records the arrival time and energy of each photon detected, allowing the modulated count rate to be determined as a function of rotation angle.

There are a range of reconstruction algorithms that can be used for *RHESSI* imaging. The initial approach is to use a 'back projection' algorithm, which generates an initial estimate of the image. This represents a convolution of the source with the instrumentational response; hence there are side-lobes. The image quality can be improved by using a method such as Clean (Hogbom & Brouw 1974) or Pixons ((Pina & Puetter 1993; Metcalf et al. 1996)). These make broad assumptions about the characteristics of the source, and then proceed in a cycle of predicting the modulation profile for a test image and comparing to the observed modulation. Subtle changes are then made to the test image until agreement is reached.

Back–projection is basically a 2D inverse Fourier transform that can be used to reconstruct a dirty image. If you attempt to run a back–projection process on the data from a limb flare concentric rings would be observed around the source. This is caused by incomplete sampling of the Fourier plane. However, most noticeable would be the 'mirror' source. This is a consequence of not having both the 'sine' and 'cosine' subcollimators. In practice this is not a problem as the region studied usually would only include the real source. However, improved images can be obtained using an algorithm such as Pixons.

The Pixon method ((Pina & Puetter 1993; Metcalf et al. 1996)) is a technique which removes the side-lobe pattern while reducing spurious sources. The goal of this algorithm is to construct the simplest model for the image that is consistent with the data. As the simplest model, the derived image would be artifact free with no spurious sources.

Table 2.2: *GOES* soft X-ray classification of flares

GOES Class	Peak Flux (erg cm^{-2} s^{-1})
A	10^{-5}
B	10^{-4}
C	10^{-3}
M	10^{-2}
X	10^{-1}

This method differs from MEM, which imposes a global condition that minimises the difference between the image and a grey map in a manner that is consistent with the data. The Pixon method, instead, imposes a local constraint. Each parameter is determined using a larger fraction of the data, hence improving the image photometry and positional accuracy. However this method is an order of magnitude slower.

2.3 *Geostationary Operational Environmental Satellites*

Geostationary Operational Environmental Satellites (*GOES*) are operated by the National Oceanic and Atmospheric Administration (NOAA). They are meteorology satellites, but additionally they carry a Space Environment Monitor (SEM) to measure solar X-rays, energetic particles and the Earth's magnetic field at the satellite's position. The data collected by the SEM is used to classify flares relative to the soft X-ray flux in the wavelength ranges 0.5–4 and 1–8 Å . The classifications shown in Table 2.2 refer to flux in the 1-8 Å range. The measurements of the X-ray flux from the Sun are made with ion chamber detectors. These X-ray flux measurements are used throughout this thesis.

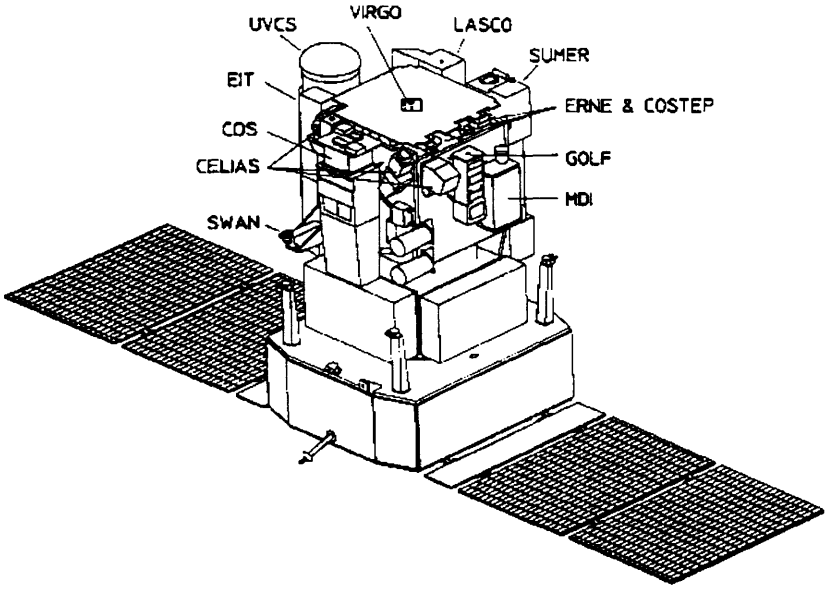

Figure 2.7: A schematic of the *SoHO* spacecraft and its 12 instruments (Domingo et al. 1995).

2.4 The *SoHO* Spacecraft

2.4.1 Introduction

The Solar and Heliospheric Observatory (*SoHO*, Domingo et al. 1995) is a joint mission between the European Space Agency (ESA) and the National Aeronautics and Space Administration (NASA). The mission carries a payload of 12 complementary instruments, four of which will be discussed in detail within this section. A schematic of *SoHO* can be seen in Figure 2.7. The mission was principally designed to study the solar interior (through helioseismology), coronal heating mechanisms, and the acceleration process of the solar wind.

SoHO was launched on the 2rd December 1995 on an Atlas II-AS rocket into a low Earth parking orbit. From here it was injected into a transfer orbit to the Earth–Sun L1 Lagrangian point. The Lagrangian points are the five positions in space where a small object can be stationary with respect to two larger objects (such as, in this case, a satellite

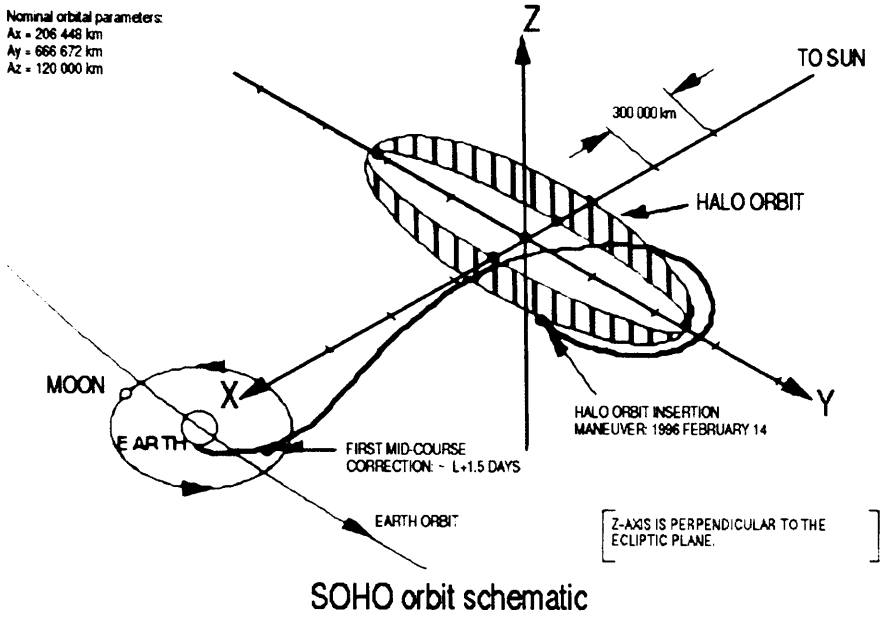

Figure 2.8: The *SoHO* halo orbit around the L1 point

with respect to the Sun and Earth). After four months the spacecraft entered a halo orbit around the L1 point (Figure 2.8). From here it enjoys uninterrupted views of the Sun. The halo orbit has a period of approximately 180 days and has semi-diameters of 200,000 km in the ecliptic in the Earth-Sun direction, 650,000 km in the ecliptic perpendicular to the Earth-Sun line and 200,000 km out of the ecliptic. This positioning also allows *SoHO* to take in-situ measurements of the solar wind as it is outside the Earth's magnetosphere.

The spacecraft maintains attitude control by using Sun sensors, star trackers and reaction wheels; while orbit adjustments are controlled by a hydrazine propulsion system. The pointing is accurate to 10″, and the pointing stability is better than 1″ over 15 minutes.

2.4.2 The Extreme-Ultraviolet Imaging Telescope

The Extreme-Ultraviolet Imaging Telescope (EIT; Delaboudinière et al. 1995) was primarily designed to study the dynamics and evolution of coronal structures over a wide range of timescales, sizes and temperatures, to investigate the mechanisms responsible

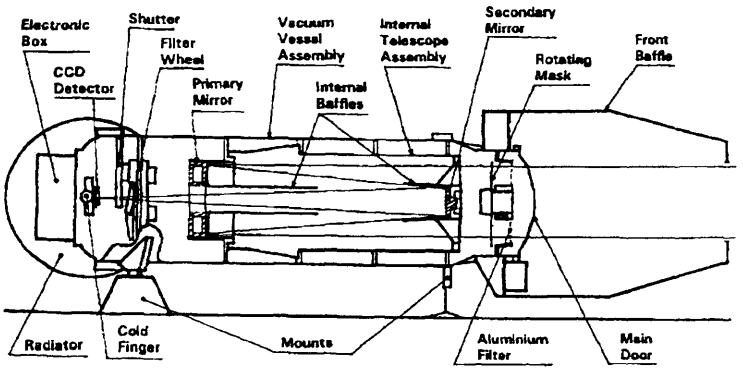

Figure 2.9: Schematic of EIT from Delaboudiniére et al. (1995)

for coronal heating and solar wind acceleration. It is a normal incidence telescope, based on the Ritchey-Chretien design (Bottema & Woodruff 1971). A schematic of the telescope can be seen in Figure 2.9. The main subsystems consist of primary and secondary mirrors, with multi–layer coatings, a rotating mask, filter wheel, electronics box and CCD detector.

EIT provides full-disk images of the solar transition region and corona at four wavelengths (304 Å, 171 Å, 195 Å and 284 Å). It has a field of view of 45' × 45' with a CCD size of 1024 × 1024 21 μm pixels, giving the system a spatial resolution of 2.62″ pixel^{-1}. This is capable of resolving features down to a scale of ~4000 km. In a similar way to SXT, pixels can be binned to produce half resolution images (2 × 2 pixel summation) and quarter resolution images (4 × 4 pixel summation), to conserve telemetry. This is required as the instrument shares the telemetry rate with LASCO.

The filters in the filter wheel are listed in Table 2.3 and the wavelength response profiles are shown in Figure 2.10.

2.4.2.1 Data Calibration

The EIT data are received as fits files from the *SoHO* archive. The data can then be read into the EIT suite of SolarSoft software where it is then calibrated through the 'eit_prep'

Table 2.3: The table shows the centre of the bandpass for each filter, the strongest ion emission at that wavelength and the peak formation temperature of the ion

Wavelength	Ion	Peak Temperature (K)	Observations
304 Å	He II	8.0×10^4	Chromospheric network; coronal holes
171 Å	Fe IX, Fe X	1.3×10^6	Corona/transition region boundary
195 Å	Fe XII	1.6×10^6	Quiet corona
284 Å	Fe XV	2.0×10^6	Active regions

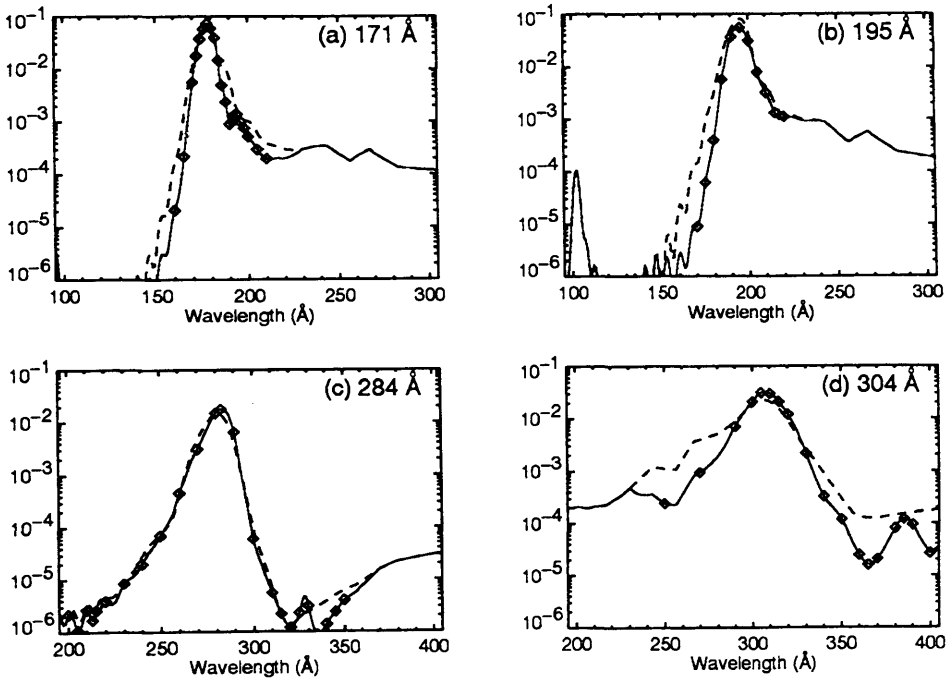

Figure 2.10: Wavelength response of EIT in each of the four bandpasses from Delaboudinière et al. (1995)

routine within this package. This routine degrids the image (to remove artifacts from the filter) and normalises for exposure time. In addition flat fielding (corrections for pixel to pixel variations in the CCD) of the image and subtraction of the dark current (thermal noise) are performed. This routine produces calibrated images which can be used for analysis. The image values are in units of data numbers (DN) but not in physical units. The translation is not a trivial one as each bandpass is broad and as such has numerous lines which contribute at various levels to the emission. For the data within this thesis a translation of units was not necessary as only the relative intensities are considered.

2.4.3 The Large Angle and Spectroscopic Coronagraph

The Large Angle Spectroscopic Coronagraph (LASCO, Brueckner et al. 1995) originally comprised three coronagraphs which together imaged the corona from 1.1 to 30 solar radii. However, the inner most coronagraph (C1) failed in 1998 and is therefore not used in any of the observations in this thesis and is not discussed further here.

A coronagraph allows the scientist to observe the solar corona as if under eclipse conditions by masking the bright solar disc. Stray light is a major problem but by using the space based coronagraphs it is possible to limit this to that scattered by the instrument. LASCO C2 and C3 are externally occulted; a disk assembly completely shadows the objective lens from photospheric light. Each of these coronagraphs uses a 1024×1024 pixel array CCD.

A schematic of the C2 coronagraph is shown in Figure 2.11. C2 is able to image from 1.5–6.0 solar radii. As an externally occulted instrument stray light is minimised but not entirely eliminated. Thus prior to launch, stray light values were measured at the Naval Research Laboratory. They found that stray light was expected to be an order of magnitude below the coronal levels. Also to minimise the stray light from diffraction at the entrance aperture a serrated design was used, thus diffracted light does not fall on the objective lens.

C3, also externally occulted, images from 3.7–30.0 solar radii and a schematic is

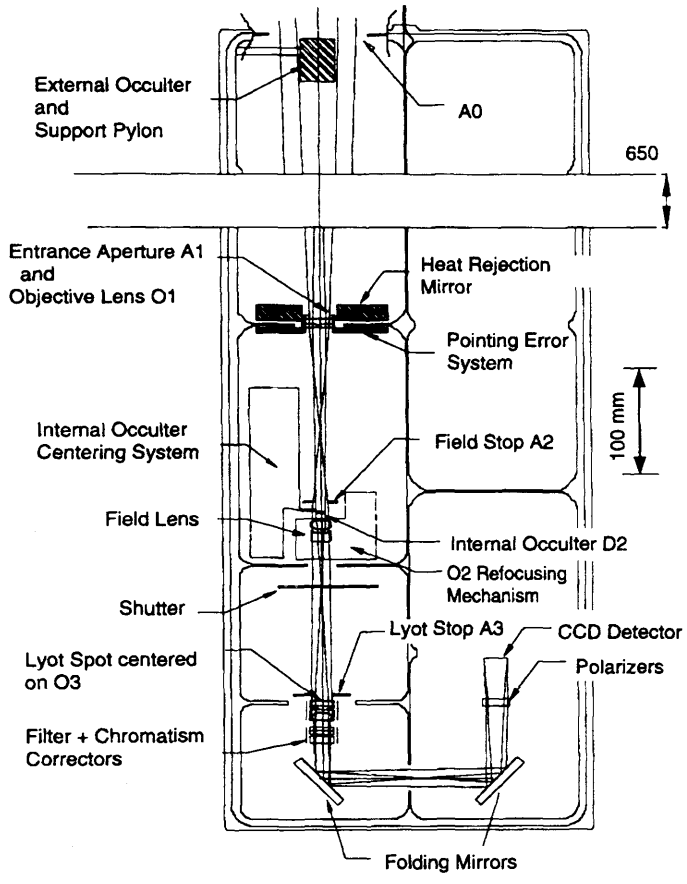

Figure 2.11: Schematic of LASCO C2, taken from Brueckner et al. (1995)

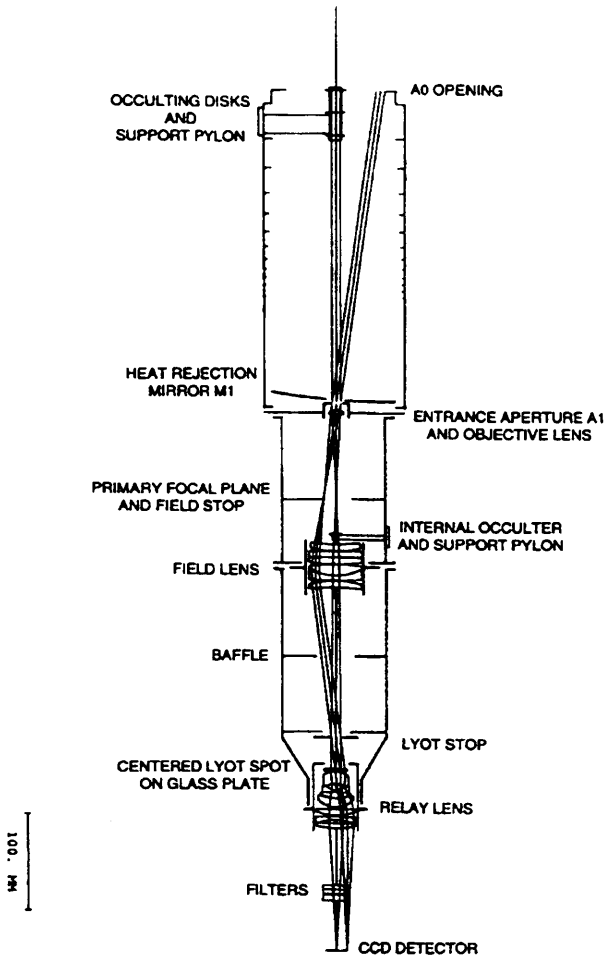

Figure 2.12: Schematic of LASCO C3 Brueckner et al. (1995)

shown in Figure 2.12. Extra precautions are required to minimise stray light with this coronagraph as the intensity of the corona is extremely low at such large distances and it would impact highly on the images. Thus extra discs are added in between the occulter and the objective lens to remove diffracted light.

Neither of these coronagraphs has any real spectroscopic abilities, but broadband colour filters and polarisers are present to allow the separation of the F (dust) and K (electron) coronae.

2.4.3.1 Data Calibration

The LASCO consortium offers both level 0.5 uncorrected data and level 1.0 calibrated files for quantitative scientific analysis. These data are corrected for flat field, geometric distortion and stray light. However, to detect CMEs the raw images are commonly used. If the CME is faint it can be enhanced through the use of difference imaging. This allows the observer to differentiate between the faint material from the stable coronal structure and the CME feature. This can take the form of running difference (one image taken from the next) or base difference (an image prior to the event is subtracted).

2.4.4 The Solar Oscillations Investigation – Michelson Doppler Imager

The Solar Oscillations Investigation – Michelson Doppler Imager (MDI, Scherrer et al. 1995) is primarily a helioseismological instrument. It is designed to probe the solar interior by detecting photospheric oscillations. A schematic of this instrument can be seen in Figure 2.13. In addition, and importantly for this work, MDI is capable of measuring line of sight magnetic fields. This is possible as the line profile produced is affected by magnetic field.

In the presence of a magnetic field electron energy levels can become separated. If we think of the orbiting electron as being a small electrical current it has an associated magnetic field. If this is aligned with the external field the orbit has a higher energy and

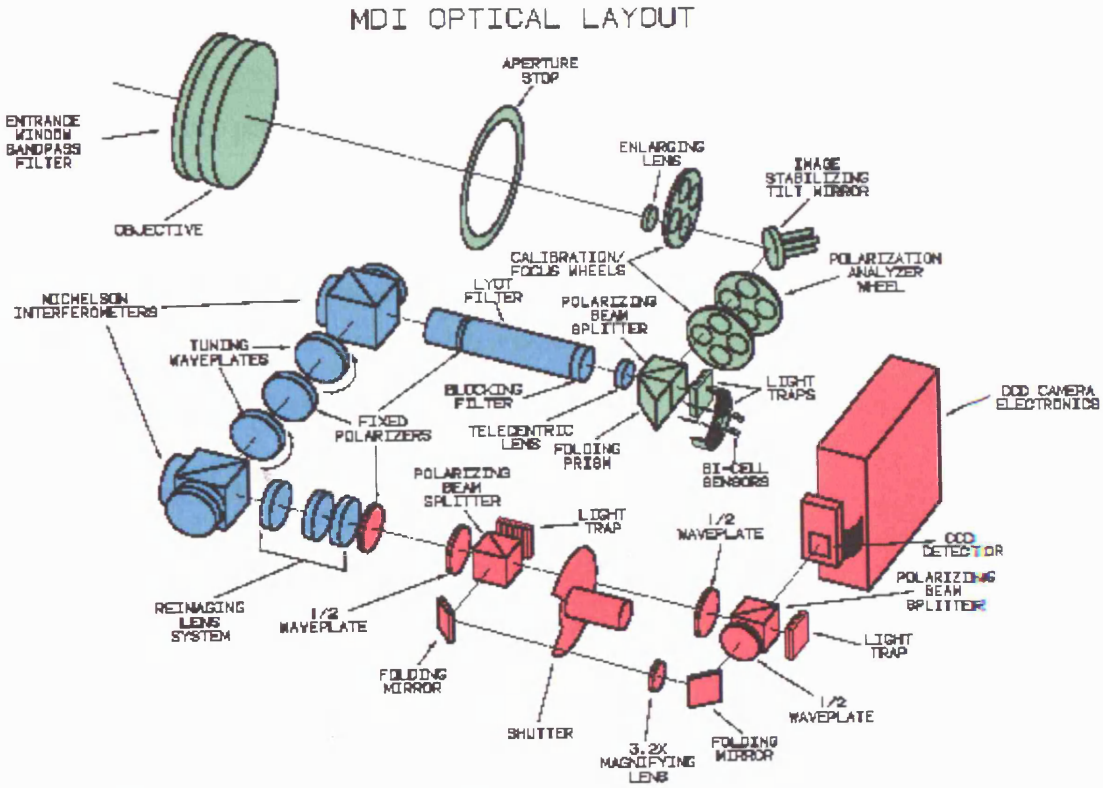

Figure 2.13: Schematic of the Michelson Doppler Imager, courtesy of Stanford University

vice versa. Thus a spectral line would appear as a doublet with the splitting of energy levels proportional to the magnetic field strength. Fortunately the two levels are also oppositely circularly polarised, enabling easy measurement with MDI.

MDI uses a refracting telescope to feed light through polarisers and filters to measure the linear and circularly polarised light. This results in a 94 mÅ bandpass centred around the mid-photospheric Ni I 6768 Å solar absorption line. The Doppler shift in the absorption line can be measured in each of the left and right circularly polarised light. The difference between these shifts is a measure of the Zeeman splitting of the line. This is in turn roughly proportional to the line–of–sight component of magnetic flux density averaged over a resolution element.

MDI operates with a 1024 × 1024 pixel array CCD, with a pixel size of 1.978″ × 1.978″. It obtains full disc magnetograms every 96 minutes. It can work also in a high resolution mode, where the beam is magnified just before the CCD by a factor of 3.2. In this mode the pixel size is 0.625″ × 0.625″ and has a fixed field of view of 10.5″ ×10.5″.

2.4.4.1 Data Calibration

Calibrations of the MDI data are performed before the data becomes generally available, thus the pixels are representative of magnetic flux density. Most important when studying magnetograms is to remember that they are line of sight images and since magnetic field is dominantly perpendicular to the solar surface, disc position is very influential. There are, however, many more issues involved in interpreting MDI data, and a detailed description follows in Section. 3.3.3.

2.4.5 The Coronal Diagnostic Spectrometer

The Coronal Diagnostic Spectrometer (CDS, Harrison et al. 1995) is a dual–mode Extreme Ultra-Violet (EUV) spectrograph instrument on *SoHO* . The primary goal of this instrument was to determine how the corona is heated and how the solar wind is accelerated by probing the coronal plasma through its EUV emission. This instrument gives

the opportunity to determine plasma temperature, density, flow velocity and abundance at good spatial and high temporal resolution. This can be achieved by viewing the Sun in the wavelength range of 150–800 Å which contains emission lines with formation temperatures in the range of 10^4–10^6K.

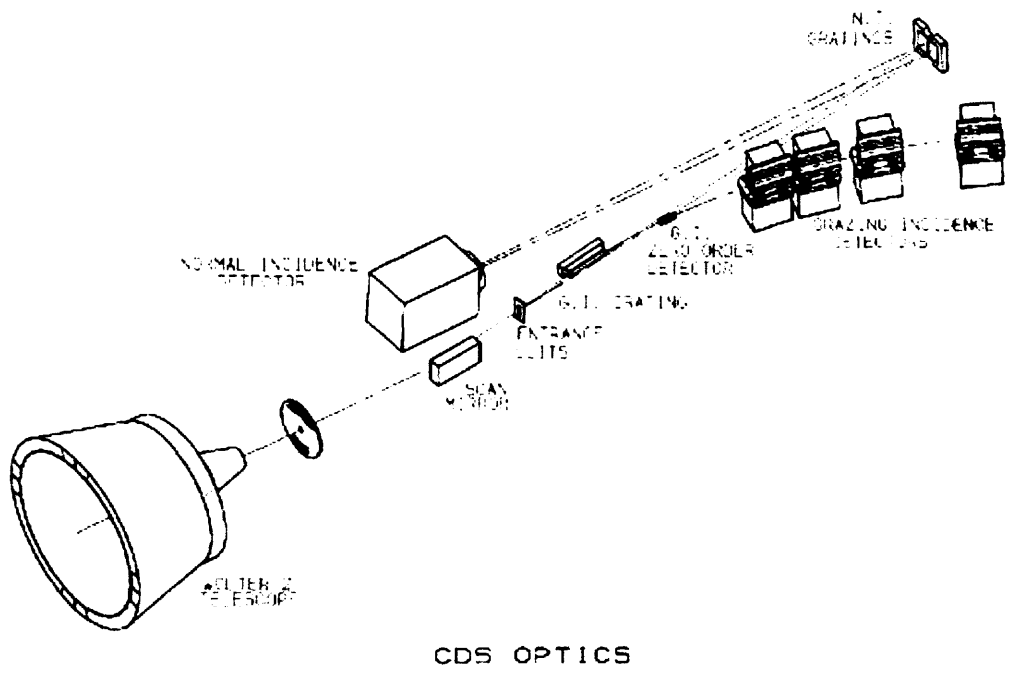

Figure 2.14: Optical schematic of CDS (Harrison et al. 1995)

This wavelength range cannot be serviced by a single instrument, thus a dual system is in operation and comprises the Grazing Incidence Spectrometer (GIS) and the Normal Incidence Spectrometer (NIS). This gives the advantage of the wide wavelength range of GIS and the imaging capabilities of NIS. The total field of view of the telescope is 4 arc-minutes square and can be re–pointed through an angle of $\pm 0.75^o$ to allow full disc coverage.

An optical schematic can be seen in Figure 2.14. The system is fed by a grazing

incidence telescope. Common entrance slits supply a focused beam that is split, to provide one for each spectrometer. Only the NIS data are used in this thesis.

2.4.5.1 Normal Incidence Spectrometer

Two toroidal gratings are used to reflect the beam in the NIS and focus it onto an intensified CCD. A small out–of–plane tilt is imposed onto the gratings allowing two spectral bands to be displayed on a single CCD one above the other. The image in the upper half covers the wavelength range of 310–380 Å at 0.08Å resolution and the lower image covers the wavelength range of 520–630 Å at 0.14 Å resolution. These images are determined by the entrance slit and to build a bigger picture the scan mirror is moved in intervals of 2″ in the work studied in Chapter 4.

2.5 The *TRACE* Spacecraft

2.5.1 Introduction

The *Transition Region And Coronal Explorer* (*TRACE* Handy et al. 1999) was launched in April 1998 as part of the NASA Small Explorer (SMEX) programme. It was put into a Sun–synchronous orbit, allowing an uninterrupted view of the Sun for 9 months of the year. During the remaining 3 months the spacecraft is in 'eclipse season', where part of the orbit is occulted by the Earth.

The *TRACE* observatory is a single instrument spacecraft, comprising a normal incidence imaging EUV telescope (Figure 2.15) that views the Sun through three narrow–band EUV filters and several UV filters (Table 2.4). This combination of filters enables it to explore the dynamics and evolution of the solar atmosphere from the photosphere to the corona.

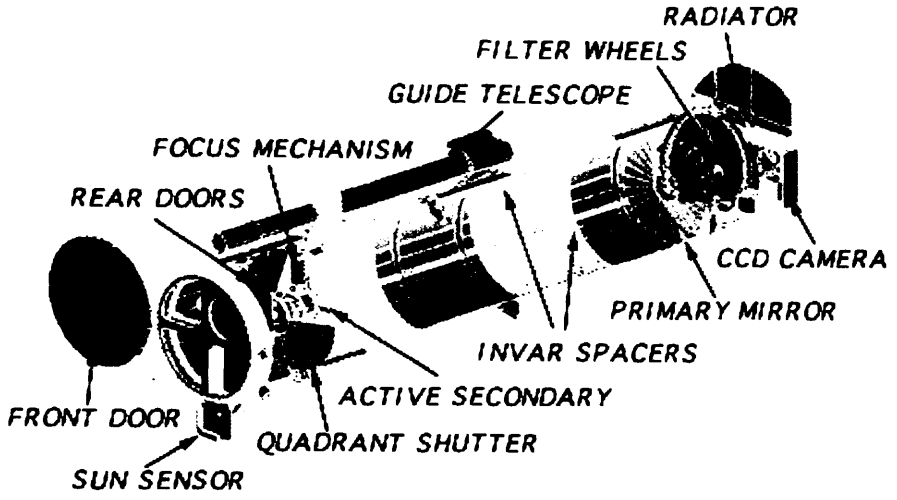

Figure 2.15: Schematic of *TRACE* from (Handy et al. 1999)

2.5.2 The *TRACE* Telescope

The instrument is a Cassegrain telescope with a 30cm aperture and a 8.5 × 8.5 arc–minute field of view. It boasts a spatial resolution 1″ (0.5″ pixel^{-1}) and a best cadence of ~3 seconds. It has four entrance quadrants at the aperture, which are selectively opened by the rotation of the open-quadrant shutter. The aperture is coated so as to reflect all but UV and EUV light. There is one quadrant for each EUV passband and the remaining quadrant is for the UV passbands. These are matched to corresponding quadrants of the primary and secondary mirrors. The secondary mirror can correct for pointing 'jitter' to within 0.1″. There are then two filter wheels at the rear of the telescope which can be combined in various ways to achieve either different levels of response in the EUV quadrants or different passbands in the UV quadrant. The wavelength response of *TRACE* can be seen in Figure 2.16.

2.5.2.1 Data Calibrartion

The data are stored as fits files which can be manipulated with SolarSoft (SSW) routines. These *TRACE* data files can be calibrated through the use of the 'trace_prep' routine. This

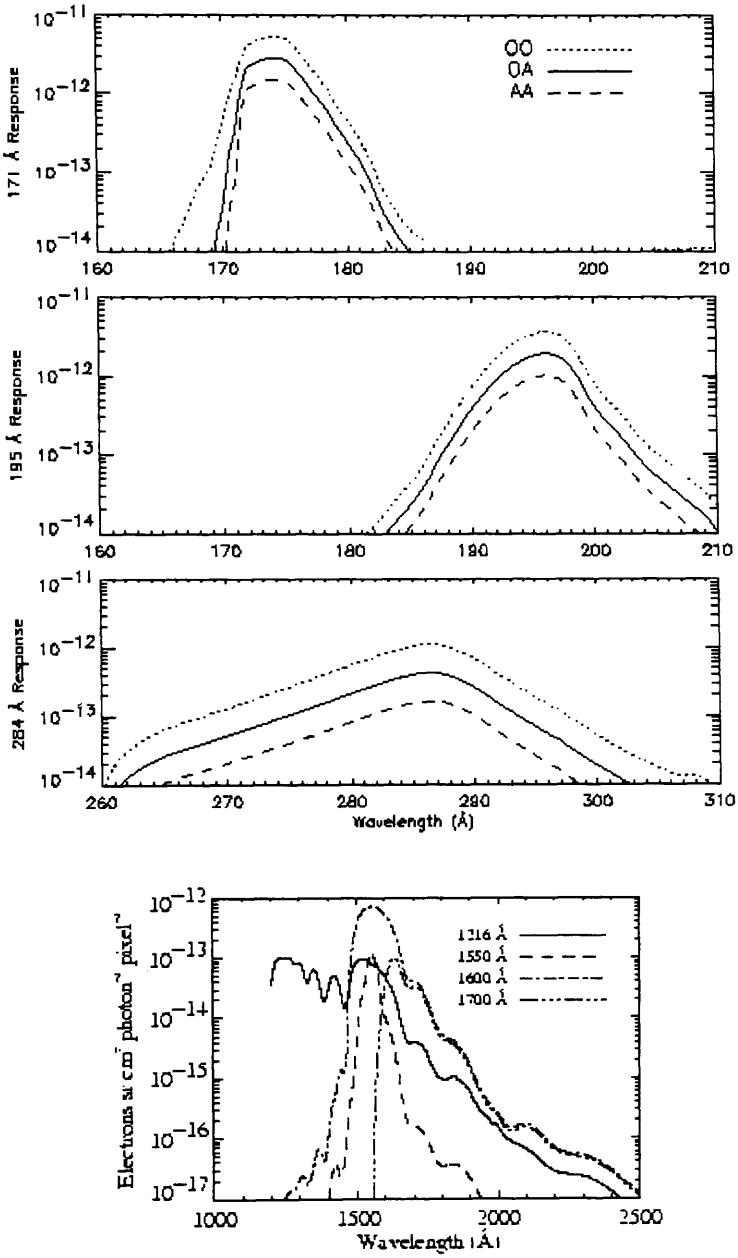

Figure 2.16: Wavelength response of *TRACE* (Handy et al. 1999)

Table 2.4: *TRACE* observation passbands

Wavelength (Å)	Target species	Bandwidth (Å)	Formation Temperature Log (K)
171	Fe IX/X	6.4	5.2–6.3
195	Fe XII	6.5	5.7–6.3
284	Fe XV	10.7	6.1–6.6
1216	H I (Lyα)	84.0	4.0–4.5
1550	C IV	20	4.8–5.4
1600	C I/Fe II/UV cont.	275	3.6–4.0
1700	Continuum (UV)	200	3.6–4.0
5000	Continuum (visible)	broad	3.6–3.8

routine subtracts the dark pedestal and current from each image. In addition it fills any pixels of zero value with the mean pixel value for the entire image and also replaces near saturated pixels with a value 4095. These actions are performed by default.

There are also a number of options that can be added to this process. Throughout this work the data were also corrected for pointing in each channel and normalised for exposure time. There is the option within this routine to remove spikes, but it has been found that the routine is very harsh. It can strip meaningful data from the image cube. Instead 'ssw_unspike_cube' which was written by Markus J. Aschwanden, was used which removes spikes based on the image before and after the image being corrected. This was much more effective and removed only the cosmic rays and not the data. The affected pixel is then replaced with the average of the nearest 2 temporal pixels if it is a cosmic ray.

TRACE suffers sometimes from a serious pointing issue. This was corrected by cross–correlating the images with EIT images following the technique described by Gallagher

et al. (2003). A brief description follows.

An EIT 195 Å and a *TRACE* 195 Å image are taken as close in time as possible (in this work, a few seconds). Then a region containing a feature common to both images is extracted. In order for cross-correlation to work both images must have the same number of pixels. Therefore, the EIT image, with the lesser number of pixels, is rebinned to have the same dimensions as the *TRACE* image. Then by using the cross–correlation routine, 'get_correl_offsets', the pixel offsets are determined and the correction is applied to all the *TRACE* images. This has the result of correcting the pointing to match that of EIT.

This whole process is limited by the selection of the reference images. It is important that clearly common features are identified and that there is very little time between the images. This will ensure that the best possible alignment can be achieved.

Chapter 3

Relating Magnetic Field Strengths To Hard X-Ray Footpoints

3.1 Introduction

Typically hard X-ray emission sites, during solar flare events, form at the footpoints of flare loops; sites of non-thermal energy deposition in the lower atmosphere. The flaring loops are often considered as double-ended magnetic bottles which confine non-thermal particles through the Lorentz force, a consequence of the converging magnetic field at the loop ends. These magnetic footpoints are rooted in the photosphere, where the magnetic field is known to be higher than the coronal component at the loop apex and particle trapping is a possibility.

The trapping efficiency is a function of the magnetic mirror ratio ($R = B_{foot}/B_{apex} > 1$) and also the conservation of angular momentum. A higher value of R indicates greater trapping efficiency, which determines the amount of radiation emitted from particles within the trap. Trapped electrons can produce gyro–synchrotron emission, while any leakage determines the level of HXR emission through thick target bremsstrahlung in the chromosphere. In solar flares we expect that precipitation will be greatest at the weaker

[1]This work has been published in A& A by Goff et al. (2004)

magnetic footpoint, where convergence is smallest if we assume magnetic field at the apex is the same for both footpoints. Conversely then, HXR intensity would be lower in regions of strong magnetic field. This relationship has been observed in flares such as those studied by Sakao (1994). He studied a sample of events where two HXR sources were situated on either side of a magnetic neutral line. He found that four out of five events, with supporting magnetogram data, had this arrangement. The fifth event showed the opposite behaviour. However, the magnetogram data for this event was approximately eleven hours old at the time of the flare peak, therefore it was more difficult to assess the magnetic field and HXR intensity relation accurately.

This 'unusual' behaviour has since been reported by Asai et al. (2002) in a single two ribbon flare, observed on 10th November 1998. In this case the two HXR sources occurred in the strong magnetic regions, whereas the weaker magnetic regions situated under Hα kernels had no HXR emission at all. This behaviour is justified due to a combination of the dynamic range of *Yohkoh* 's Hard X-ray Telescope (HXT) which prevents further sources from being observed and the estimated energy release rates at the regions with HXR sources; much larger than in the kernels without HXR emission.

Aschwanden et al. (1999a) looked at 54 *Yohkoh* flares which were simultaneously observed with the *Compton Gamma Ray Observatory (CGRO)* and each of which had 2 footpoints. They reported there was no significant energy dependence of the HXR asymmetry, but found that it is inversely correlated to the trapping efficiency. By combining their observations with their asymmetric trap model they predict that the median value of the ratio between the field strengths at each footpoint would be 1.2. They did not, however, have magnetogram data to test their theory.

It was on the basis of both the Asai et al. (2002) result and the work of Aschwanden et al. (1999a) that further examples have been studied and are reported here. With contradictory examples cropping up throughout the literature it was important to look at a wider sample comparing them to modern space based magnetograms, where data is available 24 hours each day. A moderate sample of 32 flares were chosen where two HXR footpoints could be observed. It was then possible to determine the magnetic field strength

beneath them and compare it to the observed HXR intensity. It was important to establish a reliable and effective method of measuring footpoint field strengths and to be able to effectively compare these to HXR intensities. This method is described in detail throughout this chapter.

3.2 Flare Selection Criteria

A sample of 32 flares ranging from C-class to X-class was taken between 1996 (the beginning of science operations with *SoHO*) and the end of 2001 when *Yohkoh* met its demise. The events chosen were compact flares which consisted of two HXR sources as reported in the *Yohkoh* flare catalogue. In addition, the events had data in the L, M1 and M2 channels of HXT which showed the impulsive phase well above the background level. This allowed for spectral information to be determined along with the reconstruction of accurate images up to the M2 channel. These were used to give a footpoint location and intensity.

Further restrictions were required for data selection concerning magnetic field measurements. The sources were all situated either side of a magnetic neutral line and were within ~40^o of the disc centre. Within this ~40^o region there was assumed to be a radial field where the line of sight effects were minimised allowing simple corrections for disc position to be made. The limitations are discussed in Section 3.3. These measurements were combined with data from *Yohkoh*'s SXT and HXT.

3.3 Analysis Method

With a suitable sample of events it was possible to analyse the mean magnetic field strength beneath each flare footpoint. It was expected that a weaker HXR source would be discovered in the region of stronger magnetic field as the magnetic mirror inherent in a converging magnetic field should reverse the cascading electrons responsible for the thick-target bremsstrahlung emission.

Analysing a sample such as this, with the intention of making a direct comparison between different events, required that the magnetic field strength beneath the flare footpoints was determined in a systematic and reliable manner. There were many uncertainties involved and several steps were taken to minimise these.

3.3.1 HXR Image Reconstruction

Images were reconstructed from a set of the 64 spatially modulated photon counts accumulated to a minimum of 200 cts/s/sc in M2. This information was passed through a code based on that of Sakao (1994) which uses the Maximum Entropy Method (MEM) (Gull & Daniell 1978) to reconstruct the image. This method is fully explained in the instrumentation chapter.

3.3.2 Image Alignment

Image alignment was fundamental to the accuracy of this work; any unaccounted offset between images would give false results and make comparison unreliable. Consequently considerable effort was made to ensure the best possible alignment.

Each M2 HXR source was defined as a flare footpoint and MDI magnetograms were obtained from the daily data sets of 15 per day. These images have a cadence of 96 minutes and thus the closest image prior to any event was selected. They were differentially rotated to the time of the HXR emission and corrected for Earth-view. This was important as the *SoHO* spacecraft is situated at the L1 Lagrangian point whereas other observations were made from Earth orbit thus giving a different perspective. With these corrections the HXR intensity contours from the M2 channel were placed over the magnetograms in intervals of 10% of the peak intensity. Thus the mean single polarity magnetic field strength within each contour was obtained. The magnitudes of the field strength were added across the entire sample at each contour level and plotted to give Figure 3.1 showing any trend. It showed clearly that with increasing HXR intensity the mean magnetic field strength increased as fewer and fewer background pixels were included. The total mean magnetic

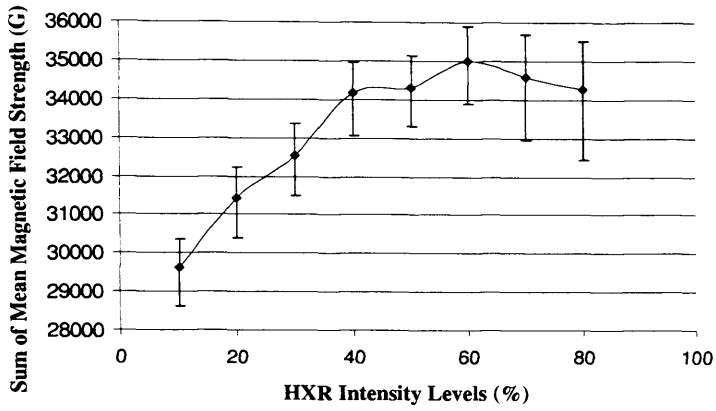

Figure 3.1: Each HXR contour level defines a region of magnetic field over which the mean magnetic field strength is determined. This plot is a representation of the magnitude of magnetic field variation with a percentage of the HXR intensity in a flare footpoint, as defined by *Yohkoh*'s HXT M2 channel MEM images. It is determined by the sum of the mean magnetic field strength at each level across the whole sample.

field strength peaked at the 60% intensity level. From this point onwards the number of pixels decreases sharply and as a result any offset between the two images became much more influential. Hence the 60% contour level was chosen as being representative of the mean magnetic field strength under the source.

Image alignment still, however, remained a significant source of uncertainty in the values determined. The pointing stability of *Yohkoh* was thought to be very good; of the order of $1''$ s^{-1} (Ogawara et al. 1991). Therefore, the discrepancy between this and the MDI magnetograms was assumed to be up to one MDI pixel, which approximately equates to $2''$ at the disc centre. As a result of this the HXR images in each case were shifted $2''$ in the direction of maximum difference. The mean magnetic field strength under each footpoint was then measured again and the difference between the two means was taken as the unavoidable uncertainty.

3.3.3 Other MDI Limitations

There were other issues which were important to be aware of when analysing MDI magnetograms. It was assumed that the magnetic field was radial at the photosphere. This is not a valid assumption in the chromosphere but it is reasonable at photospheric levels, and allows for corrections to be made to the line of sight measurements in relation to the disc position. As the active region moves away from the central meridian the line of sight measurement decreases with cos θ, where θ is the longitudinal position of the region measured from disc centre.

Additionally there were significant projection effects due to the line of sight measuring techniques. Due to this effect only events within 40^o of the disc centre were used. At the solar limb non-radial components of the magnetic field (i.e. the penumbra) may artificially enhance the values recorded by MDI. As it is impossible to compensate for this appropriate data selection techniques were employed to avoid the problem.

An additional issue was identified by the work of Hagenaar et al. (2003) which demonstrated the importance of accounting for MDI noise. They report a noise level of 3.2G and this has therefore been subtracted from all of the values used in this study.

Finally, it is beginning to emerge that MDI can dramatically underestimate the field strength measurements, particularly at high field values. Berger & Lites (2003) reported that values could be lower on average by a factor of 0.64 ± 0.013. However, this is based on a single set of observations and has not yet been verified for all observations. For this reason the values quoted throughout this work have not been corrected for this. However, it remains worthy of note.

3.3.4 Footpoint Field Strength Determination

The HXR intensities determined here were defined by the 20% contour. Although this was a physically larger region than that used for the magnetic field strength it was important to include most reliable counts. This represented an area where most of the relevant counts could be confidently attributed to the specific source (Sato et al. 1999). The 20% level

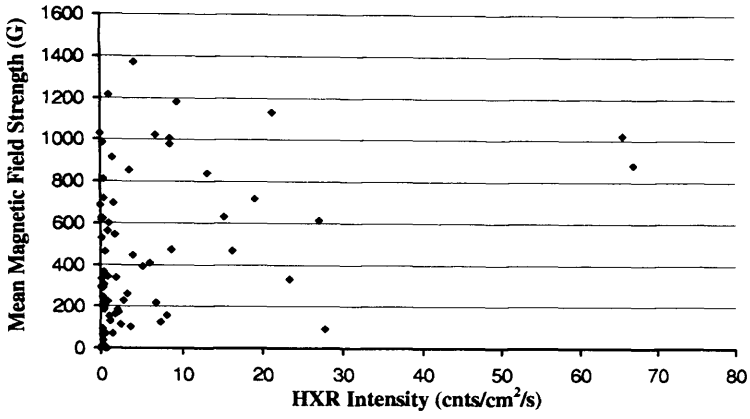

Figure 3.2: The HXR intensity at the 60% intensity level was determined and can be seen here plotted against the magnitude of the mean magnetic field strength beneath it. It is clear that there is wide variation in all values possibly an effect of comparing many different flare magnitudes.

was determined from the reciprocal of the dynamic range which has been empirically estimated to be between 10-20% (Kosugi et al. 1992). A smaller region could be used for the magnetic measurements as the positional information was most important and large regions of background field were not required.

3.4 Results

Using the above method of alignment the HXT intensity of each individual footpoint for each flare was determined along with their associated mean magnetic field strength. These two values are plotted against each other in Figure 3.2.

An inverse relation was expected based on the work of Sakao (1994). His data demonstrated that the stronger HXR emission originated from a weaker magnetic field strength region in four out of the five-featured cases, all from the M to X-class range. With the large scatter seen in Figure 3.2 any such relationship was not clear. This plot did, however, demonstrate the complexity of this study.

The sample reported here covered a range of flares from C through to X-class. In any given flare with two HXR sources, the absolute magnitude of the magnetic field beneath

each could be very different. However, if the plot in Figure 3.2 includes flares from only a single GOES classification there still remains significant scatter.

To limit the effect of the wide variation due to flare magnitudes, ratio values for the mean magnetic field strength and HXR intensity were used instead of the numerical values. The ratios were determined by comparing the two footpoints in a single flare. This provided a single value for direct comparison between events regardless of flare energy, provided both footpoints had a mean magnetic field strength well above zero. The result is shown in Figure 3.3. The stronger HXR source was always divided by the weakest, resulting in HXR ratios greater than unity. It was seen that about 50% (15) of events had both of their ratios greater than one, in the regime where the stronger HXR source was situated in the stronger magnetic field region. However, the remaining events fell in the region consistent with the results of Sakao's (1994) small sample, represented by the lower region of the plot. Here the stronger HXR source was located in a region of lower magnetic field strength. This was a consequence that would be expected as a result of simple magnetic convergence and mirroring.

It would appear from these findings that the magnetic mirroring hypothesis is not corroborated in this sample. Further analysis was thus performed in each of the two regimes to try and identify why this should be. There are those whose magnetic field ratio was less than one, where the flare follows the Sakao relation (Sakao, S-type events) and those greater than one, which did not (non-Sakao, N-type events). Due to the uncertainties inherent in the measurement technique it was reasonable to assume that those events where the error bars cross y=1 (the symmetry line) were likely to be almost symmetric in magnetic flux density. These were classified as an additional sub-group (balanced, B-type events) where measurement uncertainties play a significant role and thus these events could be removed from the study sample.

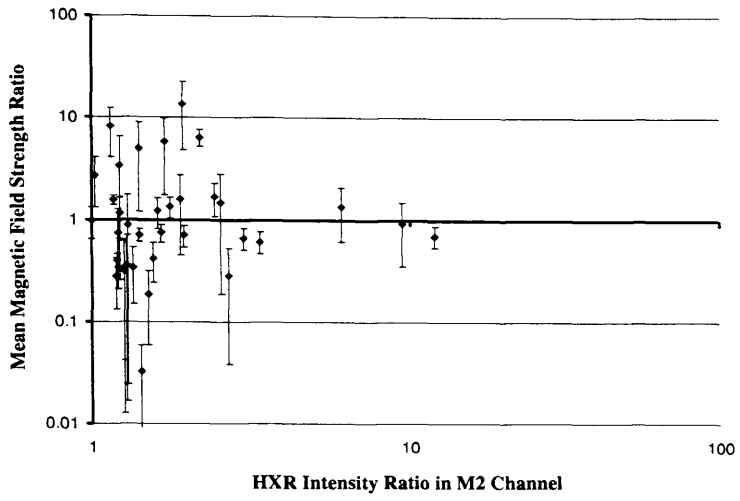

Figure 3.3: The HXR intensity ratio between the brightest and weakest footpoints in any given flare from the M2 channel are plotted directly against the mean unsigned magnetic field strength ratio between the same footpoints. The region below the y=1 line represents by the S-type events (those events where the stronger HXR footpoint lies in the region of weaker magnetic field) and the region above the N-type (where the stronger HXR lies in a region of stronger magnetic field).

3.4.1 SXR Loops

On closer inspection of contextual data additional complications were identified. Partial frame SXR images were available from *Yohkoh*'s SXT instrument. Appropriate filters were chosen such that saturation was minimised and that the shape of any structure could be seen clearly. When a single loop was observed the SXR light curves for a coincident region to the HXR footpoints could be compared. With a single SXR loop it would be reasonable to assume that the plasma at each end would show a similar response. Thus the shape of the light curves should be similar. When the profile differs substantially from one region to another it could be an indication that the regions were not connected in such a simple way and thus the possibility of different structures or magnetic connectivity should be considered. This would indicate the possibility that the electrons were not simply precipitating along a single loop and cannot be represented in this simple way. These cases are beyond the scope of this project which considered only simple single loop structures.

In five of the events from the full sample the SXR light curves showed significant differences. This could have been an indication the flare was the result of an interaction with a small loop, possibly emerging from beneath (as in Hanaoka's (1996) interacting loop studies) a larger loop. In these cases, one HXR source may be the unresolved footpoints of a small loop and thus these events were excluded from the study.

These five questionable events were broken down thus: two had error bars that cross the symmetry line (B-type) and three were from the N-type events reducing the group to just seven events. After the exclusion of these 5 problematic events there were 8 B-type events, 14 S-type and 7 N-type events.

3.4.2 HXR Timings

In 11 cases there were sufficient data to consider the timing of the HXR emission between the two sources. Of the 7 N-type events, with appropriate data, two were found with approximately simultaneous emission. This is limited by the cadence of the images, there could be tens of seconds between frames, and the Poisson noise. So at best it is only possible to quote simultaneity as within the image cadence. However, these are compact flares and it may not have been possible to measure the time difference over the limited distance.

In the S-type category seven events had sufficient data to observe individual light curves. Four of these had two individual light curves that peaked simultaneously, within the limits of the data (the time between images may be tens of seconds). In the other cases the footpoint with the strongest HXR source had a light curve that peaked first. This may suggest that the acceleration site of the electrons is positioned closer to the stronger footpoint. A greater distance to the weaker footpoint from the acceleration site could account for a longer flight time (Aschwanden et al. 1995). Alternatively it may suggest that the electrons precipitating towards the stronger footpoint are less impeded in their journey.

3.4.3 Magnetic Environment

In an attempt to understand the role of the magnetic environment in determining the properties of the HXR emission, the distribution of magnetic flux density under each of the flare footpoints was observed, the reasoning behind this being that the distribution may have been indicative of a particular event type. Where there was high convergence in the magnetic field, it was thought there would be a more rapid change or sharp peak in the flux density on crossing the footpoint, whereas for less magnetic field convergence the distribution would be flatter. However, there was nothing observed to distinguish between the two groups. In some cases the footpoints were only 3 or 4 MDI pixels across, which did not allow any distinction to be determined. However, the viewing angle provided an additional complication with this approach. Although the disc position is known, the direction of the magnetic field is unlikely to be exactly radial and thus the line of sight distortions would influence the observed strengths.

3.4.4 Spectral Evolution

Differences in the evolution of the spectral index can give insight into the trapping of electrons in a flare. It was hoped that these measurements would give a clue as to why the N-type events exist or how they differ from the S-type. Typically, spectral evolution in solar flares follows the soft-hard-soft pattern first recognised by Parks & Winckler (1969); a pattern evident across all of the above flare types.

It was important that there were data in at least the first three channels of HXT. Background was subtracted and a single power-law photon spectrum assumed. The spectral flux was assumed to be related to the photon energy by $E^{-\alpha}$ where α is the spectral index. In each flare the spectral evolution was observed and recorded at the hardest. The mean value for each group of events was ascertained along with the standard deviation in the spread. The S-type events were found to have a mean value of 3.4 with a deviation from the mean of 1.4, while the N-type had a value of 3.5 with a deviation of 1.2. Even the B-type events had a mean of 3.3 with a deviation of 0.7. Unfortunately there were not

enough data to study the evolution in each of the flare footpoints, which would have given more information. Therefore no quantitative difference was found which might indicate a difference in the transport or trapping of electrons in this limited dataset.

3.4.5 Examples

Some specific examples are presented here to illustrate the different categories along with the event properties: an S-type; an S-type where the HXR ratio is very high; a B-type; and an N-type event.

3.4.5.1 An S-type Event, 8th November 2001

This event occurred around 12:24 UT on the 8th November 2001 and the HXR light curves are shown in Figure 3.4a. The emission in each of the four HXT energy channels is plotted.

Figure 3.4b shows a soft X-ray image with superimposed HXR contours. These contours were constructed from the M2 channel around the time of peak emission within this channel. The region was very complex in soft X-rays although the situation became much clearer when compared to the magnetogram in Figure 3.4c. It was part of a large and ageing active region and thus multiple connections were probable. However, it was still apparent that the HXR sources formed at the footpoints of a smaller loop, which became brighter with time. When the spectral index was determined for this event, it evolved in the classic soft-hard-soft manner and had a value of 3.5 at the hardest.

When the footpoint brightness and mean magnetic field strengths were calculated it was clear that the brightest footpoint formed in the region with the weakest magnetic field strength, as was expected from the results of Sakao (1994). The ratio between the footpoint brightness was 3.0 and the ratio between the footpoint magnetic flux densities was $0.29^{+0.24}_{-0.18}$.

Further details of the remaining Sakao type events have been recorded Table. 3.1.

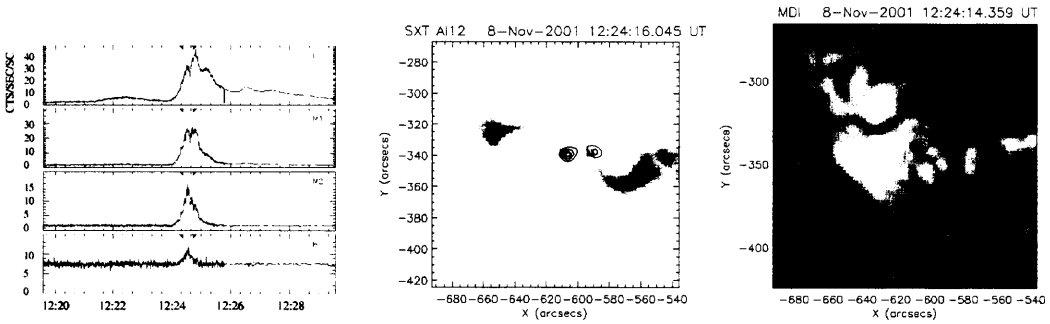

(a) (b) (c)

Figure 3.4: (a) HXT light curves for the flare on 8th November 2001 across each of the four energy channels. (b) The grey scale image represents a full resolution SXT image of the 8th November 2001 event at 12:24 UT in the Al12 filter. Superimposed are the HXR intensity contours 12:24:30 UT at 20%, 40%, 60% and 80% of peak intensity in M2 channel. (c) The greyscale image represents the magnetogram (where black is negative) from the 8th November 2001 event at 12:24 UT with the same HXR intensity levels as in (b) superimposed. It is clear that the footpoints are situated in regions of opposite polarity as expected.

Table 3.1: Featured properties of the S-type Events.

Date	Time (UT)	Goes Class	Position (arc seconds)	HXR Ratio	Magnetic Ratio
28-Jul-1999	08:31	M2.3	(-55.1,-331.7)	12.1	$0.7^{+0.16}_{-0.16}$
22-Dec-1999	10:54	C6.3	(-382.8,404.7)	1.3	$0.3^{+0.00}_{-0.19}$
06-Jul-2000	20:41	C3.7	(-258.2,254.2)	1.2	$0.4^{+0.05}_{-0.06}$
17-Jul-2000	20:25	M2.4	(-553.9,-279.1)	1.2	$0.3^{+0.10}_{-0.14}$
22-Nov-2000	16:20	C7.0	(-242.6,267.2)	1.3	$0.3^{+0.29}_{-0.11}$
24-Nov-2000	15:08	X2.3	(166.4,283.9)	1.9	$0.7^{+0.17}_{-0.13}$
24-Nov-2000	21:53	X1.8	(237.7,291.6)	1.6	$0.4^{+0.14}_{-0.18}$
06-Apr-2001	01:47	C7.7	(-607.1,-294.5)	1.6	$0.7^{+0.10}_{-0.14}$
12-Apr-2001	10:17	X2.0	(596.6,-274.2)	1.4	$0.7^{+0.10}_{-0.10}$
15-Jun-2001	10:27	M6.3	(-557.1,-430.5)	1.3	$0.3^{+0.30}_{-0.00}$
23-Oct-2001	02:16	M6.5	(-180.8,-389.5)	1.5	$0.2^{+0.01}_{-0.13}$
31-Oct-2001	08:05	M3.2	(24.1,138.4)	3.4	$0.6^{+0.04}_{-0.14}$
08-Nov-2001	12:25	M1.3	(-601.7,-359.8)	2.7	$0.3^{+0.24}_{-0.18}$
11-Nov-2001	10:57	M1.4	(-71.2,-335.9)	3.0	$0.7^{+0.15}_{-0.14}$

3.4.5.2 High Ratio S-Type Event, 28 July 1999

This event occurred around 08:30 UT on the 28th July 1999 UT and the HXR light curves are shown in Figure 3.5a. They illustrate the emission in each of the four HXT energy channels. The light curves in this case were more gradual and long-lived. Also the peak spectral index for this flare was 5.5, one of the softer events studied.

The SXT image shown in Figure 3.5b was again superimposed with the HXT contours from the M2 channel. The two HXR sources clearly coincided with the footpoint regions of a compact flaring loop. The eastern source was brighter in hard X-rays than the western source by a factor of twelve. This was unexpectedly high, but could be explained by the relatively weak nature of the western source. There are only five pixels in this source with intensity greater than 40% of the maximum intensity. We can be sure that the source is real however, as at the 20% level there are double this number of pixels.

The soft X-ray images allowed the analysis of the plasma at each end of a loop. Each region, which appeared coincident with the HXR emission, had a very similar light curve and made it likely that the two HXR sources are true conjugate footpoints. It was also possible with this event to take light curves of each of the HXR footpoints, and within the limits of the data shown in Figure 3.6, they appeared to be simultaneous. However, the reader must note the cadence, which makes it difficult to say with confidence that this is an entirely accurate indication of which footpoint peaks first as the peak could come some seconds later before the next data point.

The HXR image was superimposed onto a rotated and co-aligned magnetogram from MDI. It could be seen that the footpoints were either side of the magnetic neutral line. This is shown in Figure 3.5c. There was nothing in this event which clearly distinguished it from the other events in the category, other than the very high ratio between the HXR intensities.

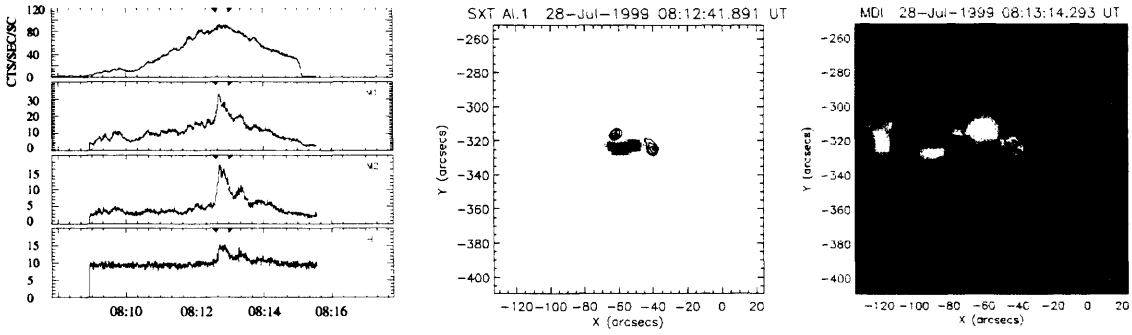

(a) (b) (c)

Figure 3.5: (a) HXT light curves for the flare on 28th July 1999 across each of the four energy channels. (b) The grey scale image represents the full resolution frame SXT image of the 28th July 1999 event at 08:12 UT in the Al.1 filter. Superimposed are the HXR intensity contours 08:12:45 UT at 20%, 40%, 60% and 80% of peak intensity in M2 channel. (c) The greyscale image represents the magnetogram (where black is negative) from the 28th July 1999 event at 08:13 UT with the same HXR intensity levels as in (b) superimposed. It is clear that the footpoints are situated in regions of opposite polarity as expected.

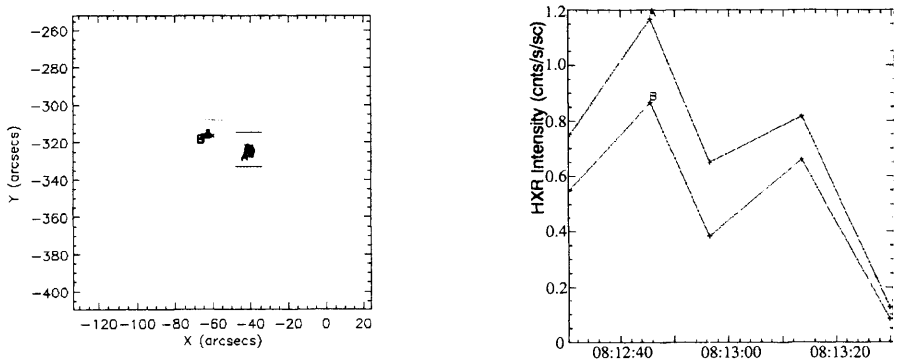

Figure 3.6: The M2 HXT image of the 28th July 1999 event at 08:12:45 is shown. Two boxes have been used to select the individual footpoints allowing us to observe the individual light curves seen at the right of this Figure The simultaneous nature of these light curves is clear.

3.4.5.3 B-type Event, 8th April 2000

This event occurred at around 02:38 UT on the 8th April 2000. The HXR light curves are shown in Figure 3.7a. They demonstrate a rapid increase in emission during the early phase of the flare but a more gradual decline in emission as time progresses. The peak spectral index for this flare was 3.1 which was very close to the mean value of 3.3 in this event class.

In Figure 3.7b the HXR contours from the M2 channel were placed over the SXR image. Again, it was clear that the two sources were situated at either end of a flaring loop. These same contours were also placed over the magnetogram in Figure 3.7c and each source was found to lay in a different magnetic polarity. In this case the magnetic ratio between the two footpoints was $0.9^{+0.86}_{-0.00}$, which would suggest that it was an S-type event, as discussed above. However, the uncertainties described previously, when applied to this event, were highly influential and gave rise to the possibility of the ratio being greater than unity. This would suggest that classification is impossible within the errors. There have been no other properties found that distinguish this event, but the limitations imposed on the measurement of the magnetic field strength make a more precise result impossible. It may simply be that this, along with the other events in this category, are symmetric in their footpoint field strengths or the geometry of these events is such that the line of sight measurement limitations are more influential. It was not possible to reliably classify these events into either N of S-type categories. Table 3.2 shows a list of all flares in the B-type group identified through this study.

3.4.5.4 N-type Event, 16th March 2000

This event occurred on 16th March 2000 at around 18:35 UT. From Figure 3.8a it is shown that there were two peaks in the M1 and M2 channels. The L channel was more gradual, as expected, but still had two bumps coincident with the peaks in the higher channel. Unfortunately there was only data up to this second peak and it was impossible to analyse this event beyond that point. It was, however, still clear that the flare had only two HXR

sources. It should be noted that this double peak is not a characteristic of all N-type events, but simply a feature of this one. The two sources are shown in Figure 3.8b along with the relation to the soft X-ray emission. Again these two sources were situated at each end of a flaring loop although the loop is longer than that of the high ratio S-type event. There also appeared to be an extra component to this loop near the northern footpoint in a region of single magnetic polarity, although all of the SXR regions had a similar light curve. In addition the peak spectral index for this event was 4.1, a little softer than the mean value.

Figure 3.8c shows the relation between the HXR and magnetogram. The brightest source was situated in the north and was in the region of strongest magnetic field. However, there were too few data points to establish whether any time delay existed between the two HXR emission profiles.

Other than the strong source being in a region of strong magnetic field this flare behaved much the same as the others. However, the northern soft X-ray region was brighter than the southern and may be an indication that the acceleration site of the electrons responsible for this event may be closer to the north end. If that was the case, then it could be possible that the flaring electrons are able to penetrate deeper into the stronger region before being mirrored, as there was less actual field convergence over a smaller section of loop. In addition the increased flight time to the other footpoint may mean a reduction in the number of electrons impacting the chromosphere in a focused region causing high amounts of radiation. Table 3.3 lists the properties of all of the non-Sakao type events.

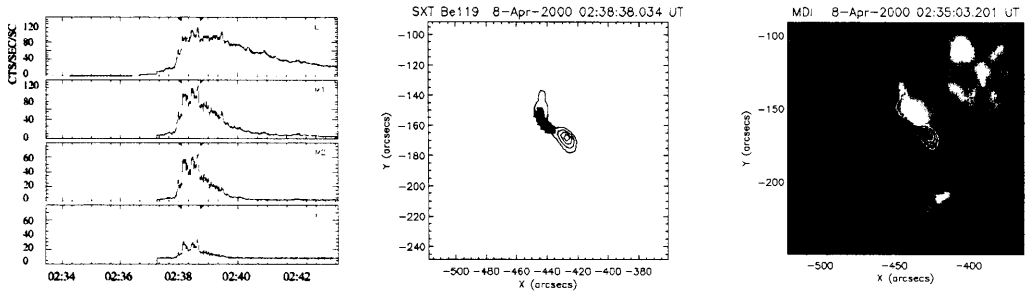

(a) (b) (c)

Figure 3.7: (a) HXT light curves for the flare on 8th April 2000 across each of the four energy channels. (b) The grey scale image represents the full resolution frame SXT image of the 8th April 2000 event at 02:38 UT in the Be119 filter. Superimposed are the HXR intensity contours 02:38:32 UT at 20%, 40%, 60% and 80% of peak intensity in M2 channel. (c) The greyscale image represents the magnetogram (where black is negative) from the 8th April 2000 event at 02:35 UT with the same HXR intensity levels as in (b) superimposed. It is clear that the footpoints are situated in regions of opposite polarity as expected.

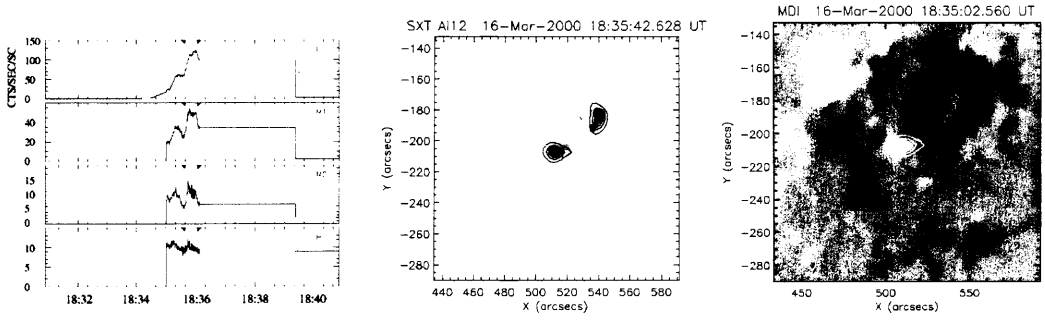

(a) (b) (c)

Figure 3.8: (a) HXT light curves for the flare on 16th March 2000 across each of the four energy channels. (b) The grey scale image represents the full resolution frame SXT image of the 16th March 2000 event at 18:35 UT in the Al12 filter. Superimposed are the HXR intensity contours 18:35:45 UT at 20%, 40%, 60% and 80% of peak intensity in M2 channel. (c) The greyscale image represents the magnetogram (where black is negative) from the 16th March 2000 event at 18:35 UT with the same HXR intensity levels as in (b) superimposed. It is clear that the footpoints are situated in regions of opposite polarity as expected.

Table 3.2: Featured properties of the B-type Events.

† These events are thought to be complicated by the interaction of multiple SXR loops and thus contributions from unresolved HXR footpoints can not be ruled out.

‡ This is the event studied by Asai et al. (2002) and the table lists magnetic footpoint ratios consistent with her observations.

Date	Time (UT)	Goes Class	Position (arc seconds)	HXR Ratio	Magnetic Ratio
30-Jun-1999†	11:26	M1.9	(108.8,-294.7)	1.6	$1.2^{+0.40}_{-0.01}$
25-Aug-1999†	01:35	M3.6	(-183.5,-550.7)	1.2	$0.7^{+0.35}_{-0.52}$
08-Apr-2000	02:38	M2.0	(-440.8,-172.2)	1.3	$0.9^{+0.86}_{-0.00}$
08-Apr-2000	20:44	M1.8	(-292.3,-155.1)	1.2	$1.1^{+0.00}_{-0.50}$
25-Nov-2000	18:38	X1.9	(383.9,292.9)	6.1	$1.3^{+0.72}_{-0.20}$
10-Apr-2001‡	05:19	X2.3	(125.7,-282.9)	1.0	$0.9^{+0.27}_{-0.33}$
14-Sep-2001	01:35	M3.7	(-580.2,-320.7)	1.9	$1.6^{+1.13}_{-0.62}$
17-Sep-2001	08:21	M1.5	(-86.9,-342.6)	2.5	$1.5^{+1.29}_{-0.58}$

Table 3.3: Featured properties of the N-type Events.

† These events are thought to be complicated by the interaction of multiple SXR loops and thus contributions from unresolved HXR footpoints can not be ruled out.

Date	Time (UT)	Goes Class	Position (arc seconds)	HXR Ratio	Magnetic Ratio
18-Jan-2000†	22:06	C4.3	(-255.6,356.1)	1.1	$8.2^{+4.75}_{-4.17}$
02-Mar-2000†	08:24	X1.1	(749.9,-226.6)	1.2	$1.6^{+0.00}_{-0.16}$
15-Mar-2000	05:41	C4.0	(227.7,-176.7)	1.9	$13.6^{+8.77}_{-8.78}$
16-Mar-2000	18:36	C9.0	(512.9,-211.7)	1.0	$2.7^{+1.36}_{-1.61}$
25-Jul-2000	02:48	M8.0	(125.1,-15.1)	1.8	$1.3^{+0.30}_{-0.17}$
25-Sep-2000†	02:09	M1.8	(257.6,55.9)	1.8	$1.3^{+0.64}_{-1.18}$
06-Apr-2001	19:16	X5.6	(-493.8,-262.9)	2.4	$1.7^{+0.60}_{-0.34}$
24-Apr-2001	06:58	M3.1	(-223.6,382.9)	1.4	$5.0^{+3.85}_{-3.68}$
31-Aug-2001	10:38	M1.6	(-553.3,147.2)	1.2	$3.4^{+2.88}_{-3.11}$
10-Sep-2001	05:13	C8.7	(-214.2,-503.1)	1.7	$5.8^{+2.44}_{-4.03}$

3.5 Discussion

This study has demonstrated that the relation between the magnetic flux density at the footpoints of a flaring loop and HXR emission is much more complicated than previously suggested by Sakao. The relationship may not even be a direct one.

When one compared the actual intensity of any individual footpoint to the magnetic flux density beneath it across a large sample, assuming the same magnetic apex, it was clear the magnetic mirroring effect was not the defining process responsible for the emission level.

It is important to note that magnetic connectivity can be complex and although SXR images show single loops in most cases, they only show structures containing hot plasma and give little information about any fine structure or the environment in which the flare occurs. The latter is especially important, as it is the magnetic field convergence which is responsible for the mirroring of electrons and not the strength of the field alone. Therefore a more detailed study of the magnetic field surrounding the footpoints may give rise to a clearer understanding of these mirror points. If one studies the field around the footpoint, it may be possible to determine how much the field can expand giving a better understanding of the level of convergence.

Also the flare sample spanned all classes and thus HXR and mean magnetic field strength ratios between the two footpoints in each event were calculated. This focused the problem by removing the issues associated with flare magnitude. It was from this study that two main groups of flares were defined; the Sakao type (S-type) and the non-Sakao type (N-type):- S-type events have high HXR intensities relating to low mean magnetic field strengths, and N-type events had low HXR with low magnetic field strength.

The uncertainties involved required the definition of a third class of event necessary which have been classified as B-type events. These events were those whose error bars cross the dividing line between the other two classes above and thus were likely to have a more symmetric nature or be dominated by measurement uncertainty.

From this sample of 32 events about 40% were the traditional Sakao type, 25% were

approximately symmetrical in mean magnetic field strength and about 30% were the non-Sakao type.

It was hypothesised that S-type events are the result of converging magnetic field lines in strong regions, which act to mirror precipitating electrons and thus reduce the number available to form HXR through thick-target bremsstrahlung. Conversely with less convergence in weaker field regions, more electrons can precipitate to the chromosphere and give rise to a stronger HXR footpoint. These results would suggest that this is not the case otherwise why should we observe N-type events?

It was hoped that many of these events would have enough counts so that individual HXR light curves could be seen for each footpoint. This information could allow any time lags between emissions to be observed. If the hypothesis was true for some cases the N-type may be simply due to an asymmetry in the location of the acceleration site. If the acceleration site were located closer to the brighter footpoint it may reduce the effects of convergence over the shorter distance, allowing more precipitation in this region than if the acceleration site was located at the loop apex. With further observations it may be possible confirm this, although currently it is not possible to rule out some other process that impedes the electron precipitation at the weaker footpoint.

To go one further, one should ask whether field convergence would be expected in the chromosphere in a significant enough way as to cause this mirroring? The relation of the magnetic pressure (P_B) and the gas pressure (P_{gas}) was considered through discussion with J. C. Brown thus:

$$\frac{P_B}{P_{gas}} \sim \frac{B^2}{8\pi nkT} \simeq \frac{2B_2^2}{n_{14}T_4} \tag{3.1}$$

where B is the magnetic field strength ($B_2 = B/10^2$), n is the volume density ($n_{14} = n/10^{14}$) and T is the temperature ($T_4 = T/10^4$). From this it is seen that n is required to be greater than $10^{14} cm^{-3}$ which is a typical lower chromospheric density. This is possibly why loops often look uniform in SXR images. Additionally knowing that the scale height (H) in the chromosphere is approximately 300km and also that $N = nH$ (N is the column density), it is determined that $N = 3 \times 10^{21} cm^{-21}$.

From Brown (1972) the depth N_s required to stop precipitating electrons of 100KeV is found to be:

$$N_s = \frac{E^2}{2K} \simeq 2.5 \times 10^{21} cm^{-2} E_{100}^2 \tag{3.2}$$

Where E is the electron energy ($E_{100} = E/10^{100}$) and K is a constant ($55.7\pi e^4$). Here one can see that the depths required for magnetic convergence can only be reached by electrons greater than 100KeV. So using these approximate calculations it is shown that convergence is likely to be too low for mirroring to be important in the flares studied.

The B-type events determined earlier enabled us to remove events that had the most influential uncertainties. Although these events were more or less symmetric in magnetic field strength at the footpoints, the same could not be said for the HXR intensities. As a result, the B-type events could not reliably be placed in S- or N-Type categories.

The work of Aschwanden et al. (1999a) showed an asymmetric trap model. In this work it was assumed that the acceleration site for the electrons was equidistant from each of the flare footpoints and was thus at the loop apex. On this basis it was predicted that the median value for the ratio of the magnetic fields at the footpoints would be 1.2. We found in the case of the B-type events this is true, although the S-type have a median value of 0.4 and the N-type a value of 3.4. Therefore, using the method of observation presented here, it was not possible to confirm their predictions, although it is unknown how moving the acceleration site would affect them.

3.6 Conclusions

The sample of 32 flare events has shown that it is not necessarily true that the stronger HXR footpoint is situated in the weaker magnetic field region. The weaker footpoint would appear to have a likelihood of 2:1 to be situated in a region of stronger magnetic field. Although the results of Sakao's thesis show a 4:1 relation, only 5 events were considered and the single observation that showed a N-type result was limited by the

frequency of the ground based magnetograms. The results here show that these N-type events occur more frequently than previously thought.

There is little that distinguishes the groups of events and there is no quantitative difference between the peak spectral hardness across the groups, nor is there any real difference in the distribution and magnitudes of the HXR and magnetic ratios.

It is also possible to state, that based on the simple calculations in the discussion, it is unlikely that electrons would reach a depth where there is significant magnetic field convergence. They are more likely to be stopped before this in the lower chromosphere.

Chapter 4

A Slow Coronal Mass Ejection with Rising X-Ray Source

4.1 Introduction

The relationship between flares and CMEs has been debated for some time, although it is becoming apparent that they may arise from the same magnetic phenomenon. Several driving mechanisms have been proposed, reviews of which can be found in, for example, Klimchuk et al. (2000), Forbes (2000) and Forbes (2003). They fall into two main categories: storage and release; and directly driven scenarios. The most common category, but not universally accepted, is the storage and release scenario. Here a slow build-up of magnetic stress precedes the onset of some kind of instability. The CME starts with the rise of an active region filament (and its overlaying arcade) due to an eruptive instability. Then, below the rising filament, as the stretched field lines start to reconnect, an impulsive energy release occurs and is accompanied by the acceleration of the filament eruption. In the main flare phase continuing reconnection forms Hα ribbons at the loop footpoints, where the particles accelerated during the reconnection process impact the chromosphere, followed by hot X-ray loops. As field lines increasingly distant from the

[1]This work has been published in A& A by Goff et al. (2005)

magnetic inversion line reconnect, the reconnection region rises. Therefore the resulting X-ray loop footpoints and the Hα ribbons appear to move apart. The initial instability may be triggered by (i) a twisted flux tube, where the twist or height of the filament reaches a supercritical value; or (ii) a sheared magnetic arcade, in which the magnetic energy is built up by shearing motions until a critical value is reached.

Most CME studies are based on coronagraph data, which are limited to observations above a certain altitude. By the time the CME has reached the point of detection, it has normally finished accelerating and continues at a constant velocity (St. Cyr 1997). Regardless of the mechanism, the plasma and associated magnetic field are accelerated from the low atmosphere at velocities that can reach in excess of 1000 km s^{-1}. The event presented here is significantly slower and therefore observations of the acceleration profile of the CME, before it reaches the coronagraph field of view, can provide valuable insights into the underlying process.

It is sometimes possible to detect a rising flux rope or filament in the low corona with *TRACE* observations. An example of this can be seen in Gallagher et al. (2003). They demonstrate that an exponential increase in height is observed when height–time information from the low corona is combined with the more traditional CME measurements in LASCO data. Typically height-time measurements from LASCO can be fitted linearly, demonstrating that the CME has reached a steady velocity. The example observed by Gallagher et al. (2003) is one of the very few observations of the acceleration phase.

Through a combination of observations from *TRACE* along with an additional data point from the Ultraviolet Coronagraph Spectrometer (UVCS; Kohl et al. 1995), this 21st April 2002 event was reported to have a low initial velocity. For its initial height-time behaviour to connect smoothly with the coronagraph observations, an exponential increase in acceleration was required.

Typically below a lifting flux rope/CME there is a complex array of rapid loop and footpoint brightenings, plasma jets and other types of ejecta (e.g. Shibata et al. 1995). A moving high-temperature (15MK) source has been reported by Tsuneta (1997) in a 2nd December 1991 limb flare. This plasmoid formed during the impulsive phase, above

the X-point and rose with a velocity of ~96 km s^{-1}. It is understood that the X-point represents the presumed magnetic reconnection region and below this are V-shaped high temperature ridges representing the newly reconnected loops. A hard X-ray (HXR) source is located at the top of these soft X-ray (SXR) loops; caused by the fast shock acting on the newly reconnected loops. Due to the symmetrical nature of the reconnection, outflows must occur both upward as well as downward and it is believed that the upward flows are responsible for the plasmoid.

The event we present was part of a homologous series first analysed by Veronig & Brown (2004) and Sui et al. (2004). They found that three homologous flares occurred between 14th April and 16th April 2002. This paper concentrates on the 16th April event. Sui et al. (2004) focused on the *RHESSI* (Lin et al. 2002) data and identified an associated CME in the LASCO catalogue for their April 15th event. It will be demonstrated that there was also an associated CME with the 16th April event. An extensive array of data was analysed and was used throughout to investigate the acceleration of the CME, as well as the coronal hard X-ray source.

4.2 16th April 2002 Event

The flare on 16th April 2002 occurred at ~12:52 UT in the northwest quadrant of the Sun (NOAA Active Region 9901). From the (GOES) soft X-ray light curve (Figure 4.1) it can be seen that the M2.5 flare lasted for three hours and had the characteristics of long duration events (LDEs) which are generally related to filament eruptions.

4.2.1 Observations of a Rising Filament

The event was observed in the *TRACE* 195 Å band for the entire duration of the flare (Figure 4.2) with a 17 second cadence and an image scale of 0.5″ per pixel. Standard image corrections were first applied (as discussed in section 2.5.2.1) before the pointing offsets were corrected. Image offset was addressed by cross-correlating these *TRACE*

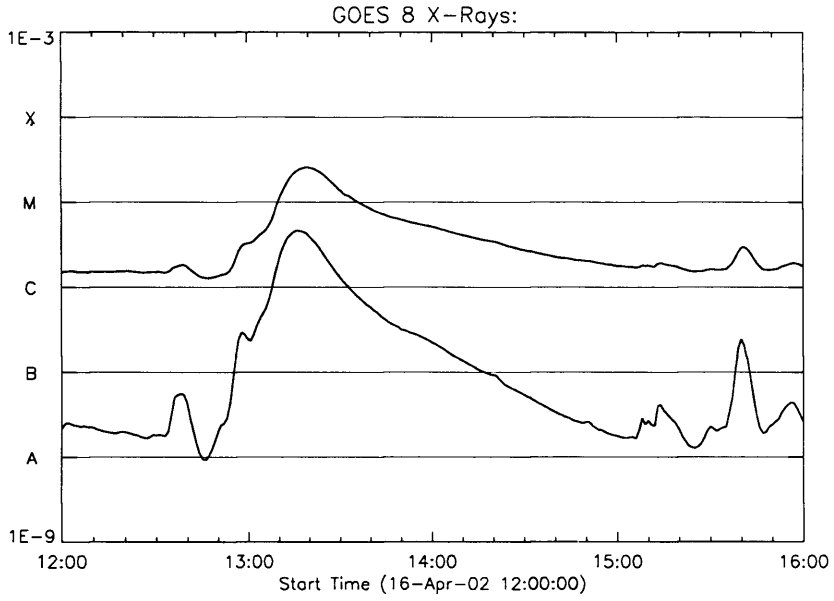

Figure 4.1: The GOES light curve for the 16th April 2002. The event studied in this chapter occurred at around 12:50 UT

images with EIT images where the pointing was well known. A full description of this method can be found in Gallagher et al. (2003), but a brief description can be seen in section 2.5.2.1.

The *TRACE* images show loops (Figure 4.2) which represent the end of an arcade like those observed in the previous two events. At approximately 12:55 UT, the end of this arcade began to brighten as the loops filled with hot plasma, as a result of chromospheric evaporation. These loops appeared to grow in height as the reconnection continued, and a cusp feature formed at around 13:10 UT. When the region above the bright loops was examined more closely it was possible to see a fainter structure, presumably heated filamentary material, which began rising at about 12:54 UT. This was seen clearly for ~20 minutes and was tracked. I will show later, in section 4.2.4 that spectra taken by CDS of this rising filament material indicate the presence of helical flows, providing evidence of its helical flux rope nature.

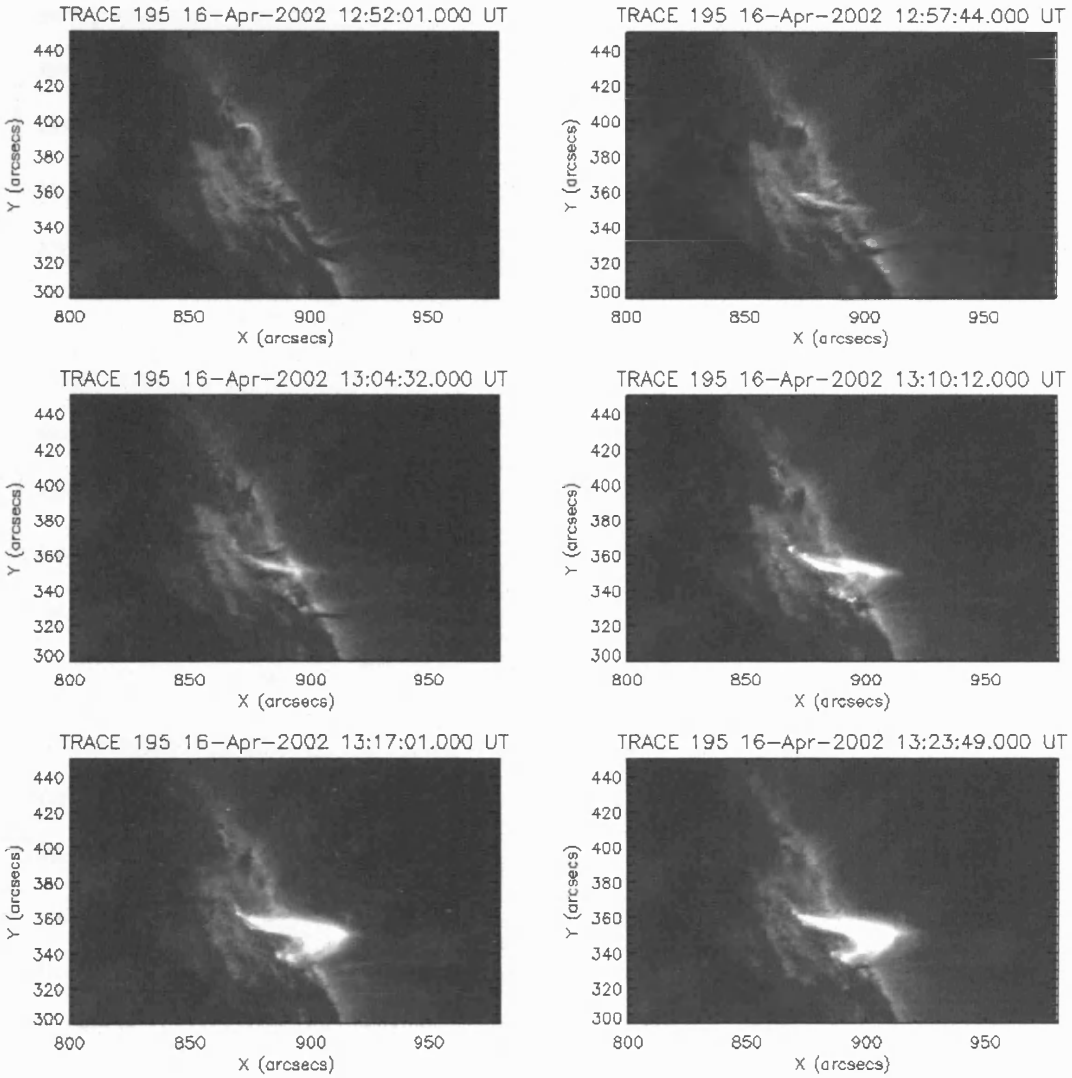

Figure 4.2: A time series of *TRACE* 195 Å images. These clearly show the formation of the flaring arcade with the formation of a cusp towards the end.

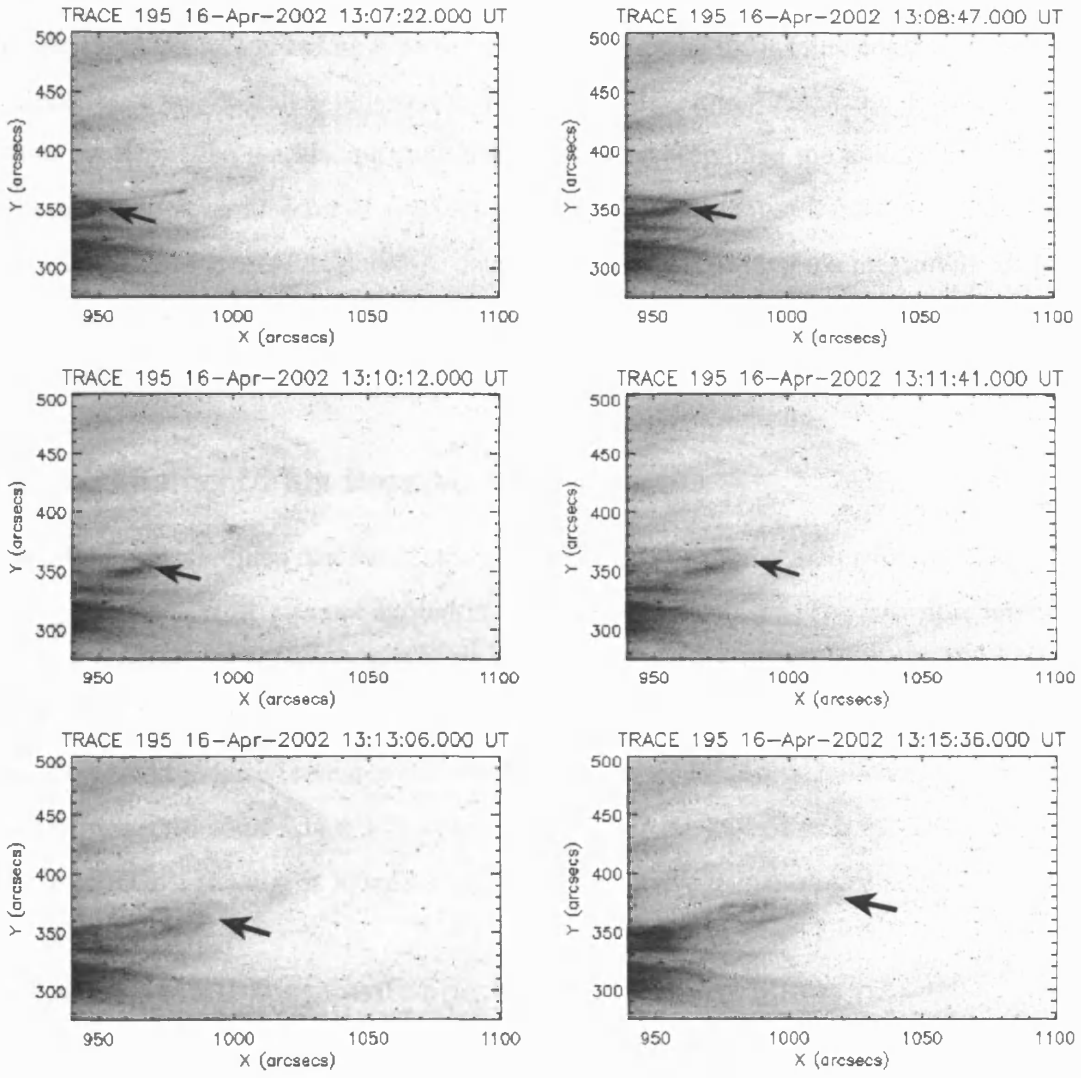

Figure 4.3: *TRACE* 195 Å images, with a reverse colour table. The field of view has been reduced to give a much clearer view of the lifting flux rope. The images are a time series from top left to bottom right. The lifting flux rope is seen as the dark feature expanding towards the right.

4.2.2 Tracking the Filament

Figure 4.3 shows the rising flux rope as observed by *TRACE* . It is likely that the contained plasma was heated which would allow the material to be seen as emitting for a short time in the 195 Å pass band before it cooled again. By tracking the leading edge, using visual inspection, a height-time profile was extracted from the *TRACE* data cube. In each image from the data cube the leading edge position was recorded and the altitude calculated. There was however an error of up to ±5 pixels, due to human uncertainty, which equated to 2.5″ in the case of *TRACE* 195 Å data. However, by repeating the measurements five times and taking a mean value, any larger errors were reduced. The resulting height-time plot is shown in the top panel of Figure 4.4.

4.2.3 Filament/Flux Rope Velocity

Initially it was assumed that the height-time plot could be represented with two linear fits as a simple linear fit was not appropriate for the whole dataset. The first nine minutes were linearly fit with an acceptable R^2 statistic of 0.89 giving a constant velocity of ~ 45 km s^{-1} from the gradient. This was followed by a short data gap, after which the flux rope appeared to have increased its velocity. This second linear fit indicated the velocity had increased to some 75 km s^{-1}, where the fit had an R^2 statistic of 0.99. There was not however, any indication as to what could have caused this increase in velocity.

4.2.4 Coronal Diagnostic Spectrometer Observations

The Coronal Diagnostic Spectrometer (CDS) also observed this event and the slit was positioned above the limb at x=945″ and centred at y=400″ (Figure 4.5). The instrument was in a 'sit and stare' mode using the 2x240″ slit while observing in Fe XIX. A simple stack plot of intensity slices against time is presented in Figure 4.5. It shows clearly that just after 13:00 UT there was a rising loop or filament, which was viewed by the slit and is represented by a crescent shape in this Figure. This crescent was a mirror image of the rising loop as the tip passed through the slit first followed by the legs. The timing was

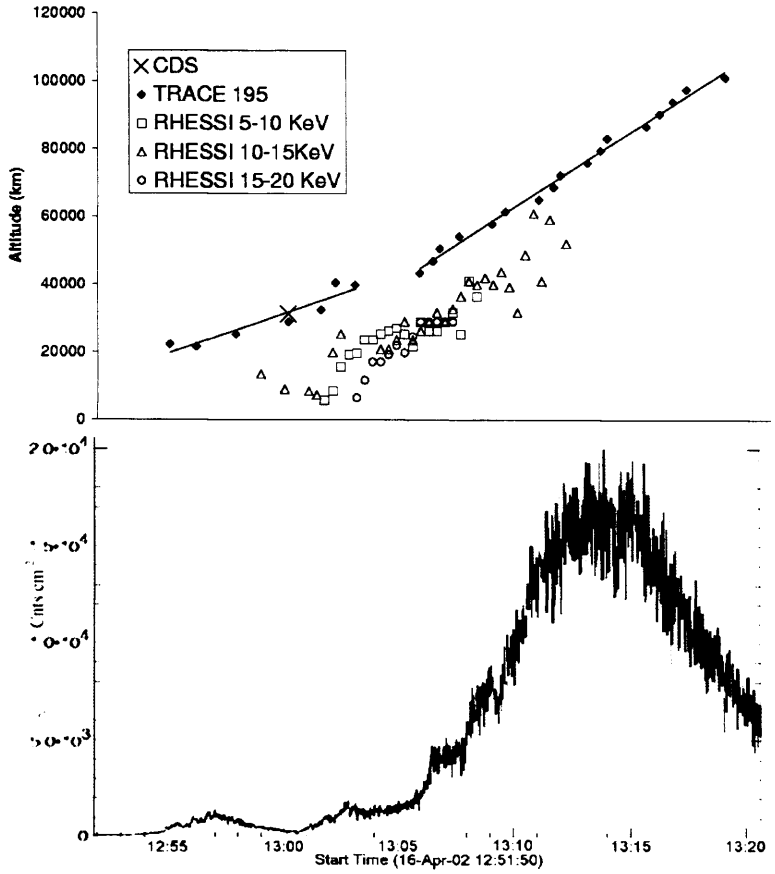

Figure 4.4: Top: Height-time plot for the lifting filament/flux rope as seen by *TRACE* . The cross represents the leading edge of the rising structure as seen by CDS. Below the best-fit lines are the data points from the coronal hard X-ray source. Bottom: The hard X-ray light curve including all data between 5 and 50 keV over the same time frame as the height-time plot above.

consistent with that expected from observations in the low corona and is shown as a cross in Figure 4.4.

By studying the Doppler velocities of this feature it was apparent that the bottom left section of the data, which represented the leading edge, had a blue shift whereas the rest of the loop structure was red shifted. This was suggestive of helical flows such as those described by Pike & Mason (2002). Anti-parallel flows along threads forming the filament body may result in a similar picture. However, erupting filaments are frequently observed to show helical whirling motions. Therefore the organised pattern of blue-shift followed by red-shift combined with this information suggests helical flows and was representative

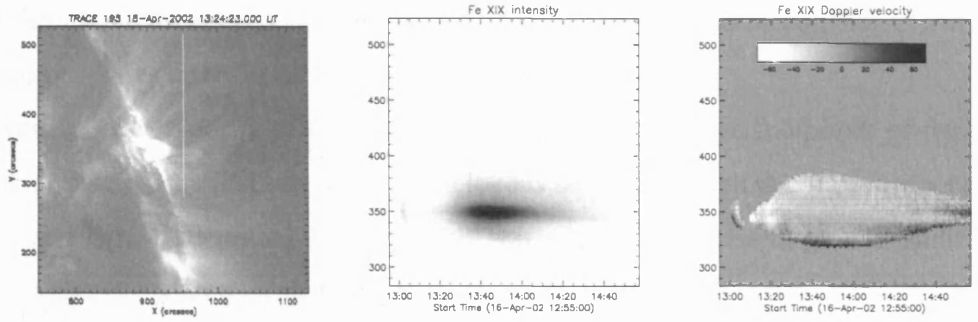

Figure 4.5: Left: *TRACE* 195 Å image with a line illustrating the position of the CDS slit. Centre: CDS time series of slit intensity images. CDS was in a 'sit and stare' mode and this image shows what happened beneath the slit over the time of event. The crescent shape to the left of this image represents the lifting flux rope. Right: Here is shown the Dopplergram of the same data. The colour bar indicates the Doppler velocity where white is blue-shifted and black is red-shifted. These two images were compiled and calibrated by L. K. Harra.

of a flux rope structure for this erupting filament.

4.2.5 *RHESSI* observations of a rising coronal source

RHESSI observations provided an additional dataset for this event. Light curves for the flare in the 3-6, 6-12, 12-25 and 25-50 keV energy channels were constructed; above 50 keV there was almost no emission. A peak was observed around 12:57 UT in the 3-6, 6-12 and the 12-25 keV channels. A much higher intensity, smooth light curve beginning at 13:00 UT and peaking around 13:13 UT was observed in the 25-50 keV band.

From this dataset is was possible to use the PIXON method (Metcalf et al. 1996) to reconstruct images; a sample is shown in Figure 4.6. A description of the principle can be found in section 2.2.1.

The images shown were constructed over 5 rotation periods (approximately 20 seconds) in 5 keV bins. Grids 3-9 were used in the processing giving an angular resolution of $\sim 7''$. There was general agreement with the configuration illustrated in both Veronig & Brown (2004) for the event on the 15th April 2002 and Sui et al. (2004) discussed earlier in section 4.1. The most intense emission in that event came from along the loop top,

which Veronig & Brown (2004) described as a loop so dense as to be collisionally thick at electron energies up to 50 keV in their earlier event.

In general, the majority of the emission is located at the dense footpoints of flaring loops. However, in the first two of the homologous series, of which this flare was a part, Veronig and Brown identified the loop itself was acting as a dense target. In addition there was another source located above the loop top source (a coronal source); also observed by Sui et al. (2004) in the 16th April event. This was clearly identified in images reconstructed with the PIXON method in the 5-10, 10-15 and 15-20 keV bands.

The dynamic range of *RHESSI* images is considered to be 10:1, thus all measurements were limited to regions where the brightness was more than one tenth of the peak image brightness at any given time. Although this source was observed by Sui et al. (2004), they reported the source as stationary. We note, however, that they imaged over a shorter time interval and wider energy bins.

Motion was clearly seen in the height-time plot shown in Figure 4.7 with the method described here. This source was weak relative to the bright emission from the loop top and often appeared to break up into fragments. However, their mean positions remained consistent with an outward moving source. Where the images were broken the brightest point from the sources was used to determine the source position and added to the plot.

The velocity of this source could be determined from the gradient of the height-time plot shown in Figure 4.7. It was clear the velocity of this source, at $\sim 60\pm20$ km s^{-1}, was comparable to that of the flux rope at the same point in time. The velocity of the flux rope, from the linear fitting performed earlier, was between 45 and 75 km s^{-1}. This was suggestive of an intimate link between the two phenomena.

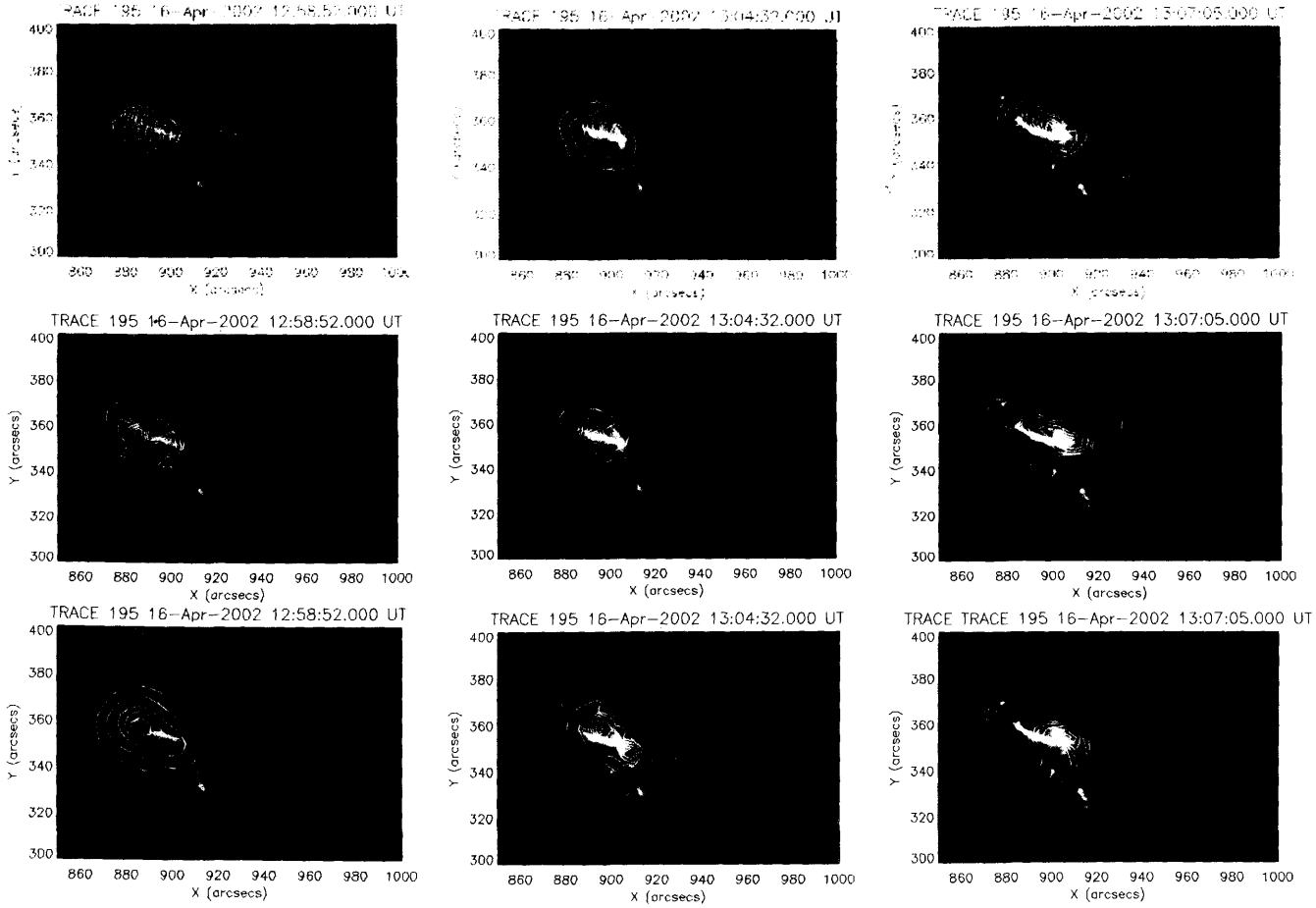

Figure 4.6: The images in this figure are all *TRACE* 195 Å images. On these images are *RHESSI* contours at 80%, 60%, 40%, 20% and 10% of the peak intensity. The top row shows contours from the 5-10 keV, the second row shows 10-15 keV and the final row has 15-20 keV contours. Of particular note is the coronal source. One can see that this source moves with time from left to right, i.e. upward.

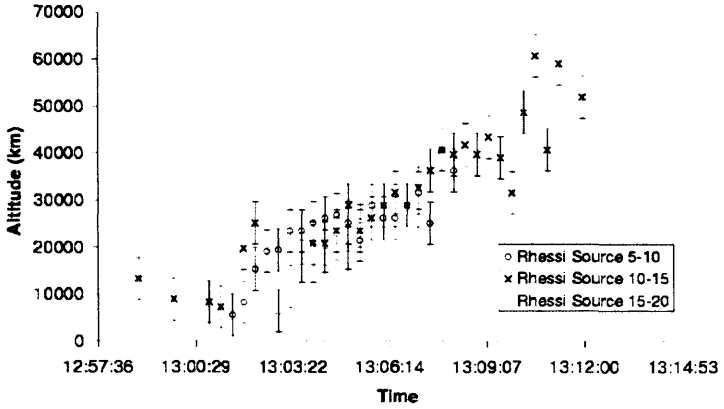

Figure 4.7: This height-time plot is derived from the coronal HXR source over three separate energy bands.

Figure 4.8 shows the light curves for the coronal source in the 10-15 keV band and also for the entire loop in the same energy range (Figure 4.8). The coronal source appeared weak from these light curves. The light curve for the coronal source was compiled by taking a large box around the source and summing the pixels within. To avoid contamination from the loop-top source a box was used to sample the area which was moved higher with the source evolution, keeping the source in the box centre. One can see immediately that the maximum intensity in the coronal source was significantly below that of the peak in the loop top and footpoint light curve. The emission was gradual and not very impulsive in both the loop top/footpoint source and the coronal source, although the coronal source light curve was much noisier.

This moving coronal source also passed through the CDS position, which had previously observed the rising flux rope. However, at the time of the coronal source passage there was little, if any, emission seen by CDS probably as a result of the source being at a higher temperature than the peak formation temperature for Fe XIX and the emission measure there being low.

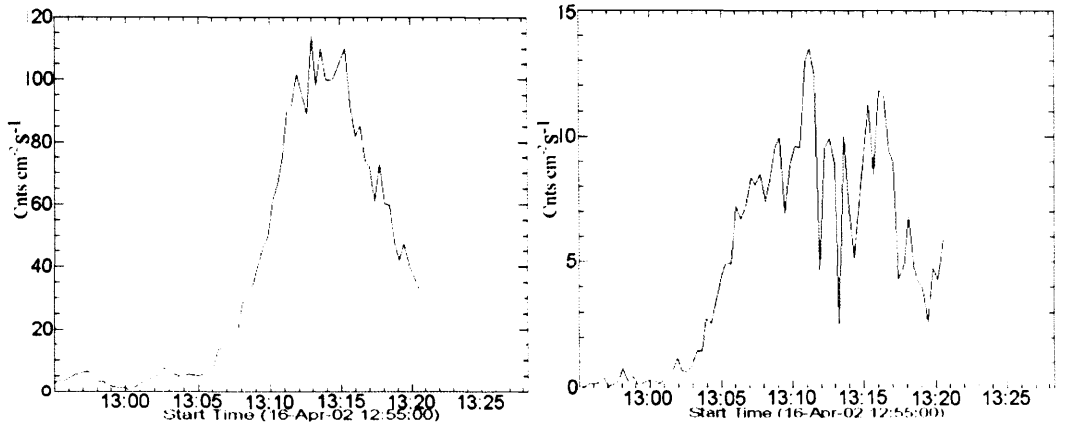

Figure 4.8: The left light curve is constructed to show how the number of counts changes with time for the loop top source and the loop footpoints. They have been grouped together as it is very difficult to distinguish between them accurately. The right light curve is that of the coronal X-ray source located above loop top source.

4.2.6 Cooling down-flows

Also apparent in the CDS observations shown in Figure 4.5, it was seen that the helical structure in the rising flux rope was followed by a gap, then by a bright source which appeared at ~13:14 UT. Only data above a reliable threshold of 10% is shown. The source expanded in size to a maximum of ~65″ at around 13:35 UT and then gradually decreased. This was consistent with the results seen in a separate dataset formed from *TRACE* .

The *TRACE* image cube was taken and a synthetic slit at the same position as that of CDS was constructed. From this, a stack plot was produced, consisting of slices of the image over a time range. This represented the *TRACE* equivalent of a CDS image, and is shown in Figure 4.9. It demonstrated that the lifting flux rope crossed the slit position, as in the CDS image, with one difference; the emission was from much cooler plasma. The legs of this flux rope could also be seen and they extended further than in the CDS image. There was weak emission under the flux rope but at around 13:14 UT the image becomes bright again. This compared well to the emission in CDS. It is believed that the *TRACE* emission was largely due to the newly reconnected loops getting higher with time and

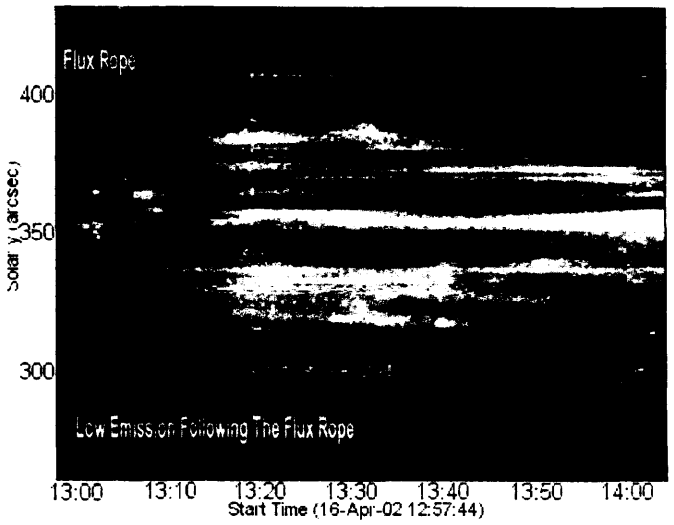

Figure 4.9: A synthetic slit image assembled from the *TRACE* data cube, designed to mimic the intensity data gathered from CDS.

entering the field of view, although clear loops are not seen passing through the position of the slit in the *TRACE* movies. This is likely to be due to the different temperatures observed by the two instruments.

The emission gap coincided with the passage of the X-ray source. Additionally it may also coincide with the X-line (current sheet) passage.

The Doppler velocity diagram shown in Figure 4.5 was formed over the same time period as the previous CDS image. However, it was seen that this extended region had a strong red-shifted component along the bottom and the remaining part was weakly blue shifted. To interpret this it was important to have a clear understanding of the loop orientations.

4.2.6.1 Magnetic Field Extrapolation

Figure 4.10 illustrates the presence of a single bipolar structure on the 5th April. Over the following days, numerous bipoles emerged and resulted in a complex region of magnetic activity. The flare loops appeared to connect opposite polarity magnetic concentrations, belonging to different bipoles. The shape and orientation of the loops in the active region

could be determined by producing a coronal field model and identifying the field lines that best match the observed loops. In this way it was possible to go from the 2D view given by the observations to the 3D view provided by the model. These 3D models (produced by C. H. Mandrini [1]) allowed the calculation of the three components of the magnetic field vector: one along the line of sight and two on a plane orthogonal to it. From the line of sight field component, the direction of the magnetic field vector and line of sight velocity measurements, the direction of the plasma flow at each point along a loop could be inferred again by C. H. Mandrini (see Harra et al. (2004)). The description which follows is supplied for completeness.

At the disk centre the component of the field orthogonal to the photosphere (B_z), which is the one used as a boundary condition in a magnetic field model, differs very little from the line of sight (B_l) value. Unfortunately, moving away from this position, the measured line of sight magnetic field becomes less representative of B_z. Furthermore, the field becomes highly distorted through foreshortening in places where the field vector is inclined to the vertical, e.g. in penumbrae. In this case, AR 9901 is located very close to the limb (W69 N22) at the time of the event. However, as done by Harra et al. (2004), a coronal field model can be produced using magnetic observations obtained some days before the arrival of the active region at the limb. The calculated field was rotated to the location of the region at the appropriate time and field lines that best fit the observed flare loops were computed.

A magnetogram from the Michelson Doppler Imager (MDI; Scherrer et al. 1995) taken on 14 April at 20:50 UT, 40 hours prior to this event was selected and the data were corrected assuming that the magnetic field vector was perpendicular to the photosphere. With these corrected data as boundary conditions, a coronal field model, under the linear (or constant α) force-free field assumption($\vec{\nabla} \times \vec{B} = \alpha \vec{B}$), was computed, using a fast Fourier transform method, as proposed by Alissandrakis (1981), which results in a semi-circular loop. When the MDI magnetic movie showing the evolution of the region

[1] C. H. Mandrini, Instituto de Astronomia y Fisica del Espacio, CONICET-UBA, CC. 67, Suc. 28, 1428 Buenos Aires, Argentina.

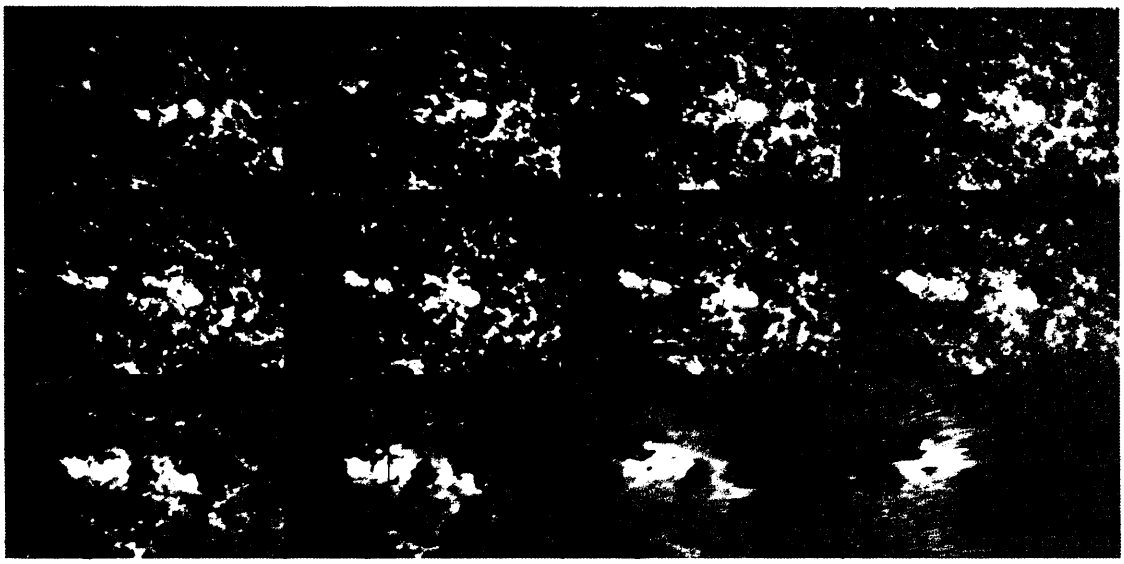

Figure 4.10: A time series of MDI magnetograms, rotated to central meridian position in the days running up to the event on 16th April 2002. One can see the evolution of the region from the top left to the bottom right where projection effects distort the image dramatically. In the image from 14th April a box is drawn representing the region over which the magnetic extrapolations were made.

is studied by eye, it appears that over the following two days the likely footpoints of the flare loops separate further, but errors are too large to consider using them as inputs to the model.

To determine the value of the free parameter of the model (α) an EIT (Delaboudiniére et al. 1995) image, taken on 16 April, overlaid on a co-temporal MDI map was used to identify the location of the magnetic footpoints of the flare loops, relative to the active region neutral line. After verifying that the orientation of the neutral line had not changed from April 14 to April 16 (using an MDI movie), the value of $\alpha = 1.5 \times 10^{-2}$ was determined. With this value, field lines that best match the EIT flare loops (whose shapes agree with those of the *TRACE* 195 Å loops seen in Figure 4.2) when rotated to the time of the flare, were determined.

The extrapolated field lines are shown in Figure 4.11. From the view of the extrapolated loops on 14th April, it was clear that the southernmost footpoints were to the west, whereas the northern footpoints were more to the east. This is important information

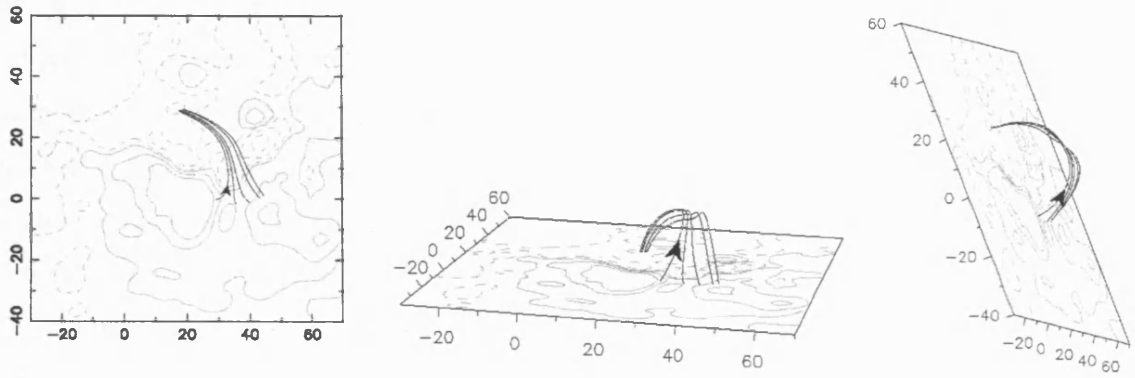

(a) (b) (c)

Figure 4.11: (a) Magnetic field lines extrapolated (local field of view, as if the AR is located at disk centre) in the linear force-free approximation (α=0.015 Mm^{-1}) using a SOHO/MDI full-disc magnetic map as the boundary condition two days prior to the event. (b) As in (a) in a different point of view to enable one to see the arcade orientation. (c) As in (a) with the AR rotated to the time of the event. The axes are measured in Mm and the field of view extends from 290″ to 428″ in the North-South direction and from 838″ to 977″ in the East-West direction (see Figure 2). The isocontour values are ± 100, 500, 1000 G.

which would be impossible to determine from the *TRACE* images alone. It should be noted that although the extrapolated loop is not a perfect match with the flare loop it does show consistency with footpoint positions. When loop shapes with slightly different footpoint positions were explored, practically all computed loops had the same plasma flow direction. It is also noteworthy that C. H. Mandrini multiplied the height of the loops by a factor of 2 to achieve a better match with the observations, but this did not influence the spatial orientation. When the magnetic field movie was observed there was continuing separation of the loop footpoints, but the numerical values of this field could not be used in the extrapolations as they were highly influenced by line of sight effects. With footpoint separation the loop apex is likely to be higher and hence a multiplication is performed, but the footpoint boundary conditions remain the same.

We can further relate the information of the magnetic field model to the CDS velocities to understand the direction of plasma flow along the observed structure, as done by Harra et al. (2004). Following the flux rope passage through the slit there is a time period where

the emission is very low. During this time, the coronal X-ray source passes through the slit and probably also the X–point. From about 13:10 UT we saw the cusp region, where the material had begun to cool back into the pass band. This was much hotter than observed by *TRACE* 195 Å, therefore it was not unexpected that these loops were not seen at the position of the slit. However, as the evolving flare–loop system was getting taller and the material was beginning to cool as it had come back into view it was likely to continue to fall. If one took the extrapolations to be a representation of the global loop orientation, then down-flows in the northern half of the loop would have a blue-shifted velocity and conversely the southern half would be red-shifted. We also saw enhancement of the blue-shifted values in the north. However, due to line of sight effects the red-shifted region can be foreshortened. Figure 4.5 shows a large grey region in the middle, possibly where the loop is almost perpendicular to the line of sight.

It was assumed that the velocities measured in CDS at both sides of the central region were mainly due to plasma flows along field lines whose shape and direction were similar to that of the extrapolated loops. From this it was possible to combine the direction of the line of sight velocity with that of the B_l (line of sight magnetic field component) along the legs of the computed loops with the vector magnetic field (see Eq.(1) in Harra et al. 2004) and attempt to determine the direction of the plasma flow. From the extrapolation it is found that B_l points towards the observer along both legs of the computed loops, while the line of sight velocity component (v_l) points towards the observer in the north and away in the south. The plasma appeared to be flowing down along both sides of the observed structure compared to the direction of the field given by the arrows on the lines in Figure 4.11. Therefore, it is suggested that hot material is falling along the newly reconnected loops as it cools.

4.2.7 The CME

The observed filament or flux rope, previously seen in the low corona, was later seen as part of a CME in LASCO (Figure 4.12). CMEs related to filament eruptions are thought to

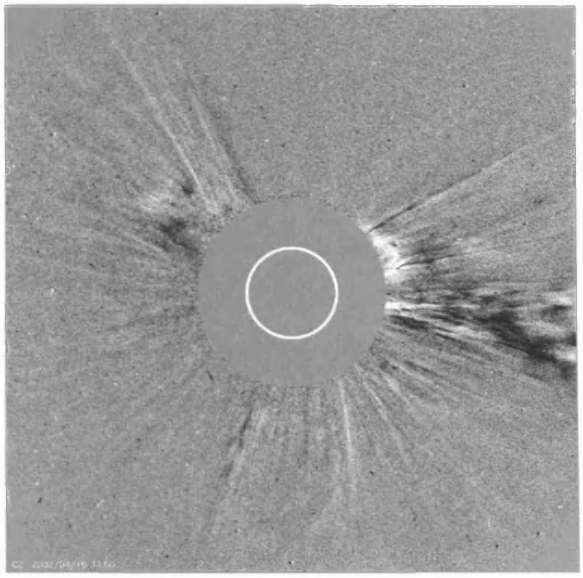

Figure 4.12: LASCO C2 difference image of the CME on 16th April 2002 at 13:50 UT, where the CME can be seen emerging from the occulting disk in the northwest.

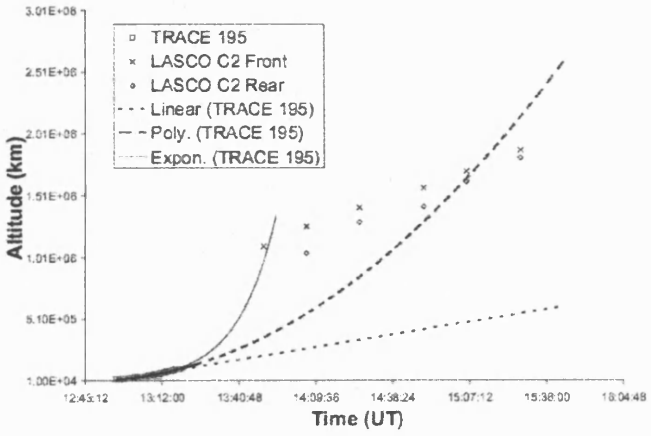

Figure 4.13: Height-time plot for the lifting flux rope as seen by *TRACE* and LASCO C2, with three different types of fit. The crosses represent the leading and trailing edge of the LASCO CME. We have an exponential growth, which can be seen to meet the required height in the required time. Also shown is a polynomial fit and a linear fit, neither of which can reach the required height in time.

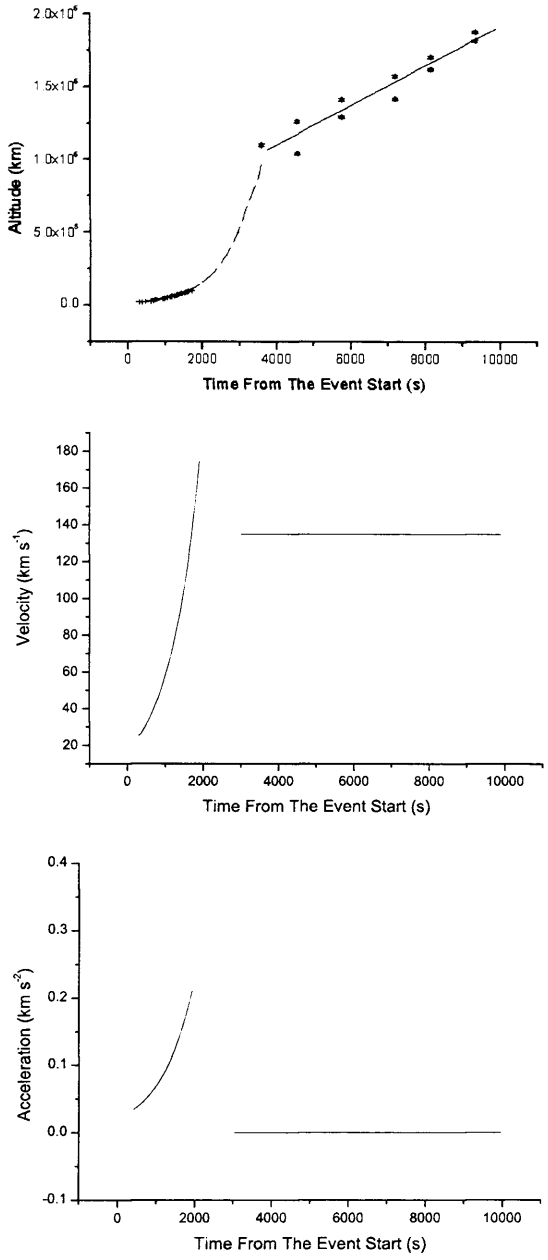

Figure 4.14: Height-time plot for the lifting flux rope as seen by *TRACE* and LASCO C2 with error bars representing five pixels. The dashed line represents the continuation of the exponential fit to the *TRACE* data. This is followed by the velocity profile and acceleration profile derived from the first and second derivative of the fits to the data.

have a three-part structure (Illing & Hundhausen 1985), indicating the initial leading edge seen in LASCO C2 is not representative of the leading edge in the *TRACE* 195 Å movies.

Recall that the three-part structure consists of a bright front, followed closely by a cavity, thought to be the magnetic structure of a flux rope and then a bright core region considered to be the filament/prominence material it contains. If we accept that the initial observations in *TRACE* 195 Å are of the flux rope, it was, therefore, not sufficient to simply measure the leading edge of the CME again in LASCO.

The CME observed was very slow and weak making it impossible to distinguish a clear three-part structure. It was thus decided to measure both the leading edge of the CME and also the trailing edge through the use of difference images. The front of the bright region signified the leading edge and the front of the dark trailing region was classified as the rear. This provided outer boundaries for the location of the previously mentioned flux rope.

With these additional points (Figure 4.13), obtained from LASCO C2, it become obvious that simple linear fits were not appropriate. It was impossible for a linear fit to be consistent with these combined observations as the required altitudes by LASCO C2 could not be reached in the available time. Instead some other fit was required to account for this rapid increase in altitude. Several samples of fits are shown in Figure 4.13. An exponential fit was most plausible, which ruled out a constant acceleration process. This fitted both the *TRACE* data section of the plot and also allowed the heights measured in LASCO to be achieved. This was consistent with the results of Gallagher et al. (2003) who had a similar plot for the 21st April 2002 CME. Note that their LASCO measurements were leading edge based, possibly giving a deceptively high value. However, an exponential rise is required for their dataset. In this event an exponential fit for the rapid rising phase and a linear fit for the LASCO section results in a fit with a high R^2 statistic (0.99 in the growth section and 0.96 in the linear region). When combined, it was possible to differentiate these to give a velocity profile and an acceleration profile as shown in Figure 4.14. The flux rope clearly slowed down following the peak, as throughout the linear phase the velocity remained constant at 135 km s^{-1}. Although a dashed line from

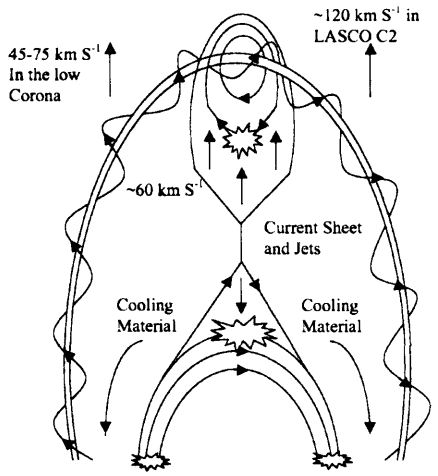

Figure 4.15: Cartoon representing the entire event, based upon observations from all instruments.

the end of the *TRACE* data to the beginning of the C2 observations was plotted in the top part of this figure, it was not differentiated for the following two parts. This was because there were no data for this section and any differentiation would be based on guess work.

4.3 Discussion

These findings can be summarised in the diagram shown in Figure 4.15, based on a model suggested by Shibata et al. (1995). However, velocity information for the event studied above has been added. The diagram illustrates the lifting flux rope, below which is the current sheet where reconnection occurs, and finally beneath this are the cooler flare loops. Traditionally at the footpoints of these flare loops there is hard X-ray emission from the collision of high-energy electrons impacting the dense chromosphere. However, in this event, footpoint emission was much lower than expected due to the unusually dense loop top (Veronig & Brown 2004).

The lifting filament/flux rope was seen in *TRACE* 195 Å and CDS Fe XIX, followed by the CME in LASCO C2. It was best shown in Figure 4.3 where the *TRACE* images covered a smaller field of view. The reason for this lift off is unclear and many models

attempt to explain it (e.g. Forbes 2000; Török et al. 2004). With careful study of the *TRACE* 195 Å movie it is apparent that there is some global deformation of the flux rope system, which might suggest kinking, although quantitative measurement of this is difficult. As the filament/flux rope rises it crosses the CDS slit field of view (Figure 4.5). The Doppler velocities from the same figure indicate that there is an inherent helical structure of the loop, highlighted by helical flows. A similar observation was made for an on-disk flux rope by Foley et al. (2001) and Pike & Mason (2002). They found that there was significant blue shift attributed to the rising flux rope and a red shifted component, either attributed to an untwisting of the flux rope or to falling material. In the case of the 16th April 2002 red and blue shifted emissions were found on opposing sides suggestive of helical flows.

From Figure 4.15, as the flux rope begins its lift-off phase, it would drag overlying arcade magnetic field lines with it. This would stretch the field beneath it forming a current sheet. At this point magnetic reconnection could begin producing strong outflows (jets) from the reconnection region as well as flare loops. The *RHESSI* observations of this event show that the flare loop top source was unusually bright relative to the footpoints. Assuming that this event was homologous with those of the previous two days, then it can be described as a loop which is collisionally thick at electron energies up to 50 keV (Veronig & Brown 2004). There was a coronal source observed up to 25 keV as shown in Figure 4.6. This source moved upward and follows the rising flux rope with a comparable velocity to that of the flux rope at a distance of roughly 20,000 km, implying an intimate link. It is suggested that this indicated the formation of a plasmoid like that previously observed by Tsuneta (1997). This source was tracked by plotting the brightest point location and is shown in the height-time plot of Figure 4.4.

From Figure 4.5 we see that following the passage of the flux rope there was a period of weak emission. This corresponded to the passage of the coronal X-ray source and may also correspond to the magnetic X–point or current sheet. When one studies the *TRACE* 195 Å movie closely, the brightening of loops and the formation of a cusp can be seen, the peak of which is located around the position of the CDS slit at the time of the gap. At

this point the emission measure would be low and little emission would be expected as the volume is very small. This was also apparent if one studies the stack plot from *TRACE* in Figure 4.9. Even in that case there was little emission in that location and time period.

Following this time there was an extended period of about 90 minutes when the velocity pattern was suggestive of down–flows along the hot, newly reconnected loops. The Doppler velocities seen by CDS in Figure 4.5 suggested that when taking into account the orientation of the loop determined through magnetic extrapolation (Figure 4.11) we were seeing the falling material either coming towards or moving away from us. It is believed that observations represent this rather than general loop shrinkage as the largest Doppler shifts are seen to be at the edges of this expanded region with much lower velocities in between. However, it is very difficult to distinguish between these two mechanisms with the available data. It may be that this grey region represents the global shrinkage and the bright edges are from the loop leg down-flows.

The flux rope continued to rise and was observed as a CME in LASCO C2. The leading edge was measured along with the rear of the CME and the two lines were plotted on the height-time plot, which could be seen in Figure 4.14. It was clear that a massive velocity change would be required in order to reach the C2 heights in the available time. Only the exponential function could provide this. This exponential growth is present in ideal instabilities such as the kink instability simulations by Török et al. (2004) and Kliem et al. (2004). These authors suggest the kink instability of a coronal flux rope as a possible initiation mechanism of solar eruptions. These data suggest that the CME has either reached a steady state by the time it is observed by LASCO or is slowing down. Gallagher et al. (2003) presented an event with a very similar profile with additional data from UVCS which provided a valuable point between *TRACE* and LASCO. Even without this it was possible to show that an exponential function was required to produce the altitudes required in the allotted time frame.

The fit shown could also be differentiated to give velocity and acceleration profiles. It is shown that this event falls in the impulsive acceleration category defined by Zhang et al. (2004). Much like their event, it can be described in a three-phase scenario. First

there is the initiation phase, characterised by the slow rise in the corona. In this case it corresponds to the *TRACE* 195 Å observations. This was observed over some 24 minutes with a maximum velocity of ~100 km s^{-1}. Throughout this time period the GOES light curve began to rise to a peak at ~ 13:25 UT.

The second phase, characterised by a rapid increase in velocity, was the most problematic to profile due to a data gap throughout this phase. However, using the LASCO data and the end of the *TRACE* data as limits one can be confident that there is a rapid velocity increase during this time. The rising filament actually sped up by a factor of 1.7 at the start of the impulsive energy release and as our fit shows was required to accelerate further before reaching 1.5 solar radii and then decelerate again before joining the line of points observed by Lasco. During this time there is rapid increase in soft X–ray emission.

The third and final phase was merely a propagation phase with little or no acceleration. This case indicated that the acceleration fell to zero, as suggested. A linear fit describes the final stages indicating the velocity dropped to a mere ~ 135 km s^{-1}. This phase corresponds to the decay phase of the *GOES* light curve.

We found that like the work of Zhang et al. (2004), the second phase corresponded to a rapid increase in GOES flux. However, this rapid increase began earlier in initiation phase suggesting that the X–ray emission rise is coincident in time with the CME initiation phase, implying a physical link.

4.4 Conclusions

It is shown that the 16th April 2004 event was associated with a flux rope (filament) lift, forming a CME. This CME had a height-time profile that required an exponential fit to achieve the observed altitudes in the given time. This exponential growth suggested that the acceleration was caused by some kind of instability, which may be attributed to the kink instability in the rising flux rope. As the flux rope / filament lifted it was seen to have helical flows, suggesting a helical magnetic structure demonstrated through Doppler measurements with CDS.

Observations from *RHESSI* indicated that the loop top source was much brighter than the footpoint sources, similar to those first observed by Veronig & Brown (2004). In addition, however, there was a coronal source that appeared to follow the rising flux rope, and was above the top of the cusp with a velocity comparable to that of the rising flux rope. It was likely that this demonstrated *RHESSI* manifestation of the plasmoid observed by Tsuneta (1997). However, the present work was able to link observationally the plasmoid to the rising filament/flux rope structure for the first time. The coronal source passed through the CDS slit although it could not be seen in the Fe XIX pass band, as it was almost certainly too high in temperature and too low an emission measure.

From study of the CDS Dopplergrams it was seen that in the cusp region under the expected location of the current sheet there were likely to be down flows along the newly reconnected loops. These contained hot material, which was cooling and falling back towards the surface.

Chapter 5

A Series of Confined Flares with an Associated CME

5.1 Introduction

So far I have studied small confined flares (chapter 3), followed by an explosive event (chapter 4), where the related CME was tracked from the low corona. This chapter addresses a series of events which display characteristics of both a confined and eruptive nature.

Presented in this chapter is a series of quadrupolar flares. They occurred in quick succession in a single active region southwest of the disk centre. The first two of these events appeared confined in nature while the third was an LDE, which are more commonly associated with CMEs. Subsequent LASCO observations and radio observations show a CME leaving the region at an earlier time than would be expected from consideration of the LDE alone. This apparent contradiction suggests that the preceding small-scale quadrupolar flares were related to a large scale CME through the interaction of field lines, created during these flares, with neighbouring open field lines. Shock-waves, observed at radio wavelengths, related to the confined flares appeared to form part of the CME as well, or to assist in the opening of the large scale field. This chapter presents a comprehensive

study of this flare series and CME over many wavelengths concluding with a cartoon description of the proposed scenario for the sequence of events that led to the CME.

5.1.1 Quadrupolar Flare and CME Models

A quadrupolar flare has four footpoints that are represented by individual flare ribbons in separate magnetic regions. A model for quadrupolar confined (non-eruptive) flares was developed by Melrose (1997) (see Section 1.3.4.3) and observationally modelled by Aschwanden et al. (1999b). This model was based on the reconnection of two current carrying magnetic loops. The 3D reconnection had a single common neutral line for the two interacting loops and does not involve any opening of field lines, thus no CME was possible. Confined (i.e. non-eruptive) 3-D quadrupolar reconnection was also studied via modelling of the location of separatrices and quasi separatrice layers (QSLs), where reconnection is likely to occur and relating them to observed flare ribbons (e.g. Sweet (1958a), Gorbachev & Somov (1988), Mandrini et al. (1991), Demoulin et al. (1993) and van Driel-Gesztelyi et al. (1994))

A further quadrupolar flare/CME scenario was developed by Antiochos et al. (1999) (see Section 1.3.4.4), in which a central magnetic arcade of increasing shear reconnects with a large scale and oppositely orientated arcade of overlying field lines. The central arcade is being sheared, and therefore rises, but is restrained by the overlying field. At the apex the overlying field lines and the rising arcade are anti-parallel. At this leading edge a current sheet is formed leading to magnetic reconnection, resulting in a removal of the restraining field lines. Thus the sheared core field could burst through creating a CME. After the CME leaves, the field lines close down slowly as they relax, hence an LDE occurs, leading to the formation of flare loops and a two-ribbon flare at the footpoints. These two-ribbon events are discussed in more detail in the introduction. Flare kernels may appear in the side lobe magnetic polarities as well though they would appear weak over large distances making their observation difficult.

A further development of this 2.5D model came in the form of the 'lateral magnetic

break-out model' of Aulanier et al. (2000). This model started with the same quadrupolar setup as before although it was asymmetric; the sheared arcade was one of the side lobes. When shear is applied along the neutral line, the side lobe starts to expand and weak reconnection is triggered at a coronal null point, which creates longer field lines overlying the sheared arcade. Since longer field lines have weaker magnetic tension, they provide less restraining force, thus the sheared field can expand and open up. Reconnection between open and oppositely orientated field lines leads to the formation of footpoint ribbons through electron precipitation and post flare loops become apparent with continuing relaxation.

Presented here is a series of flares, which have an associated CME but unusually have a clear quadrupolar nature. The orientation and loop structure does not, however, fit with the breakout scenarios suggested above. Rather it seems that some interaction between small scale flaring and the large scale magnetic field produces the observed CME.

5.2 Event Description

On the 20th January 2004 a three-phase eruptive scenario was observed with *GOES* . They are three flare events which are all intimately linked and will thus be considered as phases of an event. The light curve for this event is shown in Figure 5.1. When this was compared to the light curves observed by *RHESSI*, a similar three phase pattern was seen (see Figure 5.2), in X-ray energies up to 50 keV. The emission began to rise at approximately 07:32 UT and peaked at about 07:37 UT. At 07:40 UT the second phase appeared to begin, peaking at around 07:43 UT and decaying until 08:00 UT. It was here that the third and final phase of the flare trilogy began with a Long Duration Event. This was much smaller, C-class rather than M-class as the previous two. It peaked just three minutes later and then continued to decay until 11:00 UT. It is difficult to be more precise with the flare timing as the different phases overlap.

These events were observed in numerous wavebands with many different instruments allowing a full data set for the analysis which follows, and providing an ideal opportunity

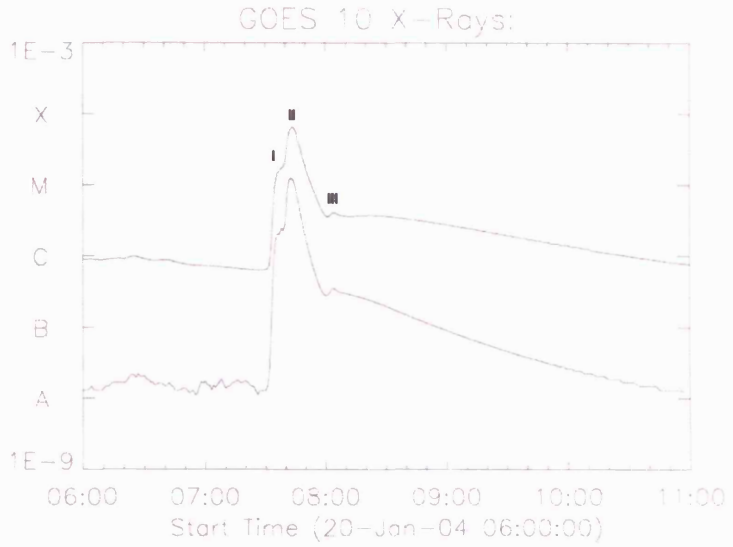

Figure 5.1: *GOES* light curve for the 20th January 2004 07:32 UT event. The three phases of the event just after 07:30 can be seen and are numbered. The first two events are impulsive flares, the third one is a long–duration event (LDE)

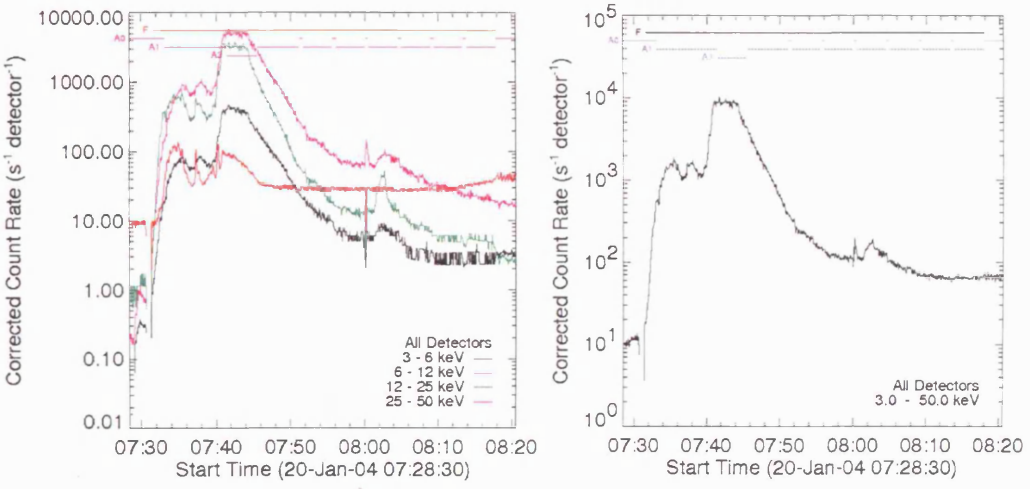

Figure 5.2: Left: The observing summary data for the 3-6, 6-12, 12-25 and 25-50 keV energy bins of the *RHESSI* data are shown. The three phase nature of the event is also evident. Energy bins above this were flat and featureless and were thus omitted to improve figure clarity. Right: This curve is the sum of those to the left.

to investigate how a CME can have originated from this series of flares.

5.2.1 Flare Ribbon Analysis

5.2.1.1 *TRACE* and H-Alpha Image Description

TRACE was observing in the 1600 Å pass band during this event. The field of view covered the entire active region responsible for the flaring emission. The images had a pixel size of 0.5″ and a varying cadence of between 3 and 60 seconds. It was therefore important that each frame was normalised for exposure time for direct comparison. For the full process involved in calibrating the images refer to section 2.5.2.1. There were, unfortunately, two data gaps during the flare where *TRACE* lost pointing. The first was between 07:33 and 07:51 UT and the second followed by phase-III at 08:04, ending at 08:37 UT. The first data gap occurred during the transition between phase-I and -II. However, it was possible to obtain H-alpha images from the Kwasan observatory (courtesy of Prof. Kurokawa), which filled this gap to some extent. These were digitised from film and supplied as a simple mpeg movie. The frames from this movie were aligned with the *TRACE* images using the two sunspots as reference points enabling the progress of the events to be followed qualitatively.

When the ribbons in these images were studied, the three phases of the flare could be clearly distinguished. Figure 5.3 illustrates the ribbon progression. The top left image shows phase-I clearly. This was predominantly composed of two large ribbons to the east of the image with a smaller ribbon to the west. The second image shows the same region in H-alpha and shows the progression from east to west. This progression can be seen in both the north and the south, where there is a super-granular cell boundary. At this boundary the magnetic field builds up due to large-scale convective motions, which led to an elongation of the H-alpha footpoints. In image 3, phase-II is well under way following the data gap and the flare ribbons of phase 1 have faded. There were three ribbons in the centre and additionally there was remote brightening in the far west sunspot. Additional ribbons to the west of the top two regions were thought to be responsible for phase-III in

image 4.

From the *TRACE* images it was possible to look at the relationships between different areas with the use of light curves. Small sub-regions of these larger images were selected and the pixel values in each frame summed. These values were plotted against time and the regions compared, the results of this analysis are shown in Figure 5.4. This gave a better understanding as to which regions and ribbons are associated with flares from particular phases.

It is clear that regions 2 and 4 were almost exclusively emitting during phase I, while 1, 3, 5, 6, 7, 8 were predominantly related to phase-II. Some of the light curve increases are subtle, but when viewed in comparison with the images, clear involvement is observed. The final phase was related to regions 1, 5 and 6, although the brightening in region 1 is very small and is difficult to determine whether the increase is due to the beginning of phase-III or the ending of phase-II.

Limitations The regions used for the light curves are by no means perfect. We first note that some of the boxes overlap. In an ideal world this would be avoided. However, in this case the boxes are designed to represent regions of observed activity in both the *TRACE* 1600 Å and the H-alpha emission.

Also even during phase-I there is a small amount of emission in the regions which we later discuss as phase-II. This is likely due to phase-II beginning before phase-I has ended as flaring cascades to the west. There is evidence for this in the light curves (Figure 5.2). It is clear that phase-I and phase-II overlap.

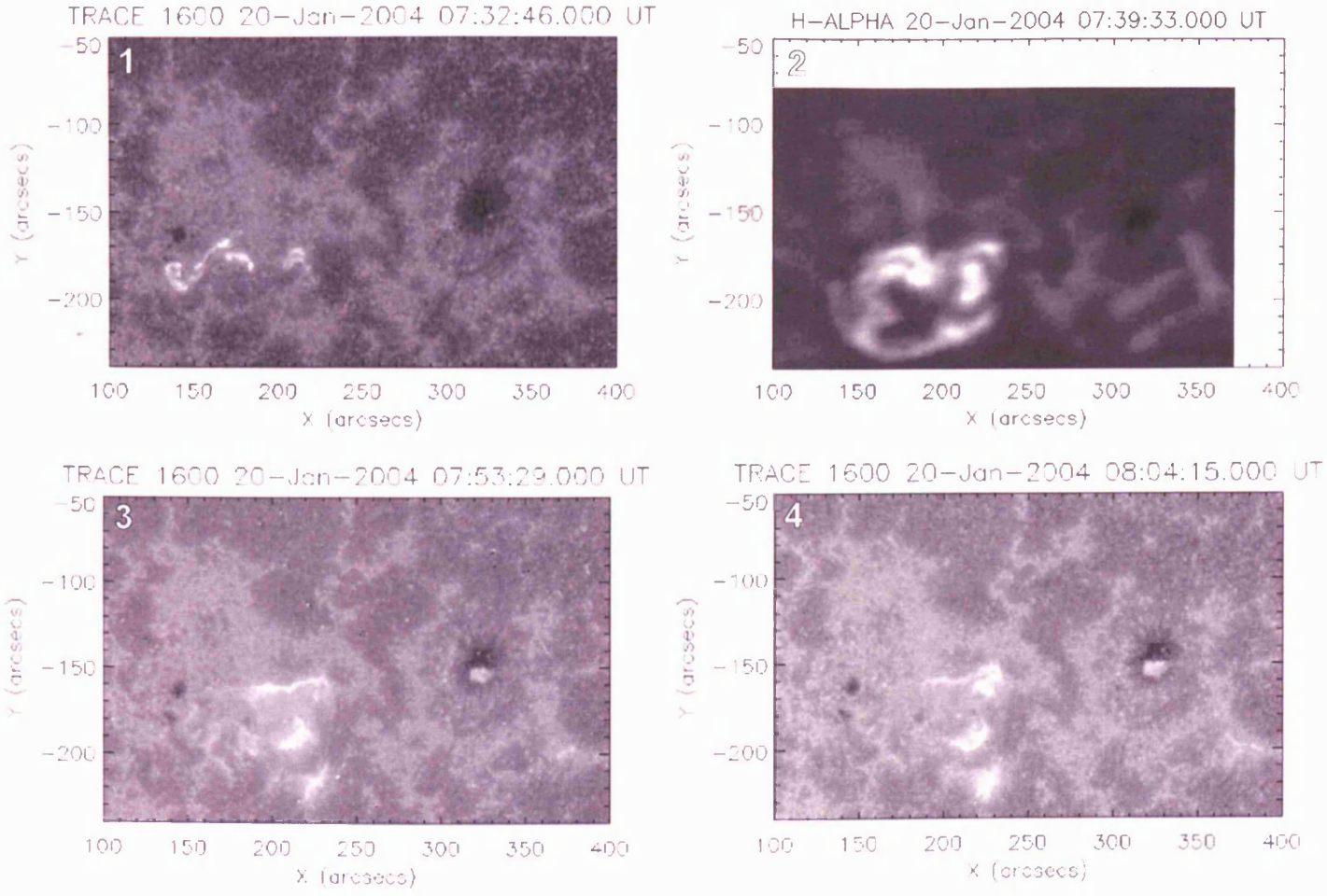

Figure 5.3: Shown here is the progression of the flare ribbons. The images go from 07:32 UT in the top left to 08:14 UT in the bottom right. All but one of these comes from the *TRACE* 1600 Å dataset but the second image is a ground based H-alpha images from the Kwasan observatory. These images show all of the flare phases.

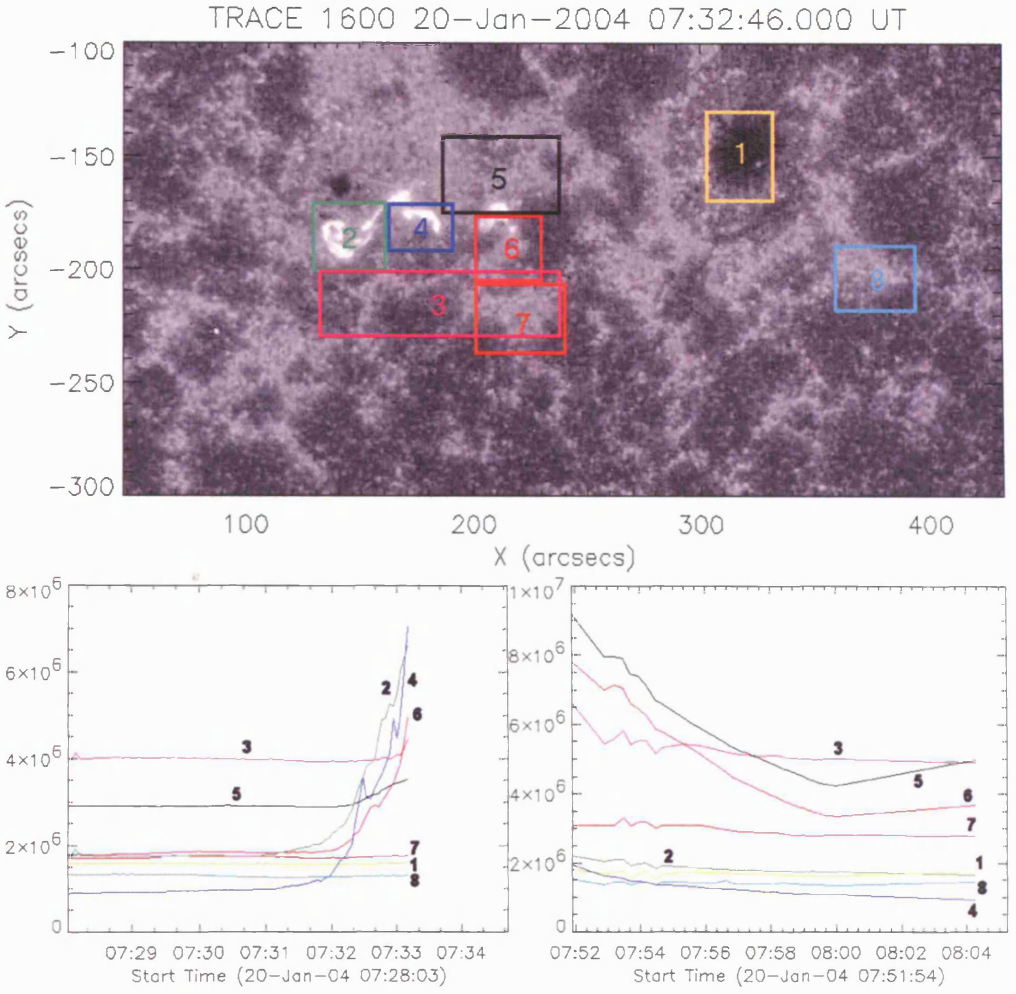

Figure 5.4: The *TRACE* 1600 Å image above is from the flare phase-I recorded at 07:32 UT. Over this image are coloured boxes which all represent regions over which light curves were determined. The intensity is measured in *TRACE* DN. In the plot below are these light curves which are coloured in the same way as the boxes above. The long straight section in the middle of these curves is due to the data gap.

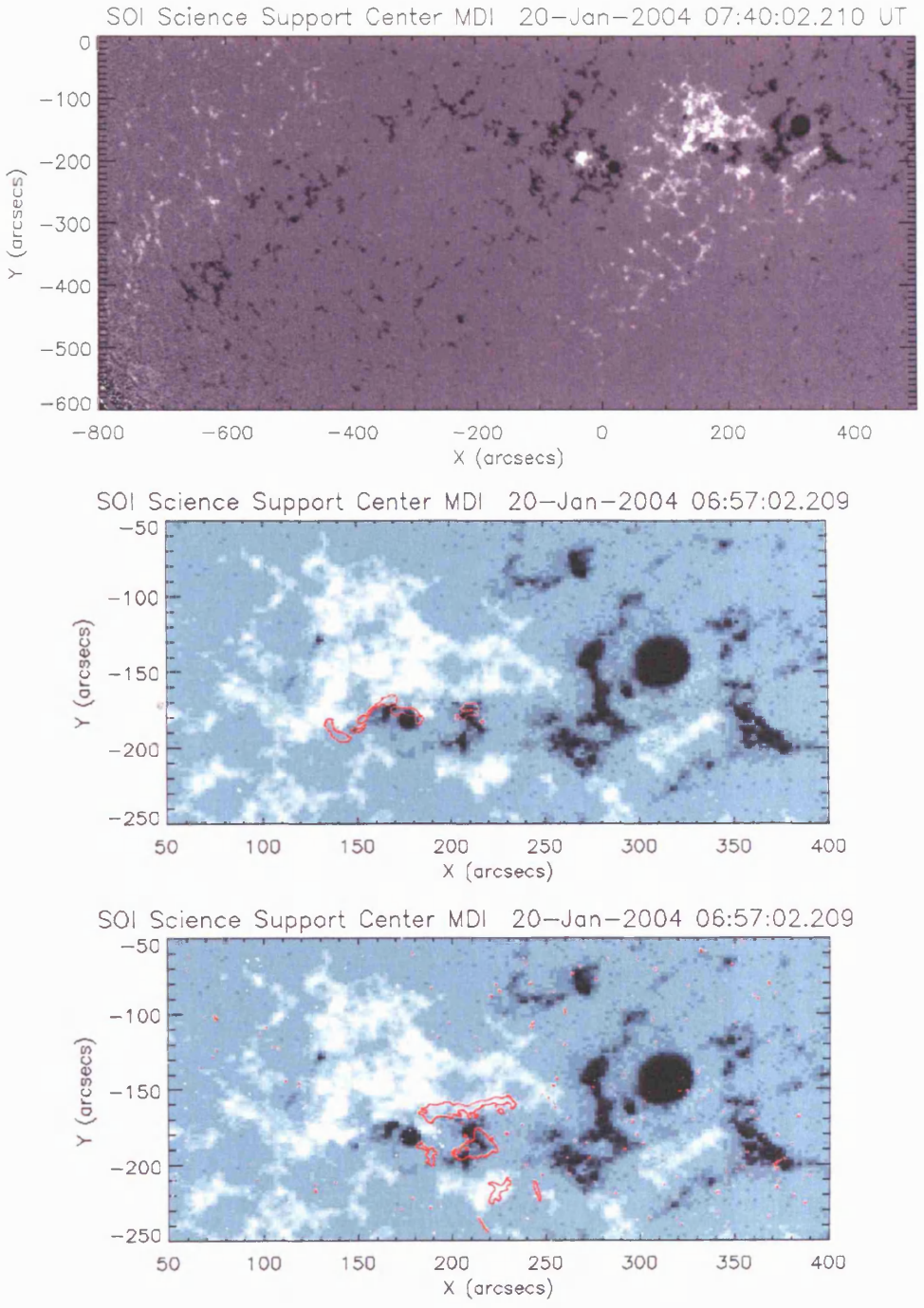

Figure 5.5: The top image is a magnetogram from MDI. This is a very wide section showing the flaring region on the southwest and a dispersed active region to the east over which lies a large streamer. The bottom two images both show the MDI region with *TRACE* contours at 20% to show the ribbons in phase-I and -II respectively.

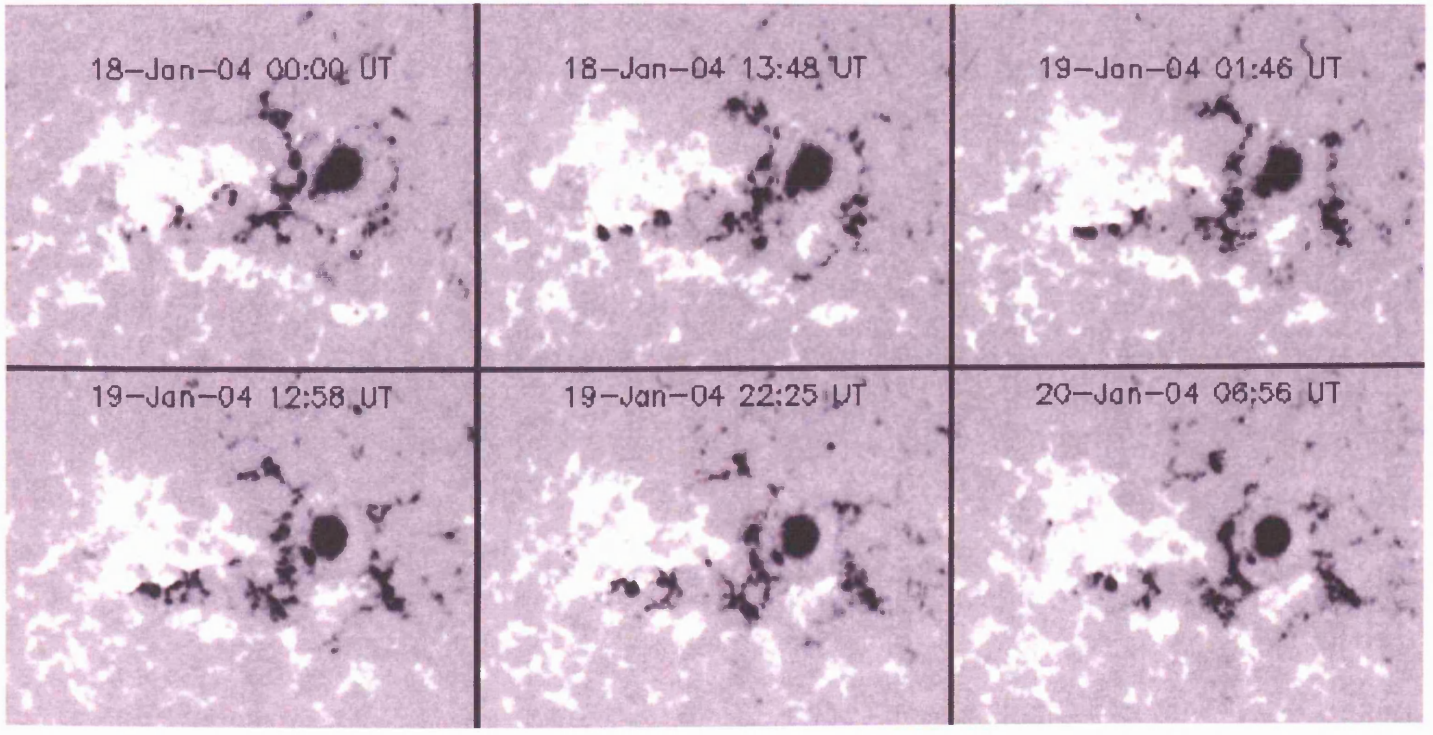

Figure 5.6: An MDI sequence showing the magnetic evolution of the active region from 18th to 20th January. Note the emergence and subsequent motion of several new bipoles along the south border of the dispersed positive polarity (white).

5.2.1.2 MDI Magnetograms

The *TRACE* images may be compared to MDI magnetograms. An overview of the region is shown in an MDI magnetogram close to flare time in Figure 5.5. Below this are two smaller regions with *TRACE* contours displayed. The phase-I ribbons were situated either side of a magnetic neutral line, as would be expected, but phase-II seemed to have the northernmost and southernmost ribbons in positive polarity field and the central ribbon in negative field (Figure 5.5), with an additional ribbon over the big leader spot of negative polarity.

Over the period from the 18th-20th January 2004, numerous bipoles emerged building up magnetic complexity within the active region (Figure 5.6). By studying the emergence of these bipoles it was possible to derive, by inspection and comparison with the *TRACE* light curves, the probable magnetic connectivity between regions. It is assumed that as a new bipole emerges it has no connections to the surrounding magnetic field. The emerging bipole is a cross-section of a single magnetic flux tube with the photosphere and therefore represents the original magnetic connectivity. Any magnetic reconnection would take place between the new bipole and pre–existing fields. For the sake of simplicity, we assume that prior to the flare event no other reconnection took place. This original connectivity is represented as image 0 in Figure 5.7. In these figures blue ovals represent regions of positive polarity and yellow ovals represent regions of negative polarity. Each of these regions represents a single magnetic pole. The regions were part of bipoles seen to have emerged over the previous few days (Figure 5.3 and Figure 5.6). These regions were determined by eye after careful study of the magnetic movie. The size and shapes are qualitative, but show a correlation to the regions observed to emerge. They demonstrate that phase-II resulted from the interactions of at least three bipoles. They are shown in the figures 2a and 2b as separate events for clarity, although both represent phase-II.

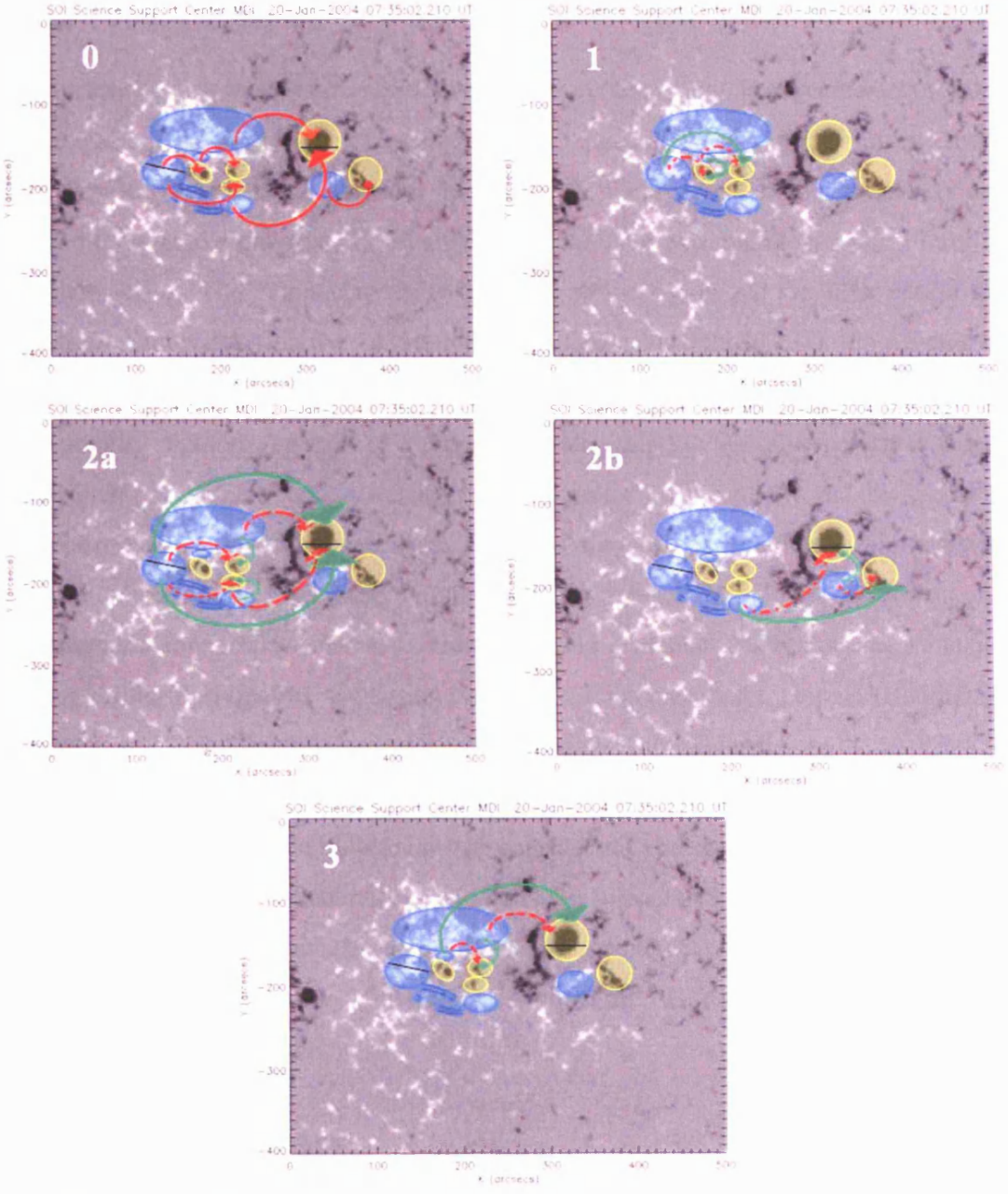

Figure 5.7: This figure shows an MDI magnetogram at the flare time. Over this a series of blue and yellow regions have been highlighted. These represent positive and negative regions respectively. Image 0 represents the deduced original magnetic connectivities. These connectivities are illustrated with red arrows. Image 1 illustrates the changing magnetic connectivities due to phase-I. The red dashed arrows are previous connectivities and the green are the new connectivities. The following 2 images represent phase-II and the final represents phase-III, again with red arrows indicating pre-existing connections and green indicating new connections.

5.2.1.3 Flare Progression

The series of flares was part of a general progression of magnetic field reconnection from east to west. Each flare led to a rearrangement of magnetic field lines, evolving the magnetic topology and making a further flare likely. This progression is more clearly explained through the diagrams in Figure 5.7. There were two dominant neutral lines in this flare series. The first was in the north of the active region and the other was in the south. The emerging negative polarity regions pushed against the large positive region to the north and smaller positive region to the south as they moved westward. These positive polarity regions were part of a pre-existing large dipole. As these polarities move, shear is created at the boundary leading to accumulation of free energy and, by approach of opposite polarities, reconnection, i.e. flaring is triggered. As the first flare progressed it acted to create long field lines, with less tension, through magnetic reconnection. As the magnetic connectivity changes, further reaching reconnections became possible, allowing further flaring. The decreasing magnetic tension provided by longer (stabilising) magnetic loops may have facilitated a partial filament eruption leading to the LDE.

All the flare phases were represented by quadrupolar footpoint emission and, looking at the configuration, would traditionally be considered to be confined except for the third phase, the LDE, which is generally considered to be related to the field lines closing down following an eruptive event. However, at least one component of the CME (i.e. the frontal part) related to this region was observed from about the LDE time, thus had to originate prior to the start of the LDE.

5.2.2 Associated CME

There was an associated CME with this series of quadrupolar flares along with numerous signatures of open field lines. These signatures and their implications will be discussed below.

5.2.2.1 LASCO

LASCO observed a CME in C2 (data calibration can be seen in Section 2.4.3.1), the core of which became visible at 08:30 UT and which, if assumed to be released radially, had a large forward velocity component towards the Earth. However, when observed in the plane of the sky it moved in a southward direction. This was evident in both the C2 and C3 fields of view and is shown in Figure 5.8. In the southeast there was a streamer which appeared to be rooted in the large active region to the east of the flare site. This streamer is observed to shift back and forth in the east-west direction as the CME propagates, first observed at 08:08 UT. This implies there is some interaction below the occulting disk. This is clearly apparent when the data are viewed as a movie but is less obvious when static images are considered.

The flaring region may also have an associated streamer, but due to its position on the disk any such streamer would be difficult to observe in LASCO at the flare time. If one assumes that these structures are stable and long lived, the data from the following days can be considered for evidence of these large structures. As the Sun rotates, any streamer over the flare region will become more in line with the plane of the sky. Thus using this method it was possible to identify that, in this event, a streamer did exist above the flaring region.

The CME was clearly observed with running difference images, in both C2 and C3, and was seen to have what was thought to be a traditional three-part structure. These images were constructed by simply subtracting consecutive images allowing the observer to see subtle changes. The leading edge shock was very faint and is again difficult to show in a static image, but the core is clearly seen in Figure 5.8. It was possible to plot height time profiles for both the C2 and C3 fields of the fast frontal leading edge as well as for the core leading edge. These can also be seen in Figure 5.8. The frontal leading edge was first detected at 08:06 UT, just minutes after the beginning of the LDE. These plots were made using a simple point and click method where the altitude is recorded along with the observation time and when repeated were always within ± 5 pixels. It was seen that once

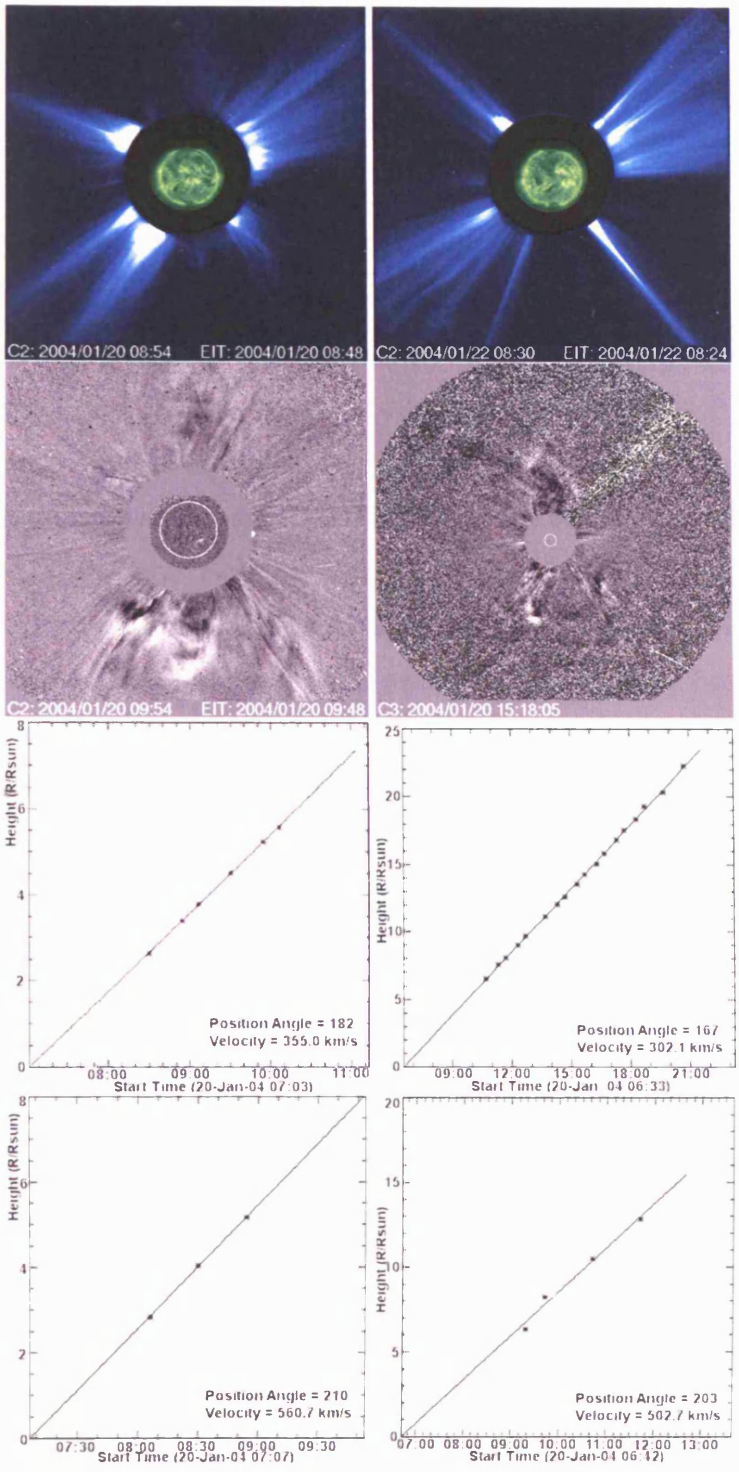

Figure 5.8: The top two images show white light LASCO C2 images. The first shows the faint CME from the event and the second is two days later showing the streamer over the active region. The following two images are running difference images from C2 and C3 showing the CME. The top two height time profiles are for the CME core and the bottom two are the CME shock front.

the CME was out as far as the field of view of C2, it was not accelerating and thus moving with a constant velocity. The leading edge shock was moving at between 502 and 560 km s^{-1} and the core was moving with a velocity between 300 and 350 km s^{-1}. The range is most probably due to the change in the image resolution between C2 and C3 images. We should recall that this is not a true speed for the CME as it is only measured in the plane of the sky and there is a large velocity component towards the Earth. In addition, the CME expands with altitude. Thus the velocity measured will have included a component of this expansion speed.

Extrapolating the height time plots for the CME core back in time linearly gives an estimated CME onset time of around 07:00 UT clearly well before the LDE, which started at about 08:00 UT. However, we can compare this to the CME onset time that could be derived from the backward extrapolation of the LASCO data in chapter 4. In this case lift-off was observed by *TRACE* . In this case it was found that the linear back-extrapolated CME lift-off time was about one hour earlier than the actual lift-off time, due to the acceleration of the CME in the lower corona. This would mean that it is possible that the CME core in this chapter could actually originate from the LDE, especially as this CME was much faster when observed in LASCO. However, there will follow some discussion on the origin of the CME front.

5.2.2.2 EIT 195 Å

EIT was observing the solar disc with ~12 minute cadence in 195 Å . This data allows the use of difference imaging to determine the likely region from which the CME originated. By taking base difference images one can look for reduction in emission. This is referred to as EIT dimming (Thompson et al. 1998). The region is believed to dim either as material leaves the field of view along open field lines, resulting in less emitting material or as the result of expanding structures. As structures containing emitting material expand the emission measure drops as the same amount of plasma is now occupying a larger volume.

To assess the effects of dimming, a time series of images is required, and then a sub-region of this can be taken. The pixel values can be summed in each of the sub-images and their intensity plotted with time (Figure 5.9). This was done in 4 main regions of the solar disc.

Dimming was most obvious in the bottom right light curve over the flaring region and regions extending southwest. At approximately 08:00 UT there was a significant dip in the light curve which lasted for nearly two hours. This dimming followed a sharp peak which was representative of the flare brightening. In the northeast there was a slight dimming which started around 06:00 UT and lasted for some three hours; this is likely to be unconnected. The other quadrants changed little or even increased in brightness.

In addition to the dimming with EIT it was possible to see some of the magnetic loop structure. Following the flare activity it was clear that most of the flaring loops have an east-west nature. This would suggest that the flaring has caused a steady build up of these longer field lines giving extra weight to the magnetic connectivity arguments of the earlier discussion.

As described earlier there was a large and dispersed active region to the east. These two regions were separated by a large neutral line most clearly seen in the wide MDI image in Figure 5.5. Until now base difference images have been used, which were good for seeing long term change. However, a running difference can show more subtle changes from image to image. In the running difference images around the flare time, connectivity between the two active regions could be identified. The image shown in Figure 5.10 was the difference between the 07:47 and 07:35 UT images. This spanned phase-I and the beginning of phase-II.

The left arrow in this figure points to this connecting region. At the arrow tip there is a dark region and further north are brighter regions. This suggests that there are new loops being formed and relaxing down. The dark region suggests there was material there in the previous frame and the bright region suggests there is new material not present in the previous image. One can see in Figure 5.10 that there is an overall brightening in the connecting region which begins somewhere between 07:25 and 07:36 UT. It is not

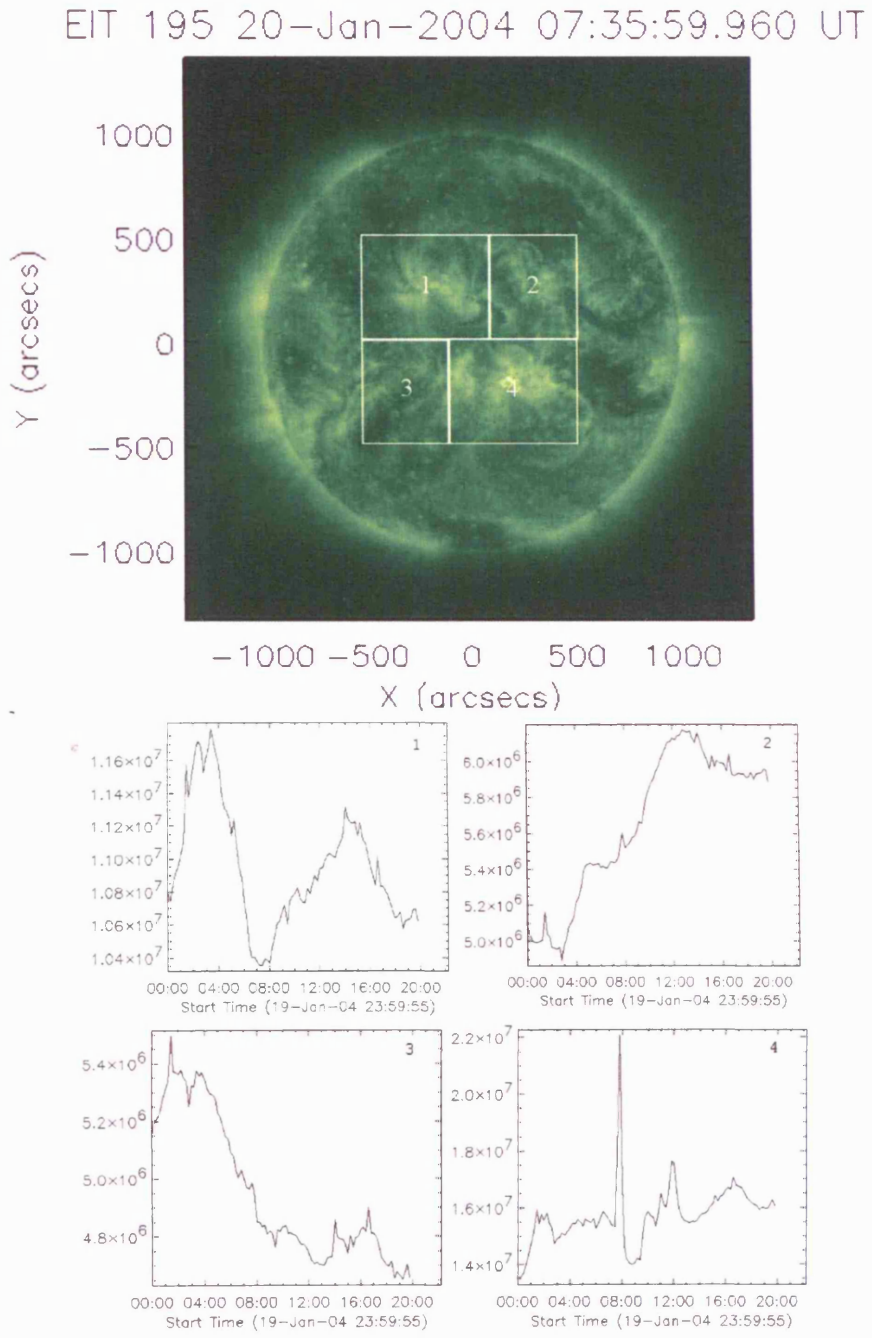

Figure 5.9: This figure shows EIT sub-regions and their respective light curves where intensity is shown in DN. The final image is from the active region in question and dimming is clearly seen following the flare brightening.

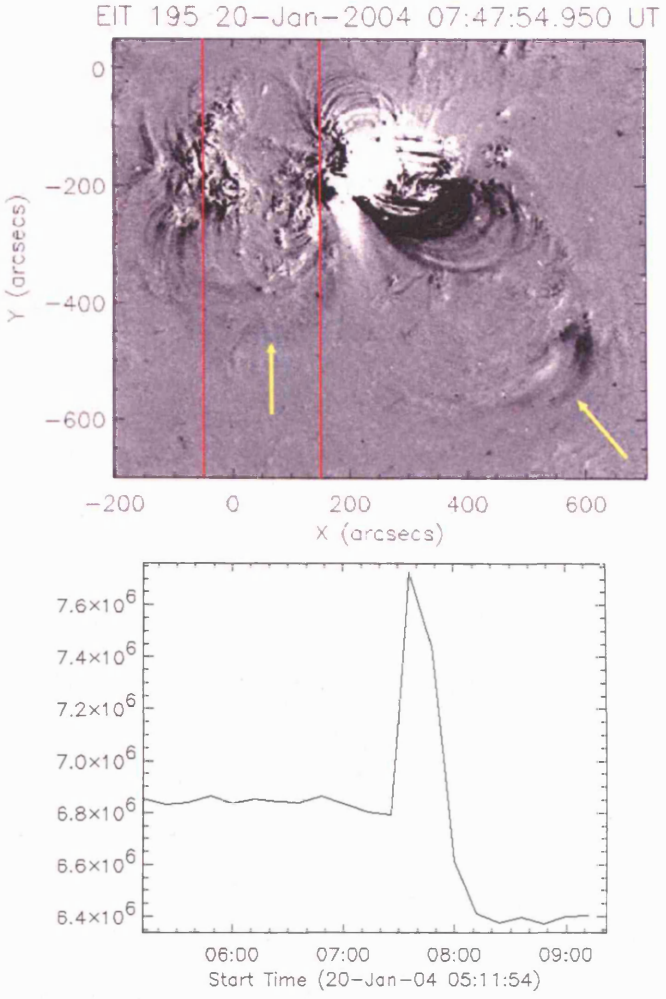

Figure 5.10: The top image is a running difference image. It shows the connectivity between the large dispersed active region and the flaring region; the yellow arrow to the left points to this connectivity. The other yellow arrow points to a region where very large expanding structures are seen. The two red lines demonstrate the region selected over which the bottom light curve (where intensity is measured in DN) was constructed.

possible to make this time more precise as one is limited by the cadence of EIT which is approximately 12 minutes.

To the west there are large expanding loops which are seem to move away from the flare region. It would appear that they originate above the region and may be expanding due to flaring activity beneath. By combining this observation with the connectivity between the two active regions, it is apparent that as the loops expand, they are reconnecting in the east with open field lines, corroborating the LASCO observations showing the streamer deflection.

5.2.2.3 Radio Emission - Type-II Radio Bursts

Also observed during this series of flares were type-II and type-III radio emissions, where the latter are due to fast electron beams propagating along open field lines. There appears to be a general consensus that type-II bursts are shock waves, which may form in front of fast CMEs. However there is also the possibility that they are simply flare generated blast waves (e.g. Gopalswamy et al. (1998)).

The type-II bursts manifest themselves as radio emission at the local plasma frequency and often at the second harmonic. The observations show a drift from high to low frequencies with time, indicating a moving source. This is an atmospheric effect, as the density drops with altitude so does the plasma frequency. With a good density model the frequency can be related to altitude and thus the speed of the disturbance can be measured. However, obtaining a density model above an active region is a non-trivial problem to solve; thus a quiet sun density model is often used frequently with double or even triple density values. Démoulin & Klein (2000) show density models for many different regions using solar eclipse observations by Koutchmy (1994) and they can be seen in Figure 5.11. From this plot, assuming a single model, and knowing the relationship between frequency and density, the altitude of the burst can be determined if you assume a density regime, viz:

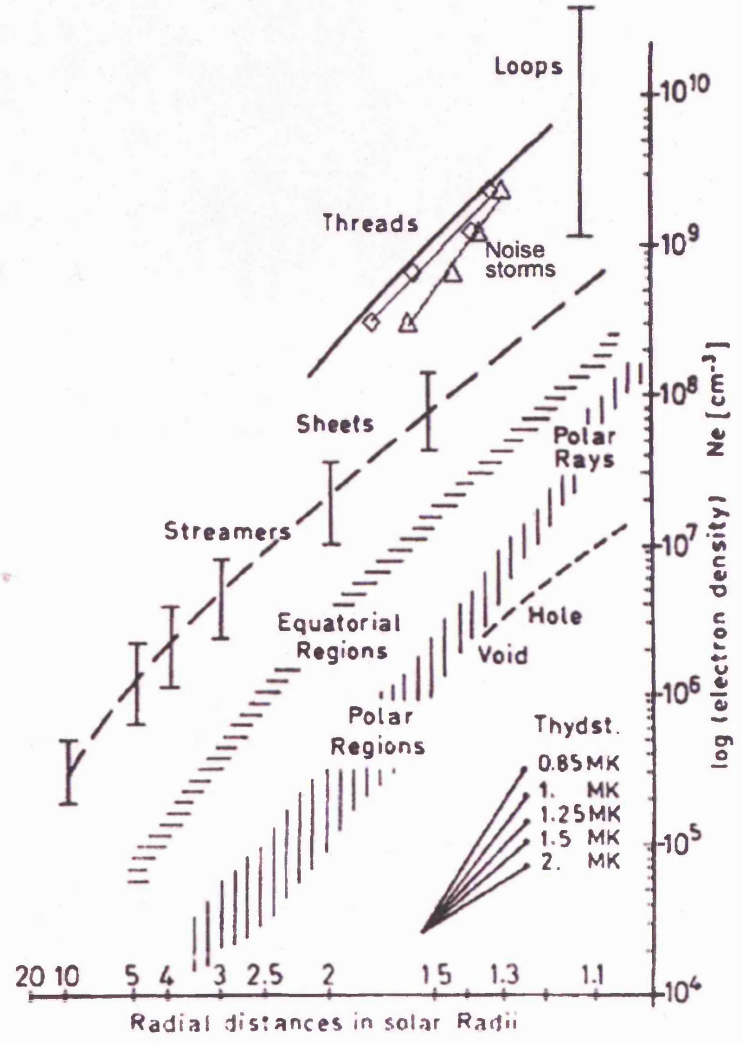

Figure 5.11: Density models from Démoulin & Klein (2000) where Thydst is the temperature of the hydrostatic model.

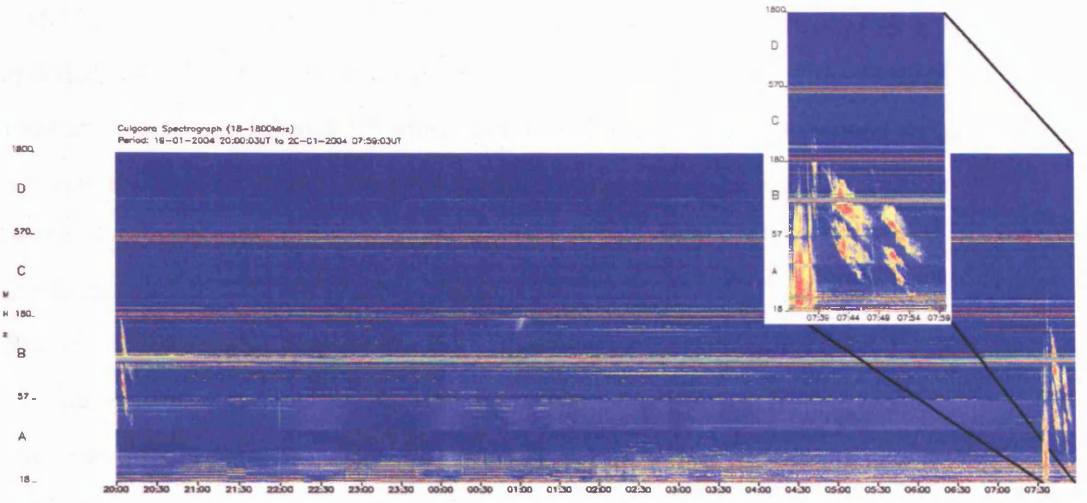

Figure 5.12: Culgoora dynamic radio spectrum. The blown up region shows the flare time. Over this period a type-III and two type-II bursts are observed. Note that both type–II emissions appear at both fundamental and the 1st harmonic frequencies.

$$f_p^2 = \frac{e^2 n_e}{4\pi^2 \epsilon_0 m_e} = 81 n_e Hz^2 \tag{5.1}$$

In this equation f_p represents the plasma frequency in Hz, e is the electron charge (1.69×10^{-19} Coulomb), m_e is the electron mass ($9.11 \times 10^{-31} kg$), n_e is the electron density (m^{-3}) and ϵ_0 is the permittivity of free space ($10^{-9}/(36\pi$)farad m^{-1}).

By determining the altitude at the beginning and the end of the type-II burst an average velocity can be determined. In this series of flares there were two metric type-II bursts that closely followed each other starting at 07:39 UT and 07:48 UT. They were observed by the Culgoora radio heliograph in Australia and can be seen in Figure 5.12. The time difference between these two bursts was 9 minutes which was similar to the time difference between the first two flare phases of the event. This suggests they are related to these respective flare phases. The shocks started after the beginning of the flares by 7 and 8 minutes respectively and after their maxima by about 2 and 5 minutes respectively. This is no surprise, since metric shocks start high in the corona, at 0.2–0.5 solar radii.

Culgoora gave a velocity for these type-II bursts as ~550 km s^{-1} for the first and

~850 km s^{-1} for the second. Therefore, by assuming that these speeds remained constant and that both bursts emanated from the same region, it was determined that they would interact at between 1.2 and 1.5 solar radii at 08:04 UT, where they could merge to create a single shock front with some average speed. These are true speeds, and thus the plane of the sky component must be determined for comparison with LASCO data. The flares are located at S14 W36 which means that the component of the 850 km s^{-1} shock is 550 km s^{-1} in the plane of the sky if it propagates radially outward.

Culgoora uses a quiet coronal density model by Newkirk (1967), largely for historical and consistency reasons, which may not be completely representative of the solar atmosphere at this time and place as densities vary depending on structure (Démoulin & Klein 2000). As seen in the LASCO data there were streamers over both the flaring region and the older dispersed region to the east. These small regions may better be described by the streamer density model in Figure 5.11. By using equation 5.1 and the frequency drifts supplied by Culgoora, new velocities can be determined. They are much higher. The first burst had a velocity of 1315 km s^{-1} and the second burst had a velocity of 2120 km s^{-1}. However, the blast waves will affect large regions and they will only pass through these streamer regions for short periods of time in the plane of the sky. Therefore the model most applicable would be some weighted combination of the two extremes, which would likely be closer to the Newkirk model.

Are these type–II bursts related to the CME? These two flares were quadrupolar flares which are usually thought to be confined. However, Type–II bursts can be caused by flare blast waves, which may be the case here. In this case, when two field lines in a sheared field configuration reconnect, a small and a longer loop form. The longer reconnected loop is 'dipped'. Magnetic tension will then make this dipped portion spring out to reach a semi-circular shape, which may then initiate a blast wave (Figure 5.13). This configuration is representative of the quadrupolar flares here. It was seen that the CME shock front first appeared in C2 at 08:06 UT. The two type–II shocks met at 08:04 UT at between 2.2 and 2.5 solar radii from Sun centre. It is thus possible that the shock front observed in C2

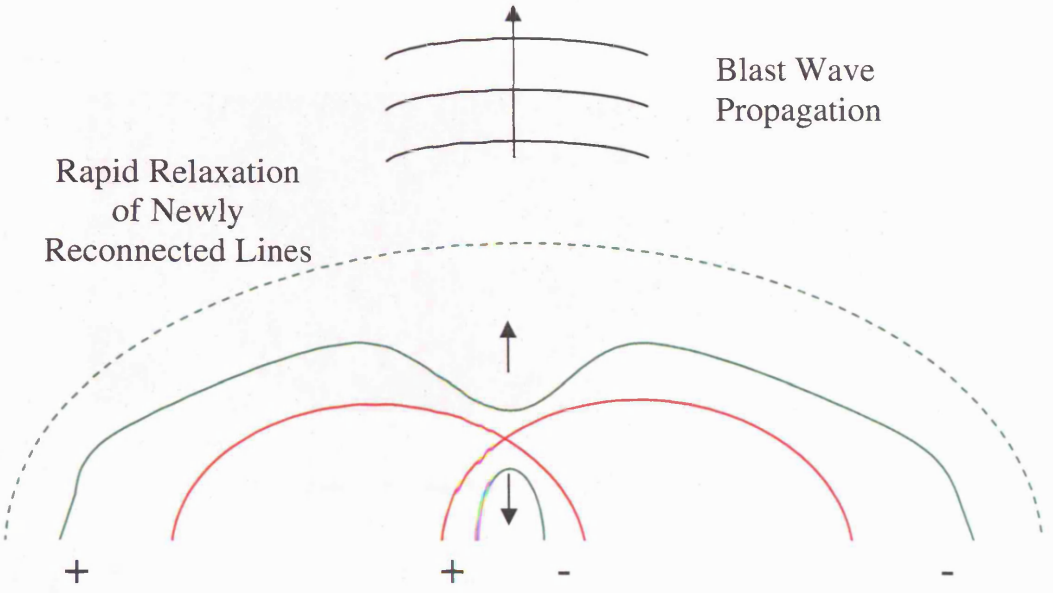

Figure 5.13: When the two red field lines reconnect they form the two green field lines. As the large green line springs to become the dashed curve, the point of minimum tension, a blast wave is generated, which later forms a shock.

is the result of the combined flare blast waves, when we account for the slight misalignment between centre of the Sun and the C2 field of view at this time which can be seen in the top images of Figure 5.8. It is unusual, however, that the shock/blast waves continue to be observed as high as LASCO C3.

5.2.2.4 Type-III Radio Busts

Type-III bursts are observed as fast drifts from high frequency to low frequency. They are representative of fast streams of electrons spiralling along open magnetic field lines. Type-III bursts are seen clearly in data from the *Wind* Waves (Bougeret et al. (1995)) instrument, which observes in the decametric-hectometric (DH) wavelength domains (Figure 5.14) as well as the Culgoora data. In the DH domain the burst begins at 07:36 UT drifting rapidly across the entire frequency range between 20 and 1 MHz in just a few seconds, although it is also seen at higher frequencies in the Culgoora data (Figure 5.12). This was

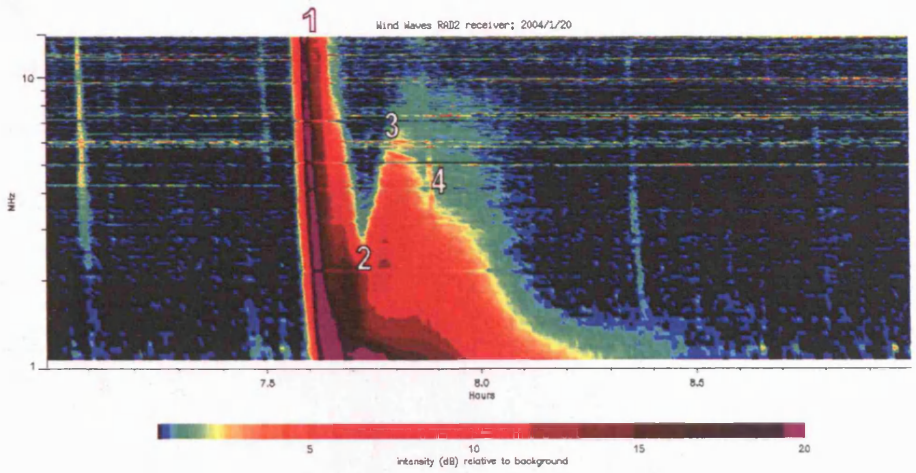

Figure 5.14: N–Burst with associated type-III observed by *Wind* Waves. (1) is a type–III burst, (2) indicates the turn–around point of the U–burst, (3) the first turn–around point which makes the burst an N–burst, and (4) the second turn–around point.

another piece of evidence that the open field was present over the flaring region, allowing streaming electrons to leave the Sun. However, at 07:42 UT there is a turn around at ~ 3 MHz (position 2 on the figure). This is followed by a further reversal at around 07:50 UT at 7 MHz (position 3). The frequency then drifts back to 1 MHz by 08:30 UT (position 4).

This was unusual. Instead of being a simple type-III burst, part of the burst was thought to be an N-burst (private communication Kaiser 2005). An N-burst starts like a simple type-III burst but the field lines along which the electrons are streaming are not fully open towards interplanetary space. In essence there is a large loop which may be expanding away from the Sun. The electrons spiral along the field lines and follow this large loop. Thus they stream from high to low density before turning back and returning towards higher density domains following the magnetic field. If this is where the burst ended it would be referred to as a U-burst. However, at some point there was an interaction within this large loop, again reversing the stream of electrons out towards interplanetary

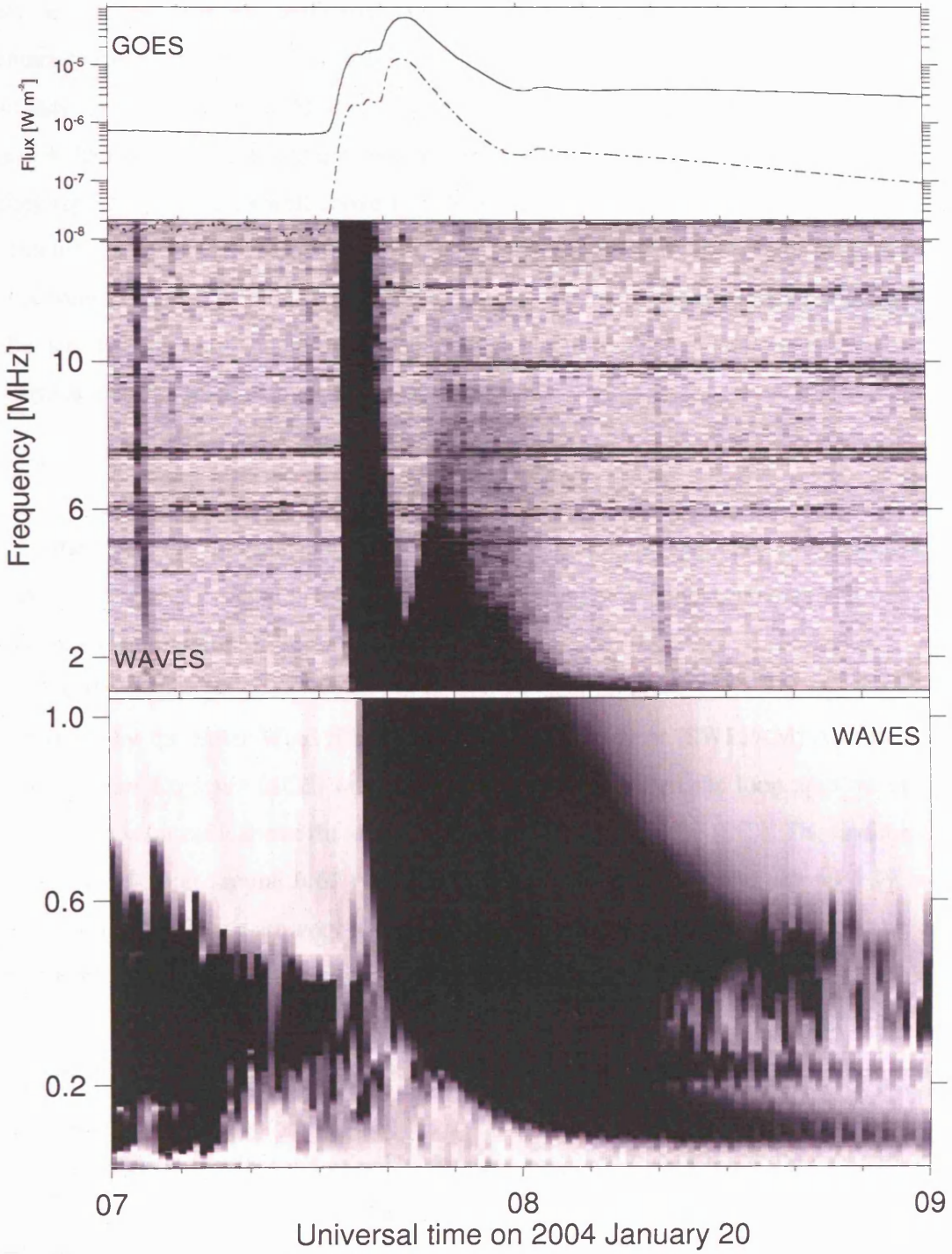

Figure 5.15: The type–III burst continues to Earth seen in the lower portion at very low frequency. However, the part of the electron beam that was reflected around the large expanding structure, left the Sun along a different path in the end. As they approach the Earth the radio observations break up, unlike the original burst and thus occupy a different point in space.

space. 5.14 was studied closely and it was possible to identify two points where there were interactions. These are at 07:48 UT and 07:55 UT, points 3 and 4 respectively. The height of these points could be calculated from the data by using the frequencies at positions 2, 3 and 4. If one uses the streamer density model of Figure 5.11 (Démoulin & Klein (2000)) they represent positions well above 10 solar radii. This would suggest large pre-existing structures were present. However, with long wavelength radio emission of observations it is commonly assumed that these regions fall into the interplanetary space regime where the density falls with square of the radius. The electron density can be measured at the Earth and scaled back using equation 5.2:

$$f_i = \frac{9\sqrt{n_{e(1AU)}} \cdot r_{(1AU)}}{r_i} \tag{5.2}$$

where f_i is the interplanetary frequency (kHz), $n_{e(1AU)}$ and $r_{(1AU)}$ are the electron density (cm^{-3}) and the radial distance (km) from the Sun at 1AU respectively, and r_i is the distance from the Sun of the emitted source (km).

Using this simple interplanetary case, and an electron density at 1 AU of ~6 m^{-3}, as measured by the Solar Wind Electron Proton Alpha Monitor (SWEPAM) on *Advanced Composition Explorer* (*ACE*) on the 20th January 2004, then the loop apex would be around 1.4 solar radii above the surface (2.4 radii from Sun centre (SC)). The first turning point would be at around 0.67 radii (1.67 Radii SC) and the second around 1.19 radii (2.19 radii SC). These are very low altitudes and the interplanetary assumption may not be completely appropriate this close to the Sun. Thus it may be that the density regime at the time of this event is somewhere between the two extremes of the Newkirk model and the streamer model. However, with no additional information it is impossible to refine these results further.

Why did the turn around at points 3 and 4 happen? Recall there were two type–II bursts and it may be that the turns are due to the interaction with these shocks. Assuming that the speeds determined by Culgoora are applicable the heights can also be determined knowing the time of flight. The first shock was initiated at 07:39 UT and the first turn around was at 07:48 UT. Thus the time of flight was 9 minutes travelling at 550 km s^{-1}.

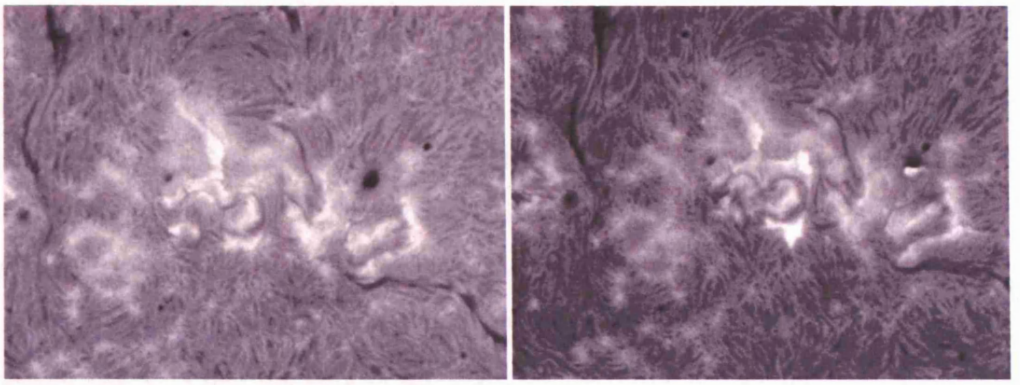

Figure 5.16: H-Alpha images showing the flaring region before and after the event. They show filaments which are present before and after the event. Left:07:20 UT Right:08:30

This shock can reach 0.62 radii (1.62 radii SC) in this time assuming that the shock is initiated at 0.2 radii (1.2 radii SC). This is remarkably similar to the first turn around point. The second burst was initiated at 07:48 UT and the second turn around was at 07:55 UT. The flight time was 7 minutes travelling at 850 km s^{-1}. Thus this shock can reach an altitude of 0.71 radii (1.71 radii SC) again assuming the shock was generated at 0.2 radii (1.2 radii SC). This is a bit lower than the 1.19 radii (2.19 radii sc) suggested from the turn around frequency, but this is not a very precise estimate as there are large errors in the density models. Also, the second shock has clearly started at greater height than the first as it had a different starting frequency.

The first type–III burst continues to Earth, seen in the lower portion of Figure5.15, at very low frequency. However, the N–burst tail does not drift as low in frequency as the first type–III burst. This suggests that the electrons which are moving along the large structure are guided to a direction different than that of the Earth. Therefore these electrons must be travelling outwards along a different magnetic structure than the electron beam of the main type-III burst.

5.2.2.5 H-Alpha Filaments

Another unusual aspect of this event is that the filaments surrounding the active region appeared to play no part in the mass ejection. We have H-alpha images from before and after the flare events and we saw that the filaments are still fully formed and have not changed significantly. These filaments can be seen in Figure 5.16.

Looking at the CME observations we observe a three part structure. This type of structure suggests that the core of the CME contains filamentary material, but it would appear from these images that the filaments remain intact. However, it is very difficult to determine if part of a filament has been released. In addition it is difficult to determine with the H-alpha coverage available whether part of the filament has been released and reformed in the time between images.

5.3 Discussion

On 20th January 2004 a flare series was observed of which the first two appeared to have a confined quadrupolar nature while the third was an LDE. This series of flares had an associated CME, which could have simply been related to the LDE. However, an investigation of the available data suggests a much more complex scenario that at first glance appeared contradictory. The series of flares showed signs of confined flaring but also clearly showed an eruptive tendency.

The *TRACE* images and magnetograms pointed to successive quadrupolar flare events in the first two phases. If this were a traditional set of flares following the models proposed by Melrose (1997), there would be no coronal mass ejections related to the first two flare phases. However, there was direct evidence of a CME from LASCO. The CME may not, however, have the traditional three part structure. It appears that the leading edge of the CME could be the combination of the two type–II bursts (i.e. shock fronts), as it was determined that they would have combined just prior to the observations in LASCO. Work on modelling a one–dimensional combination of pressure shocks (Poedts et al. 2002)

found that two shocks travelling in the same direction can combine and continue onward as one, with the introduction of a small backward component. In the example of the two type–II shocks in this chapter any backward component would be too faint to see.

Additionally the CME/shock front showed interaction with the large-scale streamer to the east, indicated by a wobbling motion and brightness increase. This streamer was likely to be rooted in the dispersed active region to the east of the flaring region. The first evidence for this streamer wobble was at 08:08 UT. The streamer base was estimated to be 200,000 km from the flare locations. This would mean that there was approximately a six minute travel time for shock one to reach the streamer base. If the shock hits the streamer it would be reasonable to assume that the disturbance would propagate up the streamer at the Alfven speed, which is approximately 1000 km s^{-1} in the corona at 100G. We estimate the streamer length to be 2 solar radii from the base to the edge of the occulting disc in LASCO C2. Travelling this distance at 1000 km s^{-1} would require a propagation time of approximately 23 minutes, which is the time between the shock hitting the streamer base and the first observation in C2.

At 07:47 UT connectivity is observed in the EIT difference images (Figure 5.10) between the flare region and the streamer region. This is two minutes after the first type–II shock hits the streamer base. Also the EIT base difference images show large scale dimming originating from the flare region, it can be deduced that the CME was likely to be from a region above the flaring active region. In addition, there was a CME from the same region some seven hours prior to this event. It was observed by Fazakerley et al. (2005) to have an interaction with this same streamer. It is thought that rapid expansion of loops over the active region, discussed above, were able to reconnect with the streamer described above.

The combination of observations allowed a possible scenario (Figure 5.17) describing the whole process to be drawn. To the top right of the cartoon the flare site is situated across a neutral line. Clearly the actual site is far more complicated than depicted but it does illustrate the general principle. As the flares occur they produce east-west loops of increasing length that act to make the loops above expand. There is also a type–II

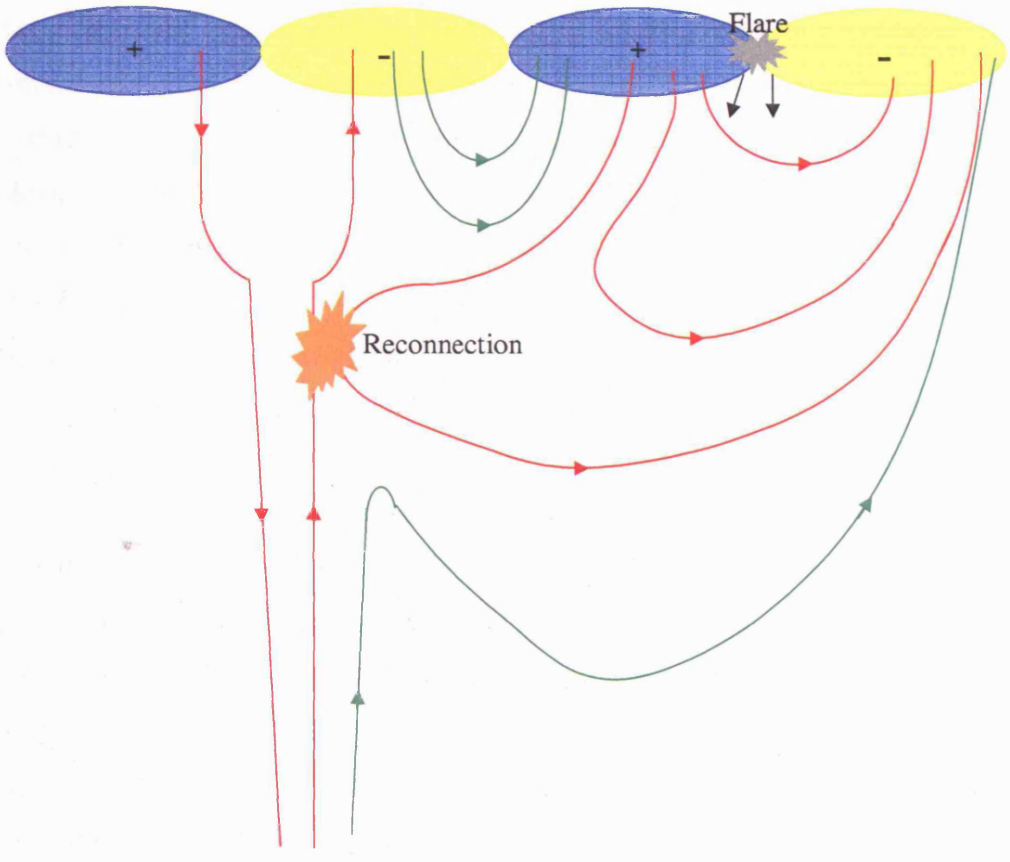

Figure 5.17: Cartoon illustrating a possible scenario for this event. It shows that as the flare progresses the large red loops rise. At some point they reconnect with the streamer causing new magnetic connectivities, shown in green.

shock blast wave which emanates from the flare site which may cause the large loops to interact with the streamer to the left of the cartoon. At this meeting point the fields are anti-parallel, therefore reconnection can occur. We do not expect to see direct evidence for this reconnection, as it is likely to be occurring below the occulting disk, but swaying in the streamer is observed which is suggestive of interaction. This could result in new connections being created as shown in green. This would give rise to a contracting series of small loops crossing the neutral line between the two large active regions for which we saw evidence in the EIT difference images. Additionally as a result of this reconnection, large open field lines are created across the original flaring AR. These will rise and move to the west allowing plasma to be released from the atmosphere, constituting the CME. This moving field line could also represent the frontal part of the CME, as it would try to straighten out, bringing plasma with it.

Additionally there was a type–III burst with an N–burst. This is also consistent with the cartoon shown in Figure 5.17. If electrons are spiralling along these large field lines one would expect to see the U-burst as described earlier. However, it is possible that the electrons had their journey impeded by the two type–II bursts. There are two points in the N–burst data where the electrons are seen to turn back towards interplanetary space, probably due to interactions with the type-II blast waves or the reconnection with the open streamer field lines: the beam is travelling along a curved path. Also the electrons accelerated from the reconnection with the streamer would move along a different structure, i.e. the streamer, which can explain the apparent frequency split in Figure.5.15.

The CME core observed by LASCO is likely to be as a result of a partial filament eruption. We say that the phase–III event was an LDE, which are most commonly associated with CMEs. It is plausible that as a result of successive flare events, the overlying field has lower tension as loop length increased. Therefore, the retaining force exerted on the filaments in the region was reduced. This would allow a partial filament eruption. This scenario has parallels with the breakout model, where the overlying field is gradually reduced until there comes a point where the filament can push through.

The above described process would allow the confined flares to remain confined and

the large-scale field would give rise to a CME. This can also explain why the filaments remain unchanged from before the flaring activity.

5.4 Conclusions

We found that this series of events is extremely complicated. We have seen that the confined flares in phase–I and II cause the rapid expansion of loops and two blast waves. These blast waves may push these expanding magnetic loops into a streamer field line which was anti-parallel allowing reconnection. This creates a large expanding opening structure. The CME appeared at first to have a traditional three part structure; however, the frontal part is likely to be the combination of the two shock fronts caused by blast waves initiated by the flares or the sweeping of the large newly reconnected structure. The gradually lengthening magnetic connectivities due to the reconnections of phase I and II flares created expanding loops which have a lower tension force and thus make it easier for a filament from beneath the loops to erupt. This is likely to have happened causing the CME core seen in LASCO, and the LDE. It is seen in this study that the fortuitous rearrangement of magnetic field allowed the CME release. This event has demonstrated, however, that not all events can be described by a single model. These events have required numerous flare and CME models to interact to give rise to these observations.

Chapter 6

Conclusions and Future Work

This thesis has shown that solar events are by nature very complex and to understand them fully multi–wavelength observations are essential. The solar community has been fortunate that there are often observations from numerous ground–based and space–based instruments and I hope that this will continue to be the case.

Very valuable analysis can be performed in a single waveband for specific purposes, but it is most important that this information is then cross–referenced with studies in other wavelengths to correctly interpret the observations in context. This thesis presented several multi–wavelength studies which probed individual characteristics of flares and CMEs. It showed that they are often intimately linked and it was therefore appropriate that they should be studied as a complete phenomenon.

The thesis consists of three original science chapters that each present a separate research product with the core science falling under the umbrella of non-thermal emission. To begin with a study of hard X–ray emission from a group of small confined HXR flares was presented followed by a larger explosive event in the next chapter; and then finally a much more complex explosive event was considered in many wavebands.

6.1 Relating Magnetic Field Strength to Hard X–Ray footpoints

Chapter 3 presented a statistical study of flare hard X–ray footpoint emissions and its relationship to magnetic field strength using data from *Yohkoh*'s HXT and *SoHO*'s MDI. It has been previously reported by Sakao (1994) that the location of the stronger magnetic footpoint has weaker HXR emission. However I have shown that the relation between the magnetic flux density at the footpoints of a flaring loop and HXR emission is much more complicated than previously thought.

Sakao studied a small sample of just 5 flares, and is often referenced in the literature. However, although the study was competently performed it was limited by the number of events available and by the quality and quantity of magnetogram data which could be used. I have shown in this thesis that a significant number of events contradict these findings, having the stronger magnetic footpoint coincident to the stronger HXR emission.

To perform this study it was required that a fair method of measuring the magnetic flux density beneath any given HXR footpoint was developed. Also a much larger sample, than considered by Sakao, was used for events where magnetogram data was taken not more than 45 minutes from the event time.

From my sample of 32 events, 40% were the traditional Sakao type (S–type), 25% were approximately symmetrical in mean magnetic field strength (B–Type) and 30% were the non-Sakao type (N–type). There was, however, little difference between the physical properties of each of these flares. The mean spectral index at the peak was almost the same in each of the three classes with a value of 3.4 in the S-type, and 3.5 in the N-type; with soft-hard-soft evolution across the board.

It was unfortunate that individual HXR light curves could not be compiled for each footpoint. This information would have allowed any time lags between emissions to be observed which would give weight to an asymmetry in the location of the acceleration site and thus the resulting precipitation of electrons and HXR emission at the footpoints. An asymmetry in the location of the acceleration site might explain the occurrence of N-type

events. If the acceleration site was located closer to the brighter footpoint it might reduce the effects of convergence over the shorter distance, allowing more precipitation in this region than if the acceleration site was located at the loop apex. Future observations may be possible to confirm this, although we are unable to rule out some other process that impedes the electron precipitation at the weaker footpoint.

There were only two events, in the N-type cases, that had timing information and both had simultaneous light curves for both footpoints. However, there were very few HXR images that were integrated over a relatively long period of time that gave rise to a poor cadence.

The work of Aschwanden et al. (1999a) described an asymmetric trap model. They assumed that the acceleration site for the electrons was equidistant from each of the flare footpoints and predicted that the median value for the ratio of the magnetic fields at the footpoints would be 1.2. We found this to be the case in the B-type events, although the S-type have a median value of 0.4 and the N-type a value of 3.4. Therefore, using the method of observation presented here, it was not possible to confirm their predictions, although it is unknown how moving the acceleration site would affect them.

In conclusion I have determined that the N–type events are more common than previously thought. Until now these events have been considered as the curious anomaly, such as that illustrated in the work of Asai et al. (2002) and Aschwanden et al. (1999a).

6.1.1 Future Work

Further work by Alexander & Metcalf (2002) showed some of the limitations to this work. By utilising *RHESSI* 's higher spatial and energy resolution and also utilising the process of magnetic field extrapolation, they were able to look in detail at electron trapping in a single flare. The *RHESSI* images showed clearly the loop top source and the use of magnetic extrapolations enabled them to determine a possible value for the magnetic field at the loop apex along with the full magnetic field at the loop footpoints. As the convergence in magnetic field can only truly be determined by comparing the loop top field with the

footpoint, they had a much better understanding of the setup in this case. In addition the asymmetry could be measured on numerous occasions as the flares progress allowing you to see how this changes as well as how it changes with energy.

Many processes affect the distribution of particles in space (e.g pitch angle scattering) and in energy (e.g. Coulomb collisions), and these have an effect on the production of photons, affecting total flux, spectral shape, and spatial location of emission. However, for coronal densities and HXR–producing electron energies, the coronal transit time is very much shorter than the collisional/scattering times and so the corona only has an major effect on the particle distribution if the particles remain in the corona for longer, i.e., via coronal trapping.

By using spatially resolved HXR observations it should be possible to see how particles on each side of the flaring loop have been affected and thus give some clue as to the nature of the trapping. It may then be possible to compare the trapping rate to the magnetic field strengths beneath the flare footpoints. It is widely believed that S-type events are the result of converging magnetic field lines in strong regions, which act to mirror precipitating electrons and thus reduce those available to create HXR through thick-target bremsstrahlung. Conversely with less convergence in weaker field regions, more electrons can precipitate to the chromosphere and give rise to a stronger HXR footpoint. So why should we observe N-type events? Unfortunately in the examples of chapter 3 there was insufficient data in most cases and in the others the spectral resolution was too poor to distinguish between the footpoints. With *RHESSI* however, the spectral resolution is much better and it may therefore be possible to perform a similar study but look at the spectral effects in much more detail.

As mentioned above spatially resolved spectral information would greatly improve this work. *RHESSI* has made this possible now with its greater spectral resolution. This will allow us to develop an understanding of the relative trapping nature on each footpoint leg and thus give us the ability to assess how this relates to the magnetic field under each flare footpoint.

Also magnetic connectivity can be very complex and some clues can be gained by

studying SXR images. However, while these images can show what appears to be a single loop, they only show structures containing hot plasma and give little information about any fine structure or the environment in which the flare occurs. The latter is especially important, as it is the magnetic field convergence which is responsible for the mirroring of electrons and not the strength of the field alone. A detailed study of the magnetic field surrounding the footpoints may give rise to a clearer understanding of these mirror points. If one studies the field around the footpoint, it may be possible to determine how much the field can expand giving a better understanding of the level of convergence. A study such as this would provide an interesting continuation of this project.

6.2 A Slow CME with Rising X–Ray Source

Chapter 4 described a single explosive flare event that occurred on the west limb following a series of homologous events. The mechanisms for filament eruptions are not well understood and many models have been proposed (e.g. Forbes 2000; Török et al. 2004). There are a very limited number of observations (e.g.Gallagher et al. (2002); Foley et al. (2001); Pike & Mason (2002); Williams et al. (2005)) from the low corona making it very difficult to constrain the models. The eruptive event on 16th April 2002 had high quality observations available in numerous energy enabling the filament to be tracked from the low corona in *TRACE* 195 Å. The same filament was later seen in CDS Fe XIX and was followed by the observation in LASCO C2/C3 as a CME.

By careful study of the *TRACE* 195 Å movie it was apparent that there was some global deformation of the filament, which might suggest kinking, although quantitative measurement of this is difficult. As the filament lifted it crossed the CDS slit field of view. The measured Doppler velocities indicated that there was an inherent helical structure to this loop, highlighted by helical flows. A similar observation was made for an on-disc filament by Foley et al. (2001) and Pike & Mason (2002). In my case red and blue shifted emissions were found on opposing sides suggestive of helical flows, allowing the inference that this filament was contained within a magnetic flux rope.

As the flux rope lifted, it dragged overlying arcade magnetic field lines with it. These stretch the field beneath forming a current sheet. At this point magnetic reconnection can begin producing strong outflows (jets) from the reconnection region as well as flare loops.

The *RHESSI* observations of this event showed that the flare loop top source was unusually bright relative to the footpoints. Assuming that this event was homologous with those of the previous two days, then it could be described as a loop which is collisionally thick at electron energies up to 50 keV (Veronig & Brown 2004). There was also a coronal source observed up to 25 keV as shown in Figure 4.6. This source moved upward and followed the rising flux rope with a comparable velocity at a constant distance of roughly 20,000 km, implying an intimate link. I suggest that this indicates the formation of a plasmoid and is indicative of a shock front from the reconnection jets like the scenario detailed by Tsuneta (1997). There have been few observations of plasmoids and in the model proposed by Shibata et al. (1995) it is suggested that the plasmoid is actually the filament/flux rope. However, this is clearly not the case here.

Following the passage through the CDS slit field of view of the flux rope, there was a period of weak emission. This corresponds with the passage of the coronal X-ray source and may also include to the magnetic X–point or current sheet. When one studies the *TRACE* 195 Å movie closely, the brightening of loops and the formation of a cusp can be seen, the peak of which is deduced to be located around the position of the CDS slit at the time of the gap. At this point the emission measure would be low and little emission would be expected.

Following this time there was an extended period of about 90 minutes when the velocity pattern was suggestive of down–flows along the hot, newly reconnected loops. Doppler velocities seen by CDS combined with 3-D magnetic modelling of these loops suggested that we were seeing the falling material either coming towards or moving away from us. We believe that observations represent this rather than general loop shrinkage as the largest Doppler shifts are seen to be at the edges of this expanded region with much lower velocities in between.

The flux rope continued to rise and was observed as a CME in LASCO C2/C3. The

leading edge was measured along with the rear of the CME and the two lines were plotted on the height-time plot. It was clear that a massive velocity change would be required in order to reach the C2 heights in the available time which could be provided by the exponential function. This growth is present in ideal instabilities such as the kink instability simulations by Török et al. (2004) and Kliem et al. (2004). These authors suggest the kink instability of a coronal flux rope as a possible initiation mechanism of solar eruptions. These data suggest that the CME has slowed and reached a steady state by the time it is observed by LASCO, possibly due to the relatively slow nature of the CME. Gallagher et al. (2003) presented an event with a very similar profile with additional data from UVCS which provided a valuable point between *TRACE* and LASCO. Even without this UVCS point it was possible to show that an exponential function was required to produce the altitudes required in the allotted time frame.

6.2.1 Future Work

There are very few examples of such events available to the community but their importance has been shown throughout this work. The examples that have been previously published and examples found in the future need to be brought together for direct comparison. By a rigorous analysis of the height time profiles it may be possible to make better correlations with the initiation models which currently exist or may even help to develop further models. It may be possible to utilise the current high cadence operations of *TRACE* to observe more of these events allowing for further comprehensive studies such as this.

More observations in the region between the *TRACE* field of view and that of LASCO C2 are needed. With the ability to track these moving features as they leave the Sun and propagate into space, a more accurate height time plots can be made of the acceleration profile. This information is vital for modellers as they can then start to refine their existing models using realistic data from many events rather than just boundary condition data from a few 'special' events such as the one shown here.

The picture of filament eruptions would be still further improved if there were some kind of 3–D perspective available, such as that which may be provided by *STEREO*. With coronagraph and EUV imager data from more than one perspective it should be possible to determine the actual velocity, and thus acceleration, profile of such events which would remove a further uncertainty in the observational data.

Additionally if *Solar Orbiter* were to produce magnetograms from directly above a region where an erupting filament were to occur and this information could be combined with the data from *STEREO* further constraint can be placed on the figures required to produce verification for the models of erupting filaments.

6.3 A Series of Confined Flares With Associated CME

Chapter 5 presented the results of a study into a flare series which constituted of quadrupolar 'confined' flares and an LDE on the 20th January 2004. The classical picture depicted by the quadrupolar flare models of e.g. Sweet (1958) and Melrose (1997) suggest that they remain confined due to the topology of the reconnection.

We determined that the flares were quadrupolar in nature by comparing the *TRACE* 1600 Å images to the magnetogram evolution. However, we also noted numerous indications of the explosive nature of these events ranging from weak evidence such as metric type–II and type–III radio signatures, to the direct observation of a CME in LASCO C2 and C3. It was thus important to determine how this situation could occur if the Melrose model holds.

The range of observations we gathered allowed us to illustrate a possible scenario (Figure 5.17) which described a process by which a series of 'confined' flares and a small LDE can lead to a fast CME. We find that the initial quadrupolar flares led to the creation of a series of long east–west magnetic loops. These loops pushed the pre–existing loops above causing them to expand. These same flares also generate type–II blast waves like those described by Gopalswamy et al. (1998). They propagate radially and push the large

overlying loops into an existing streamer in the east. At this point the fields are anti-parallel, and reconnection can occur. It was not unexpected that direct evidence for this reconnection was not observed, as it is likely to be occurring below the occulting disc, but swaying and brightening in the streamer was observed suggesting an interaction.

Additionally, assuming the blast waves travel at the speeds determined by Culgoora, they would meet just below the occulting disc and would continue as a single wave front, which might be observed as a density enhancement in LASCO C2. The timings are such that the CME front appears at about the same time as combined shock would appear. However, this is not the only explanation; it could also have been produced by the large field lines above the active region formed by the reconnection which sweeps out as they try to straighten to a point of minimum tension. Additionally there was a type-III burst with an N–burst related to this series of event. This is also consistent with the cartoon. Electrons spiralling along an opening structure giving rise to such emission due to their flight paths.

This reconnection with the streamer would also result in new connections being created between the active regions, taking the form of a contracting series of small loops crossing the neutral line between the two large active regions. Evidence was seen in the EIT difference images. The large open structures formed rise and move to the west allow plasma to be released from the atmosphere giving rise to coronal dimmings observed with EIT (Figure 5.10).

It was not possible for the LDE, thought to form as a result of a filament eruption, to be responsible for the CME front observed in C2 as there was insufficient time. However, the core of the CME was significantly slower and there was likely sufficient time for an erupting filament to reach the required altitudes.

By assuming the process that I have suggested the quadrupolar flares can remain confined while the large-scale field gives rise to a CME front followed by a more traditional filament eruption as the large restraining and overlying field was weakened or even removed.

In conclusion I have shown that under the right magnetic conditions it is possible for

flares to cascade along a magnetic inversion line. As each flare progresses the rearrangement of magnetic field makes the conditions for further flaring favourable. In addition these 'small–scale' events can rearrange magnetic field in such a way as to give rise to large–scale phenomena.

6.3.1 Future Work

This work has made a significant contribution to the discussion of nature of 'confined' flaring. Although the flares portrayed traditionally confined behaviour their effect on the large scale was fundamental on large–scale processes. One of the most significant problems we encountered while studying this event was the lack of coverage in the Corona below C2 as before. While trying hard to assess the timings and relations between different aspects of these events it was difficult to make judgements when features are not observable. With the addition of data in this region, it should be much easier to link features.

6.4 Final Remarks

This thesis has looked in detail at the footpoints of flaring events and moved on to study specific examples of large explosive events, following their effects into the corona and beyond. The work has shown that as the availability of observations improves and their coverage increases the pictures we build continue to evolve. With the addition of space–based magnetograms, the work that was so reliant upon them could be performed with greater ease. Larger samples could be taken and the general picture of what was always assumed to be fact, changed. It was found that the 'odd case' was more common than previously thought. A significant number of events had their stronger HXR footpoint in the region of stronger magnetic field.

It is my hope, that as observations improve, a similar thing will happen with the study of CMEs and their origin. With 3–D observations it should be possible to track CMEs to

their source with much more reliability, as well as observe their initiation phase. It is only then that it becomes possible to see if the events observed here are unique or if they are much more common than previously thought.

Bibliography

Alexander D., Metcalf T.R., Nov. 2002, Sol. Phys., 210, 323

Alissandrakis C.E., Jul. 1981, A&A, 100, 197

Antiochos S.K., Devore C.R., Klimchuk J.A., Jan. 1999, ApJ, 510, 485

Asai A., Masuda S., Yokoyama T., et al., Oct. 2002, ApJ, 578, L91

Aschwanden M.J., Schwartz R.A., Alt D.M., Jul. 1995, ApJ, 447, 923

Aschwanden M.J., Fletcher L., Sakao T., Kosugi T., Hudson H., Jun. 1999a, ApJ, 517, 977

Aschwanden M.J., Kosugi T., Hanaoka Y., Nishio M., Melrose D.B., Dec. 1999b, ApJ, 526, 1026

Aulanier G., DeLuca E.E., Antiochos S.K., McMullen R.A., Golub L., Sep. 2000, ApJ, 540, 1126

Beckers J., 1972, Annual Review of Astronomy and Astrophysics, 10, 73

Berger T.E., Lites B.W., Apr. 2003, Sol. Phys., 213, 213

Bottema M., Woodruff R., 1971, Appl. Opt., 10, 300

Bougeret J.L., Kaiser M.L., Kellogg P.J., et al., Feb. 1995, Space Science Reviews, 71, 231

Brown J.C., 1971, Sol. Phys., 18, 489

Brown J.C., 1972, Sol. Phys., 26, 441

Brueckner G.E., Howard R.A., Koomen M.J., et al., 1995, Sol. Phys., 162, 357

Burkepile J.T., et al., Dec. 1994, In: ESA SP-373: Solar Dynamic Phenomena and Solar Wind Consequences, the Third SOHO Workshop, 57

Canfield R.C., Gunkler T.A., Ricchiazzi P.J., Jul. 1984, ApJ, 282, 296

Carmichael H., 1964, In: The Physics of Solar Flares, 451

Carrington R.C., Nov. 1859, MNRAS, 20, 13

Carrington R.C., Apr. 1863, MNRAS, 23, 203

Démoulin P., van Driel-Gesztelyi L., Mandrini C.H., Klimchuk J.A., Harra L., Mar. 2003, ApJ, 586, 592

Delaboudiniére J.P., Artzner G.E., Brunaud J., et al., 1995, Sol. Phys., 162, 291

Démoulin P., Klein K., 2000, Lecture Notes in Physics, Berlin Springer Verlag, 553, 99

Demoulin P., van Driel-Gesztelyi L., Schmieder B., et al., Apr. 1993, A& A, 271, 292

Dennis B.R., Hudson H.S., Krucker S., 2005, Proceedings of CESRA Workshop 2004 'The high energy solar corona: waves, eruptions, particles' on the Isle of Skye

Domingo V., Fleck B., Poland A.I., 1995, Sol. Phys., 162, 1

Dryer M., 1982, Space Science Reviews, 33, 233

Dungey J.W., 1953, MNRAS, 113, 679

Edlén B., 1942, Z. Astrophys., 22, 30

Fazakerley A.N., Harra L.K., Culhane J.L., et al., 2005, submitted

Foley C.R., Harra L.K., Culhane J.L., Mason K.O., Oct. 2001, ApJ, 560, L91

Forbes T.G., Oct. 2000, Journ. Geo. Rev., 14, 23153

Forbes T.G., Sep. 2003, Advances in Space Research, 32, 1043

Forbes T.G., Acton L.W., Mar. 1996, ApJ, 459, 330

Gallagher P.T., Dennis B.R., Krucker S., Schwartz R.A., Tolbert A.K., Nov. 2002, Sol. Phys., 210, 341

Gallagher P.T., Lawrence G.R., Dennis B.R., May 2003, ApJ, 588, L53

Goff C.P., Matthews S.A., van Driel-Gesztelyi L., Harra L.K., Aug. 2004, A& A, 423, 363

Goff C.P., van Driel-Gesztelyi L., Harra L.K., Matthews S.A., Mandrini C.H., May 2005, A& A, 434, 761

Gopalswamy N., Kaiser M.L., Lepping R.P., et al., Jan. 1998, Journ. Geo. Rev., 103, 307

Gorbachev V.S., Somov B.V., 1988, Sol. Phys., 117, 77

Gosling J.T., Hildner E., MacQueen R.M., et al., Nov. 1974, Journ. Geo. Rev., 79, 4581

Green L.M., Matthews S.A., van Driel-Gesztelyi L., Harra L.K., Culhane J.L., Feb. 2002, Sol. Phys., 205, 325

Gull S.F., Daniell G.J., Apr. 1978, Nature, 272, 686

Hagenaar H.J., Schrijver C.J., Title A.M., Feb. 2003, ApJ, 584, 1107

Hanaoka Y., May 1996, Sol. Phys., 165, 275

Handy B.N., Acton L.W., Kankelborg C.C., et al., Jul. 1999, Sol. Phys., 187, 229

Hara H., 1996, Structures and Heating Mechanisms of the Solar Corona, Ph.D. Thesis

Harra L.K., Mandrini C.H., Matthews S.A., Nov. 2004, Sol. Phys., 223, 57

Harrison R., 1995, A&A, 304, 585

Harrison R., 1996, Sol. Phys., 166, 441

Harrison R., 2002, In: COSPAR, Plenary Meeting

Harrison R.A., Sawyer E.C., Carter M.K., et al., 1995, Sol. Phys., 162, 233

Heyvaerts J., Priest E.R., Rust D.M., Aug. 1977, ApJ, 216, 123

Hirayama T., 1974, Sol. Phys., 34, 323

Hogbom J.A., Brouw W.N., Jul. 1974, A&A, 33, 289

Hoyng P., van Beek H.F., Brown J.C., Jun. 1976, Sol. Phys., 48, 197

Hurford G.J., Schmahl E.J., Schwartz R.A., et al., Nov. 2002, Sol. Phys., 210, 61

Hurford G.J., Schwartz R.A., Krucker S., et al., Oct. 2003, APJ, 595, L77

Illing R.M.E., Hundhausen A.J., Jan. 1985, Journ. Geo. Rev., 90, 275

Kaiser M., 2005, Private Communication

Kane S.R., 1974, In: IAU Symp. 57: Coronal Disturbances, 105–141

Kay H.R.M., Harra L.K., Matthews S.A., Culhane J.L., Green L.M., Mar. 2003, A&A, 400, 779

Kliem B., Titov V.S., Török T., Jan. 2004, A&A, 413, L23

Klimchuk J.A., Antiochos S.K., Norton D., Watko J.A., May 2000, AAS/Solar Physics Division Meeting, 31,

Kohl J.L., Esser R., Gardner L.D., et al., 1995, Sol. Phys., 162, 313

Kopp R.A., Pneuman G.W., Oct. 1976, Sol. Phys., 50, 85

Kosugi T., Masuda S., Makishima K., et al., Nov. 1991, Sol. Phys., 136, 17

Kosugi T., Sakao T., Masuda S., et al., Oct. 1992, PASJ, 44, L45

Koutchmy S., Apr. 1994, Advances in Space Research, 14, 29

Lin R.P., Dennis B.R., Hurford G.J., et al., Nov. 2002, Sol. Phys., 210, 3

Mandrini C., Démoulin P., Klimchuk J., 2000, ApJ, 530, 999

Mandrini C.H., Demoulin P., Henoux J.C., Machado M.E., Oct. 1991, A& A, 250, 541

Masuda S., Kosugi T., Hara H., Tsuneta S., Ogawara Y., Oct. 1994, Nature, 371, 495

Melrose D.B., Sep. 1997, ApJ, 486, 521

Metcalf T.R., Hudson H.S., Kosugi T., Puetter R.C., Pina R.K., Jul. 1996, ApJ, 466, 585

Munro R.H., Gosling J.T., Hildner E., et al., Feb. 1979, Sol. Phys., 61, 201

Neupert W.M., Jul. 1968, APJ, 153, L59

Newkirk G.J., 1967, araa, 5, 213

Ogawara Y., Takano T., Kato T., et al., Nov. 1991, Sol. Phys., 136, 1

Ohyama M., Shibata K., May 1998, ApJ, 499, 934

Parker E.N., Dec. 1957, JGR, 62, 509

Parker E.N., Jul. 1963, APJS, 8, 177

Parks G.K., Winckler J.R., Feb. 1969,
apj, 155, L117+

Petschek H.E., 1964, In: The Physics of Solar Flares, 425

Pike C.D., Mason H.E., Apr. 2002, Sol. Phys., 206, 359

Pina R.K., Puetter R.C., Jun. 1993, PASP, 105, 630

Poedts S., van der Holst B., de Sterck H., et al., Mar. 2002, In: ESA SP-477: Solspa 2001, Proceedings of the Second Solar Cycle and Space Weather Euroconference, 263–270

Ricchiazzi P.J., Canfield R.C., Sep. 1983, ApJ, 272, 739

Sakao T., 1994, Ph.D. Thesis

Sato J., Kosugi T., Makishima K., Feb. 1999, PASJ, 51, 127

Scherrer P.H., Bogart R.S., Bush R.I., et al., 1995, Sol. Phys., 162, 129

Schindler K., Hornig G., 2001, Magnetic reconnection In Murdin 2000

Sheeley N., Howard R., Koomen M., Michels D., 1983, Astrophys. J., 272, 349

Shibata K., Masuda S., Shimojo M., et al., Oct. 1995, ApJ, 451, L83

St. Cyr O.C., Dec. 1997, In: ESA SP-415: Correlated Phenomena at the Sun, in the Heliosphere and in Geospace, 103

Sturrock P.A., 1966, Nature, 211, 695

Sui L., Holman G.D., Dennis B.R., Sep. 2004, ApJ, 612, 546

Sweet P.A., 1958a, In: IAU Symp. 6: Electromagnetic Phenomena in Cosmical Physics, 123–+

Sweet P.A., Feb. 1958b, The Observatory, 78, 30

Török T., Kliem B., Titov V.S., Jan. 2004, A&A, 413, L27

Thompson B.J., Plunkett S.P., Gurman J.B., et al., Jul. 1998, GRL, 25, 2465

Tsuneta S., Jan. 1996, ApJ, 456, 840

Tsuneta S., Jul. 1997, ApJ, 483, 507

Tsuneta S., Acton L., Bruner M., et al., Nov. 1991, Sol. Phys., 136, 37

Tsuneta S., Hara H., Shimizu T., et al., Oct. 1992, PASJ, 44, L63

Vaiana G.S., van Speybroeck L., Zombeck M.V., et al., 1977, Space Science Instrumentation, 3, 19

van Driel-Gesztelyi L., Hofmann A., Demoulin P., Schmieder B., Csepura G., Feb. 1994, Sol. Phys., 149, 309

Veronig A.M., Brown J.C., Mar. 2004, ApJ, 603, L117

Williams D.R., Török T., Démoulin P., van Driel-Gesztelyi L., Kliem B., 2005, APJ, in press

Willingdale R., 1981, MNRAS, 194, 359

Yokoyama T., Akita K., Morimoto T., Inoue K., Newmark J., Jan. 2001, APJ, 546, L69

Zhang J., Dere K.P., Howard R.A., Vourlidas A., Mar. 2004, ApJ, 604, 420

Chapter 7

Acknowledgements

I would like to take this opportunity to thank a few people for making this thesis possible. First and foremost I would like to thank my wife Jane, who has had great patience with all my weekend work, especially in the last few months. She has been a pillar of strength and been able to listen when I thought it was all going to fall apart. I would also like to thank my parents who have had to listen to me moan about how long it takes to write one of these books.

I would like to thank Sarah Matthews and Louise Harra for their support as my supervisors. They have supported me every step of the way and even with the arrival of little Matthew, were always there to pass a critical eye over the projects.

Special thanks to Lidia 'The Oracle' van Driel–Gesztelyi, for never telling me my question was stupid, and for giving me so much of her time. Also special thanks to Len Culhane, who especially over the past few months has given so much time in the discussion of my final chapter (I hope Mary will forgive me for keeping you in the lab late on more than one occasion). And also thanks to Cristina Mandrini and Pascal Démoulin, whose ideas and skills have contributed so much to my understanding.

It is at times like the final months of thesis writing that you really appreciate your friends. Especially those who have had the misfortune to have actually written or be in the process of writing a thesis. Of special note are Dave Williams, Hilary Kay and Lucie Green who had to answer countless questions throughout my time at the lab. Also Tracey

Poole and Steve Fuerst who kept me sane during my time in the student office.

Thanks to PPARC for their funding of my research, long may others have the opportunity to suffer in the same way.

And last but not least thanks to Prof. Richard Harrison and Prof. John Brown for not being as scary as Sarah, Lidia and Len.